nature cell biology

Article

https://doi.org/10.1038/s41556-026-02030-7

Nuclear class 3 PI3K co-activates fasting-specific chromatin remodelling

Received: 7 February 2025

Accepted: 26 June 2026

Published online: 28 July 2026

Check for updates

Nathaniel F. Henneman[1,2], Genki Kawamura[3,11], Ying Luo[1,2,11], Catia Oliveira Dias[1,2], Jiaqi Su[1,2], Arianna Segaloni[1,2], Ivan Nemazanyy[4], Samuel le Cam[5], Calvin Rodrigues[5], Nicolas Kuperwasser[6], Nicolas Cagnard[7], Karim Hnia[8], Raphaël Margueron[5], Dominik Lutter[9,10], Takeaki Ozawa[3] & Ganna Panasyuk[1,2]

Transcriptional remodelling during fasting ensures metabolic adaptation and provides health benefits across species. Although several regulators of fasting-induced transcription and chromatin are known, how nutrient levels directly influence RNA polymerase II (RNAPII) and epigenetic writers remains unclear. Here we show that lipid kinase class 3 phosphatidylinositol 3-kinase (PI3K-3), a master regulator of autophagy, also functions on chromatin as a co-activator of epigenetic writers to promote RNAPII transcription. PI3K-3 overlaps with transcriptionally engaged RNAPII phosphorylated at Ser5 and with Setd1a/COMPASS, the complex that deposits the activating H3K4me3 mark. Nuclear PI3K-3 interacts with RNAPII and Setd1a/COMPASS and promotes their chromatin binding. PI3K-3 loss reduces RNAPII-S5p and H3K4me3 at selected genes, whereas PI3K-3 overexpression co-activates p300/CBP and chromatin-targeted PI3K-3 increases H3K4me3. During starvation, PI3K-3 induces autophagy genes and drives fasted liver towards ketogenesis and lipid degradation. These findings link nutrient stress to chromatin-mediated transcriptional activation.

The induction of specific gene programmes ensures survival under energy stress, but how information such as nutrient fluctuation is relayed to epigenetic writers for RNAPII transcription remains understudied[1]. The fundamental property of coupling nutrient sensing with transcription emerged at the onset of cellularity; exemplified by operon activity in prokaryotes and ligand-activated transcription factor nuclear receptors in metazoan[2]. While these mechanisms address how metabolites directly act on transcriptional machinery, they fall short to resolve the complexity of epigenomic and transcriptomic remodelling that takes place under nutrient stress, such as fasting. Our study attempts to fill this gap by demonstrating that nutrient signalling effectors functionally interact on chromatin with epigenetic writers and RNAPII. In multicellular organisms, hormones and nutrient sensing signalling pathways coordinate transcriptional remodelling to assure metabolic adaptation to starvation. Among these nutrient-responsive effectors, class 3 phosphatidyl-inositol-3 kinase (PI3K-3) is particularly well positioned to couple nutrient availability to cellular adaptation. Functional in all eukaryotes, PI3K-3 is an obligatory lipid kinase complex composed of

[1]Institut Necker-Enfants Malades, INSERM U1151/CNRS UMR 8253, Paris, France. [2]Université de Paris Cité, Paris, France. [3]Department of Chemistry, School of Science, University of Tokyo, Tokyo, Japan. [4]Platform for Metabolic Analyses, Structure Fédérative de Recherche Necker, INSERM US24/CNRS, UMS 3633, Paris, France. [5]Institut Curie, Paris Sciences et Lettres Research University, Sorbonne University, INSERM U934/CNRS UMR 3215, Paris, France. [6]Platform for Genome Editing, Structure Fédérative de Recherche Necker, INSERM US24/CNRS, UMS 3633, Paris, France. [7]Platform Bio-Informatique, Université Paris Cité, Structure Fédérative de Recherche Necker, INSERM US24/CNRS UMS 3633, Paris, France. [8]Institute of Cardiovascular and Metabolic Diseases (I2MC), INSERM-UMR 1297, University Paul Sabatier, Toulouse, France. [9]Computational Discovery Research, Institute for Diabetes and Obesity, Helmholtz Diabetes Center, Helmholtz Zentrum München – German Research Center for Environmental Health, Neuherberg, Germany. [10]Division German Center for Diabetes Research, DZD, Neuherberg, Germany. [11]These authors contributed equally: Genki Kawamura, Ying Luo. e-mail: ganna.panasyuk@inserm.fr

https://doi.org/10.1038/s41556-026-02030-7

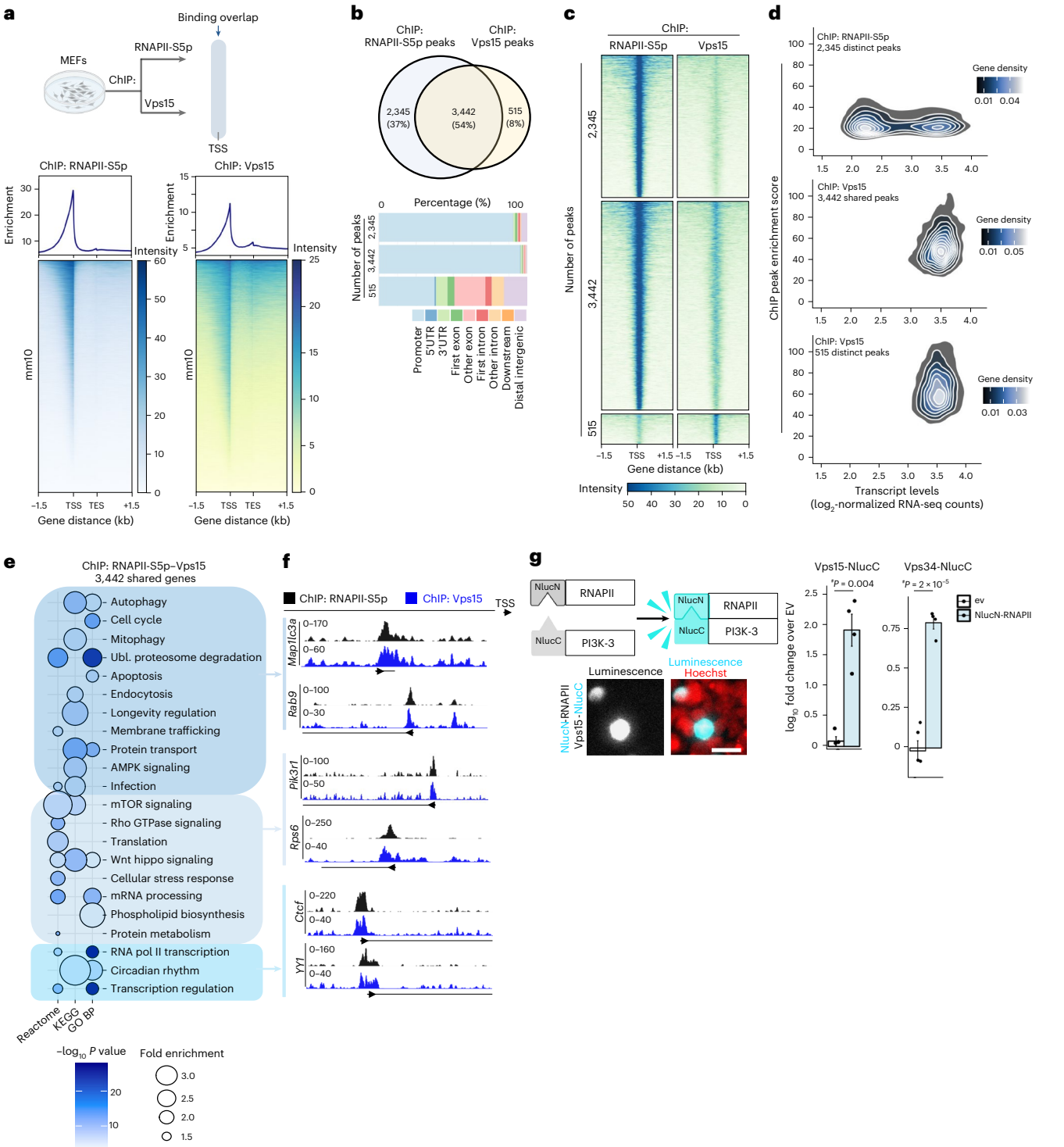

Fig. 1 | PI3K-3 chromatin binding overlaps with RNAPII. a, Top: a schematic diagram of ChIP-RNAPII-S5p and ChIP-Vps15 overlap analysis. ChIP-seq heat maps and profile plots of RNAPII-S5p and Vps15 enrichment in growing MEFs ($n = 2$ independent biological repeats per ChIP, merged bam files per ChIP used for representation). The rows represent genes ordered by signal strength across the mm10 genome, −1.5 kb to +1.5 kb from the TSS and transcription end site (TES). **b**, Venn diagram of unique and shared peaks between RNAPII-S5p and Vps15 determined by Diffbind consensus/differentially-bound peaks ($P < 0.05$, unique peaks; $P > 0.05$, consensus peaks, Deseq2 Wald test). Genomic annotation of shared peaks between RNAPII-S5p and Vps15. **c**, A heat map plotting unique and shared peaks between RNAPII-S5p and Vps15 relative to the TSS. **d**, Gene density plots of $\log_2$ variance stabilized transformation RNA counts in growing MEFs plotted against unique and shared peaks between RNAPII-S5p and Vps15. Peak enrichment scores indicate relative peak intensity determined by MACS2. Gene density indicates number of genes associated with respective peak score. **e**, Reactome, KEGG and GO BP pathway analyses of shared peaks between RNAPII-S5p and Vps15. P-values determined with Fisher's exact test. **f**, RNAPII-S5p and Vps15 enrichment on promoters of indicted genes in respective pathways. Arrow indicates TSS. **g**, A schematic diagram of split-luciferase complementation assay in HEK293T cells overexpressing NlucN-RNAPII and Vps15-NlucC or Vps34-NlucC. Image of bioluminescent signal from partner–pair interaction. Scale bar, 10 µm. Data are $\log_{10}$ fold change versus empty vector (EV) mean ± s.e.m., $^{\#}P < 0.05$ ($n = 4$ independent biological repeats for NlucN-RNAPII with NlucC-Vps15; $n = 5$ independent biological repeats for EV and NlucC-Vps34; $n = 4$ independent biological repeats for NlucN-RNAPII with NlucC-Vps34), Student's two-tailed t-test. Schematics in **a** and **g** created in BioRender; Henneman, N. https://biorender.com/gqhx29q (2026)Source data.

catalytic subunit Vps34 and regulatory subunit Vps15; which is required for Vps34 stability, membrane targeting, and lipid kinase activity[3]. PI3K-3 responds to nutrient availability, including feeding and fasting cues to generate phosphatidyl inositol-3-phosphate (PI3P). The engagement of additional subunits bound to the Vps15-Vps34 core, such as Atg14 or UVRAG, confer PI3K-3 specificity towards nutrient uptake via endocytosis or macromolecule degradation in lysosomes by autophagy[3]. While these cytosolic lipid kinase PI3K-3 complexes enable acute responses to changes in nutrient levels, its involvement in RNAPII transcription for metabolic adaptation remains unexplored. Evidence supporting a nuclear function of PI3K-3 has emerged across several models. In plants and yeast, PI3K-3 promotes RNAPII elongation[4,5]. In animal cells, both Vps34 and Vps15 subunits of PI3K-3 are imported to nucleus and localize to active transcription sites[6]. In mammals, PI3K-3 co-activates the circadian clock transcription factor[6], further supporting a transcriptional regulatory role. Notably, prolonged fasting represents a metabolic stress that relies on RNAPII-driven transcription to induce liver gluconeogenesis and fatty acid oxidation for glucose and ketone release into circulation. Chromatin recruitment of RNAPII parallels daily nutrient fluctuations, suggesting that regulatory mechanisms are in place[7], yet RNAPII regulation remains to be investigated in fasting. Although PI3K-3 activity in autophagy indirectly contributes to transcriptional remodelling during fasting, it is unknown whether the nuclear pool of PI3K-3 directly regulates fasting-induced transcription[8,9]. Together, these observations prompted us to investigate the role of chromatin-associated PI3K-3 for activating RNAPII transcription to support metabolic adaptation to fasting.

Results

PI3K-3 chromatin binding overlaps with RNAPII

To understand the role of PI3K-3 on chromatin, we performed chromatin immunoprecipitation followed by sequencing (ChIP-seq) of Vps15, the essential regulatory subunit of PI3K-3 in growing mouse embryonic fibroblasts (MEFs). To explore involvement of PI3K-3 in active transcription, we coupled it with ChIP-seq of RNAPII phosphorylated on Serine5 (RNAPII-S5p) of its C-terminal domain (CTD). RNAPII-S5p confers proximal-promoter pausing of RNAPII, engaged in early elongation[10,11]. As expected, RNAPII-S5p was enriched at the transcription start site (TSS) and promoter, and strikingly, Vps15 showed a nearly identical binding profile (Fig. 1a and Extended Data Fig. 1a). Accordingly, differential binding analysis showed an overlap of 3,442 consensus peaks shared between Vps15 and RNAPII-S5p, while 2345 and 515 peaks were distinct to RNAPII-S5p and Vps15, respectively (Fig. 1b,c and Extended Data Fig. 1b). The peaks shared between Vps15 and RNAPII-S5p as well as RNAPII-S5p distinct peaks almost entirely resided within promoters (Fig. 1b). However, Vps15 distinct peaks were additionally mapped to intronic, exonic and distal intergenic regions (Fig. 1b). By integrating the ChIP analyses with RNA-seq from growing MEFs, we found that Vps15 binding mapped to highly expressed genes (both Vps15 distinct and shared RNAPII-S5p peaks), whereas RNAPII-S5p distinct peaks were distributed between high and low expressed genes (Fig. 1d). Pathway analysis of shared RNAPII-S5p and Vps15 genes pointed to a wide range of cellular processes. Vps15 was enriched at promoters of key genes involved in autophagy, trafficking, signalling, metabolism and transcriptional regulation, highlighting the breadth of potential transcriptionally regulated pathways by PI3K-3 (Fig. 1e,f and Extended Data Fig. 1c). Given the similarity of RNAPII-S5p and Vps15 chromatin binding profiles, we investigated their interaction. Notably, while nuclear Vps15 and Vps34 levels were minor compared with the cytosol (Extended Data Fig. 1d,e), immunofluorescent microscopy showed co-localization of Vps15 and RNAPII (Extended Data Fig. 1f). Split-luciferase complementation assays in live cells further showed close proximity between RNAPII and both PI3K-3 subunits (Vps15 and Vps34), suggesting a direct and specific interaction (Fig. 1g and Extended Data Fig. 1g). In addition, immunoprecipitation of RNAPII from nuclear extracts pulled down both Vps15 and Vps34 (Extended Data Fig. 1h), while truncation or deletion of the regulatory CTD of RNAPII[12] weakened this binding (Extended Data Fig. 1h). Inversely, N-terminal truncation of Vps15, that destabilizes the PI3K-3 complex in Vps15KO MEFs[13], was also sufficient to impair the Vps15 RNAPII interaction (Extended Data Fig. 1i). Altogether, these findings suggest that chromatin bound PI3K-3 is involved in RNAPII mediated transcription.

PI3K-3 induces chromatin enrichment of RNAPII-S5p and H3K4me3

H3K4me3 is a histone methylation mark that controls RNAPII proximal-promoter pause release, RNAPII promoter half-life and transcription elongation[14]. H3K4me3 is deposited on transcriptionally active genes via the Setd1a/COMPASS methyltransferase complex[15]. Thus, we next investigated whether PI3K-3 regulates RNAPII through H3K4me3. Analyses of published Setd1a chromatin binding in MEFs revealed a striking overlap with Vps15 (Fig. 2a and Extended Data Fig. 2a–d). The majority of Vps15 and Setd1a shared peaks also mapped to highly expressed genes, and those common between Vps15 and RNAPII-S5p (Extended Data Fig. 2d–f). Co-immunoprecipitation and split-luciferase complementation assays showed that nuclear PI3K-3 interacts with subunits of Setd1a/COMPASS and is proximally present to its nucleosome substrate (Fig. 2b,c and Extended Data Fig. 3a,b). To further support the interaction between RNAPII-S5p, Setd1a/COMPASS and PI3K-3 on chromatin, we adapted CUT&RUN for immunoprecipitation analyses. For this, CUT&RUN was performed with antibodies against RNAPII-S5p and its eluates were then subjected to immunoprecipitation with anti-Vps15 antibodies. Notably, Setd1a/COMPASS subunits, Wdr5 and Wdr82, were detected in Vps15 immunoprecipitates from RNAPII-S5p-bound fragments (Extended Data Fig. 3c). Next, we asked if overexpression of PI3K-3 subunits impacts enrichment of RNAPII-S5p and H3K4me3. Overexpression of either Vps15 or Vps34 did not alter global RNAPII-S5p occupancy across the genome (Extended Data Fig. 3d,e). However, Vps15 overexpression specifically induced RNAPII-S5p enrichment in 1,886 regions corresponding to 1,723 genes, whereas Vps34 included enrichment on 2,268 regions in 2,066 genes (Fig. 2d and Extended Data Fig. 3f). Moreover, 323 shared genes gained RNAPII-S5p enrichment in cells overexpressing either Vps15 or Vps34 (Extended Data Fig. 3g). Furthermore, unlike for RNAPII-S5p, Vps15 overexpression increased global H3K4me3 enrichment resulting in induction of 6,927 peaks (assigned to 5,435 genes) (Fig. 2d and Extended Data Fig. 3d,h,i). Among the impacted regions in Vps15-overexpressing cells, 475 genes, corresponding to induced peaks, were shared between RNAPII-S5p and H3K4me3 datasets (Fig. 2e). Pathway analyses of these 475 genes highlighted chromatin organization, transcriptional regulation and methionine metabolism (Fig. 2f). These findings suggest that PI3K-3 may function as a co-activator of RNAPII-S5p by promoting H3K4me3 deposition.

Methionine-dependent H3K4me3 deposition and RNAPII recruitment require PI3K-3

H3K4me3 deposition on active genes is facilitated via the binding of Setd1a/COMPASS and RNAPII CTD[16], prompting us to ask if PI3K-3 impacts their interaction. H3K4me3 is a labile histone mark[17], making its turnover sensitive to methionine levels and a universal methyl group donor, *S*-adenosyl-L-methionine (SAM) (Fig. 3a,b). Consistently, 4-h methionine deprivation in MEFs reduced SAM availability and decreased cellular methylation capacity reflected in reduced ratio of SAM to *S*-adenosyl-L-homocysteine (SAH), resulting in a reduction of global H3K4me3 (Fig. 3b,c). Methionine replenishment rescued cellular methylation capacity and restored H3K4me3 levels via de novo methylation (Fig. 3a–c). Thus, extracellular methionine deprivation/replenishment represents an approach to model de novo H3K4me3 deposition and investigate recruitment of transcriptional complexes on chromatin. To test this, we employed the

https://doi.org/10.1038/s41556-026-02030-7

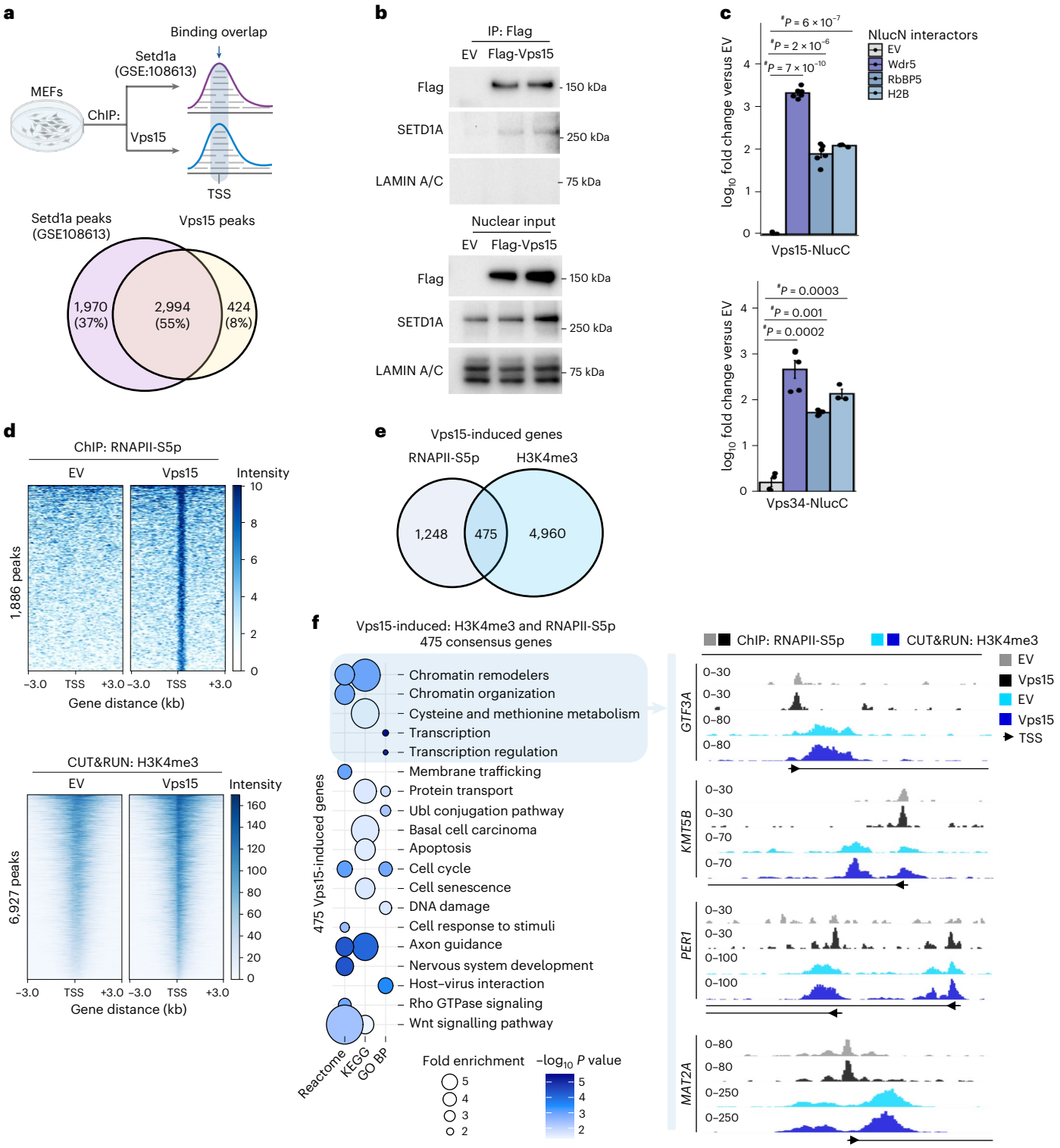

Fig. 2 | PI3K-3 induces chromatin enrichment of RNAPII-S5p and H3K4me3. **a**, Top: a schematic diagram of ChIP-Setd1a (GSE:108613) and ChIP-Vps15 overlap analysis. Venn diagram of unique and shared peaks between Setd1a and Vps15 determined by Diffbind consensus/differentially-bound peaks ($P < 0.05$, unique peaks; $P > 0.05$, consensus peaks; $n = 2$ independent biological repeats for ChIP-Vps15). **b**, Immunoblot of Flag-Vps15 immunoprecipitated complexes from HEK293T cells, probed with indicated antibodies. **c**, Split-luciferase complementation assay in HEK293T cells overexpressing Vps15-NlucC or Vps34-NlucC with either NlucN-Wdr5, NlucN-RbBP5 or NlucN-H2B. Data are mean ± s.e.m., $^{\#}P < 0.05$ (Vps15-NlucC: $n = 6$ independent biological repeats for NlucN-Wdr5 and NlucN-RbBP5, $n = 3$ independent biological repeats for NlucN-H2B; Vps34-NlucC: $n = 5$ independent repeats for NlucN-Wdr5 and NlucN-RbBP5, $n = 3$ independent biological repeats for NlucN-H2B), Student's two-tailed t-test versus empty vector (EV). **d**, Heat maps of RNAPII-S5p and H3K4me3 peaks induced by Vps15 overexpression identified by Bdgdiff differential binding with peak score fold change >1 between Vps15 versus EV overexpression. **e**, Venn overlap between Vps15-induced RNAPII-S5p and H3K4me3 genes with fold change >1. **f**, Reactome, KEGG and GO BP pathway analysis of overlapping Vps15-induced RNAPII-S5p and H3K4me3 genes and indicated example gene tracks. P values determined with Fisher's exact test. Schematic in **a** created in BioRender; Henneman, N. https://biorender.com/gqhx29q (2026).

https://doi.org/10.1038/s41556-026-02030-7

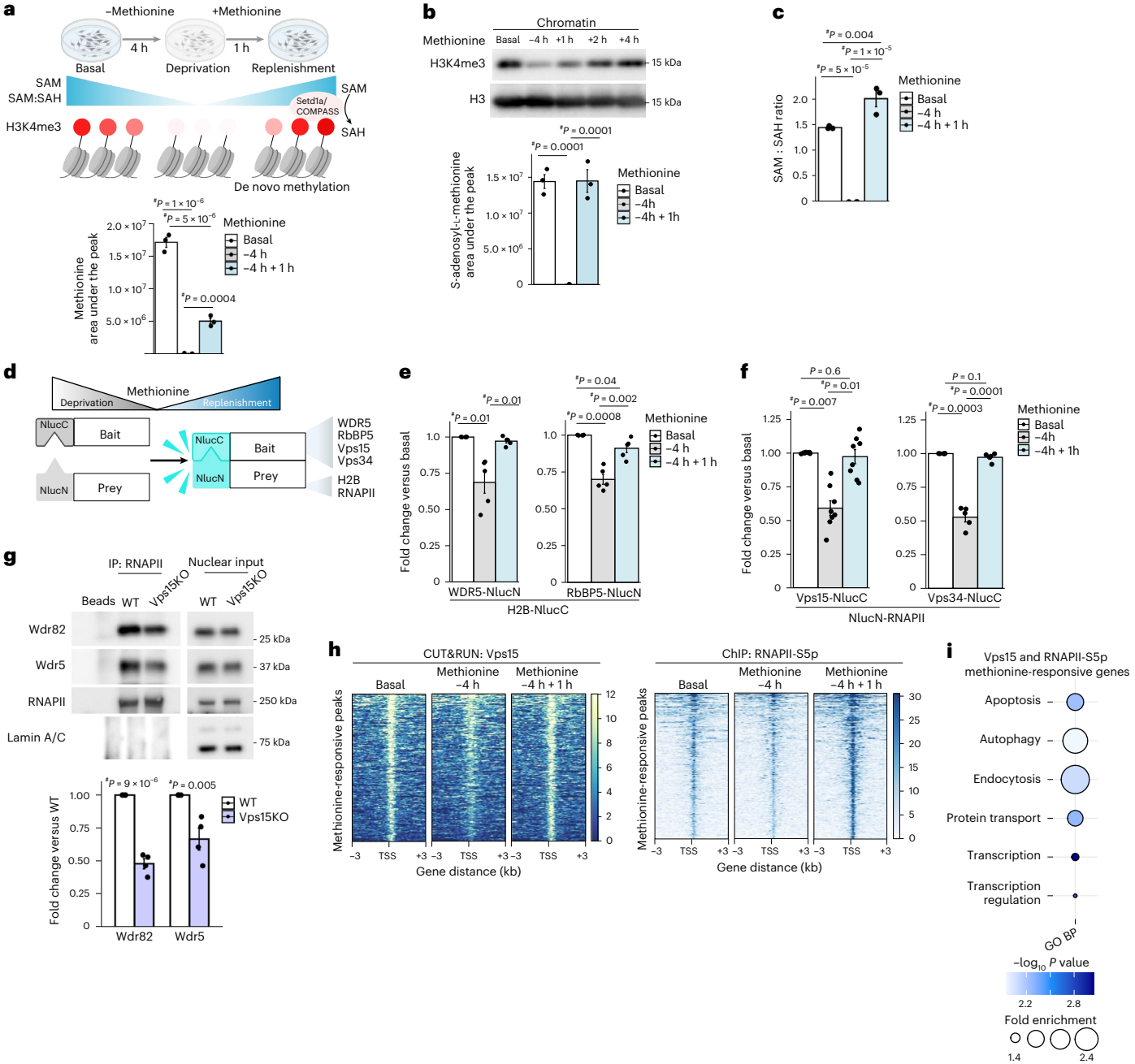

Fig. 3 | PI3K-3 engages in de novo H3K4me3 establishment. a, A schematic diagram of methionine deprivation and replenishment and its impact on SAM:SAH and H3K4me3 levels. Colour saturation is illustrative of metabolite levels. Bottom: LC–MS of L-methionine in nuclear extracts of MEFs under methionine deprivation (−4 h) followed by methionine replenishment (+1 h). Data are mean ± s.e.m., $^{\#}P < 0.05$ ($n = 3$ independent biological repeats), one-way ANOVA with Benjamini–Hochberg correction. **b**, Top: immunoblot of MEFs under methionine deprivation (−4 h) followed by methionine replenishment (+1 h, +2 h, +4 h) probed with indicated antibodies. Bottom: LC–MS in nuclear extracts of MEFs under methionine deprivation (−4 h) followed by methionine replenishment (+1 h). Data are mean ± s.e.m., $^{\#}P < 0.05$ ($n = 3$ independent biological repeats), one-way ANOVA with Benjamini–Hochberg correction. **c**, Nuclear SAM:SAH ratio derived from LC–MS in nuclear extracts of MEFs under methionine deprivation (−4 h) followed by methionine replenishment (+1 h). Data are mean ± s.e.m., $^{\#}P < 0.05$ ($n = 3$ independent biological repeats), one-way ANOVA with Benjamini–Hochberg correction. **d**, A schematic diagram of split-luciferase complementation assay in conditions of methionine deprivation and replenishment. **e**, Split-luciferase complementation assay in HEK293T cells expressing H2B-NlucC with either WDR5-NlucN or RbBP5-NlucN that were either kept in compete media (basal), were methionine deprived (−4 h) or followed by methionine replenishment (+1 h). Data are fold change versus basal mean ± s.e.m., $^{\#}P < 0.05$ ($n = 5$ independent biological repeats), one-way ANOVA with Benjamini–Hochberg correction. **f**, Split-luciferase complementation assay in HEK293T cells expressing NlucN-RNAPII with either Vps15-NlucC or Vps34-NlucC treated as in **e**. Data are fold change versus basal mean ± s.e.m., $^{\#}P < 0.05$ ($n = 8$ independent repeats for Vps15-NlucC, $n = 5$ independent biological repeats for Vps34-NlucC), one-way ANOVA with Benjamini–Hochberg correction. **g**, Immunoblot of RNAPII immunoprecipitated complexes from nuclei of Vps15$^{f/f}$ MEFs transduced with either adeno-GFP (WT) or adeno-CRE (Vps15KO), probed with respective antibodies. Densitometric analysis shows mean ± s.e.m. of Wdr82 or Wdr5 fold change versus WT normalized to RNAPII signal. $^{\#}P < 0.05$ ($n = 4$ independent biological repeats), Student's two-tailed t-test. **h**, Heat maps of methionine responsive genes identified in Vps15 CUT&RUN-seq and RNAPII-S5p ChIP-seq identified with Diffbind comparing genes showed reduced binding between basal versus methionine −4 h and genes that increased in binding between methionine −4 h and methionine −4 h + 1 h at a threshold of $P < 0.05$. **i**, GO BP pathway analysis of Vps15- and RNAPII-S5p-methionine responsive genes from **h**. P values determined with Fisher's exact test. Schematics in **a** and **d** created in BioRender; Henneman, N. https://biorender.com/gqhx29q (2026).

split-luciferase complementation assay (Fig. 3d). Notably, the interaction of Setd1a/COMPASS subunits (WDR5 and RbBP5) with H2B was reduced in methionine-deprived cells and recovered by methionine supplementation (Fig. 3e). This was backed by methionine-sensitive interaction in co-immunoprecipitation between subunits of the Setd1a/COMPASS complex, WDR5 and SETD1A (Extended Data Fig. 4a). Surprisingly, a similar methionine-sensitive pattern was observed for Vps15 pulled down in WDR5 complexes (Extended Data Fig. 4a). Supporting this, the split-luciferase complementation assay showed a methionine-sensitive interaction between PI3K-3 subunits and RNAPII (Fig. 3f). To note, methionine deprivation/replenishment did not alter nuclear levels of the PI3K-3 subunits (Extended Data Fig. 4b). Moreover, binding between RNAPII and Setd1a/COMPASS was decreased in Vps15-depleted cells (Fig. 3g). Altogether, these support PI3K-3 involvement in Setd1a/COMPASS-RNAPII-mediated transcriptional regulation, prompting us to investigate PI3K-3 gene targets coupled with H3K4me3 turnover. For this we performed CUT&RUN-sequencing of Vps15 and ChIP-sequencing of RNAPII-S5p in MEFs under methionine deprivation and replenishment. Notably, TSS recruitment of Vps15 and RNAPII-S5p were largely unmodified by methionine deprivation but were induced by methionine supplementation (Extended Data Fig. 4c). However, differential binding analysis comparing conditions of basal versus methionine deprivation showed reduced binding in 217 peaks for Vps15 and in 333 peaks for RNAPII-S5p (Extended Data Fig. 4d). Moreover, methionine replenishment induced 256 Vps15 peaks and 417 RNAPII-S5p peaks (Extended Data Fig. 4d). These peaks constituted a subset of genes to which Vps15 and RNAPII-S5p were co-recruited in methionine-sensitive manner (Fig. 3h). Pathway analyses of Vps15 and RNAPII-S5p-bound methionine-responsive genes highlighted processes potentially under transcriptional control of PI3K-3; such as autophagy, endocytosis, protein transport and transcription regulation (Fig. 3i). A direct role of PI3K-3 in autophagy gene transcription was further supported by methionine-sensitive occupancy of RNAPII-S5p and Vps15 on autophagy-related genes such as *Sqstm1*, *Gabarapl2* and *Nrp1* (Extended Data Fig. 4e). More globally, Vps15 read densities across H3K4me3 methionine sensitive peaks demonstrate increased Vps15 enrichment in methionine replenishment conditions, coinciding with de novo H3K4me3 deposition (Extended Data Fig. 4f,g). These findings of H3K4me3 reinstallation point to PI3K-3 as a co-activator of Setd1a/COMPASS and RNAPII for transcriptional remodelling under amino acid deprivation.

PI3K-3 promotes transcription of autophagy related genes

Next, to establish a PI3K-3 dependent transcriptome, we performed RNA-sequencing in $Vps15^{f/f}$ MEFs transduced with either adeno-GFP (wild type, WT) or adeno-CRE (Vps15KO) followed by methionine deprivation and replenishment. Principal component analysis (PCA) plot of the transcriptional response to methionine in highlighted a segregation between genotype and methionine conditions, driven by 936 methionine-responsive genes in WT cells that were dysregulated in Vps15KO MEFs and contributed to PC1 and PC2 segregation (Fig. 4a and Extended Data Fig. 5a). The PI3K-3 dependent methionine responsive genes belonged to pathways encompassing transcription regulation, cell cycle regulation, sterol and lipid metabolism (Fig. 4b). The role of PI3K-3 in transcriptional induction upon methionine replenishment was further supported by an increased number of downregulated genes in Vps15KO cells, rising from 309 genes at 1 h to 477 genes at 4 h (Extended Data Fig. 5b). Gene set enrichment analysis revealed a defective transcriptional response to methionine in Vps15KO cells, with disrupted transcription regulation, metabolic and cell stress response pathways (Extended Data Fig. 5b). Combining transcriptomic analyses with methionine sensitive cistromes of Vps15 and RNAPII-S5p, we found that RNAPII-S5p was largely confined to high expressed genes upon methionine replenishment while Vps15 was associated with both high and low expressed genes (Extended Data Fig. 5c). Interestingly, genomic analyses consistently pointed to PI3K-3 as potential transcriptional activator of the autophagy-related genes (Figs. 1e and 3i and Extended Data Figs. 1c, 3g and 4e). To extend these findings to a pro-autophagy context, we performed RNA-seq in WT and Vps15KO MEFs subjected to EBSS treatment, a starvation-mimicking media that lacks amino acids and is low in glucose. In response to EBSS, WT cells induced 573 genes and downregulated 896 genes,whereas Vps15KO MEFs displayed induction of 576 genes and downregulation of 870 genes compared to WT cells (Extended Data Fig. 5d). This was accompanied by a dysregulated transcriptome even in basal conditions between WT and Vps15KO cells (Extended Data Fig. 5d). Notably, 255 genes were EBSS-responsive in WT cells and this EBSS response was dysregulated in Vps15KO cells (Fig. 4c). Gene Ontology Biological Processes (GO BP) pathway analyses showed that these 255 genes were enriched in cellular stress response and RNAPII transcription processes (Fig. 4d). These transcriptomic findings were corroborated at autophagy-related genes which were iduced by EBSS in WT MEFs but showed defective or delayed activation in Vps15KO cells (Fig. 4e). Of note, EBSS treatment did not affect nuclear levels of PI3K-3 subunits (Extended Data Fig. 5e). Finally, supporting the role of PI3K-3 for transcriptional adaptation to amino acid deprivation, Vps15KO MEFs showed a reduction in H3K4me3 and RNAPII-S5p at the promoters of Vps15-dependent methionine-sensitive autophagy genes (Fig. 4f). Altogether, these findings position PI3K-3 as a transcriptional activator that links amino acid availability to H3K4me3 and RNAPII-S5p-mediated transcription.

PI3K-3 is required for fasting-induced chromatin recruitment of RNAPII in mouse liver

To explore the in vivo role of PI3K-3 in fed-to-fast transcriptional remodelling, we performed RNA-seq in livers from control mice (WT) and mice with acute Vps15 depletion (Vps15iLKO)[6,13]. Liver tissue was collected at the onset of active feeding in ad lib fed mice or after 24 h of fasting (Fig. 5a). Fasting in WT mice drove PC2 segregation in the principal component analysis (Fig. 5b). In WT mice, fasting resulted in differential expression of 6,571 genes that were up- or downregulated in similar proportions (Fig. 5c). While no global changes in RNAPII-S5p or H3K4me3 were observed, robust transcriptional activation in livers of fasted WT mice coincided with increased recruitment of RNAPII-S5p (1,580 peaks) and gained enrichment of H3K4me3 (1,651 peaks) (Extended Data Fig. 6a,b). Remarkably, PI3K-3 inactivation blunted the fasting transcriptional response, with only ~10% of fasting-induced genes showing changes in livers of Vps15iLKO mice (Fig. 5c). The transcriptional impairment in livers of Vps15iLKO mice was accompanied by diminished RNAPII-S5p recruitment and defective fasting-induced H3K4me3 enrichment (Fig. 5d,e and Extended Data Fig. 6c). Notably, PI3K-3 depletion resulted in unmodified nuclear RNAPII-S5p or H3K4me3 (Extended Data Fig. 6d,e). Yet, fasting led to a slight reduction in total RNAPII and PI3K-3 nuclear levels in livers of WT mice (Extended Data Fig. 6d). To explore how fasting impacts PI3K-3 chromatin distribution, we performed ChIP-seq of Vps15 in livers of fed and fasted WT mice. Despite a modest decrease in protein levels of PI3K-3 core subunits in nuclear extracts of fasted WT mice, fasting promoted Vps15 enrichment at TSS regions, introns and exons (Fig. 5f and Extended Data Fig. 6d,f). Notably, fasting increased Vps15 chromatin recruitment on 895 peaks (Extended Data Fig. 6g). Consistently, RNAPII-S5p and H3K4me3 enrichment in these 895 Vps15-bound peaks were decreased in livers of fasted Vps15iLKO mice (Extended Data Fig. 6h). Moreover, 895 Vps15-bound fasting peaks were distributed between high and low expressed genes (Extended Data Fig. 6i). In line with their implication in active transcription, the 2001 RNAPII-S5p and 2106 H3K4me3 peaks, identified as fasting-induced and PI3K-3-dependent, were predominantly mapped to highly expressed genes (Fig. 5d,e and Extended Data Fig. 6i). Fasting-induced peaks with reduced chromatin enrichment of RNAPII-S5p and H3K4me3 in livers of fasted

https://doi.org/10.1038/s41556-026-02030-7

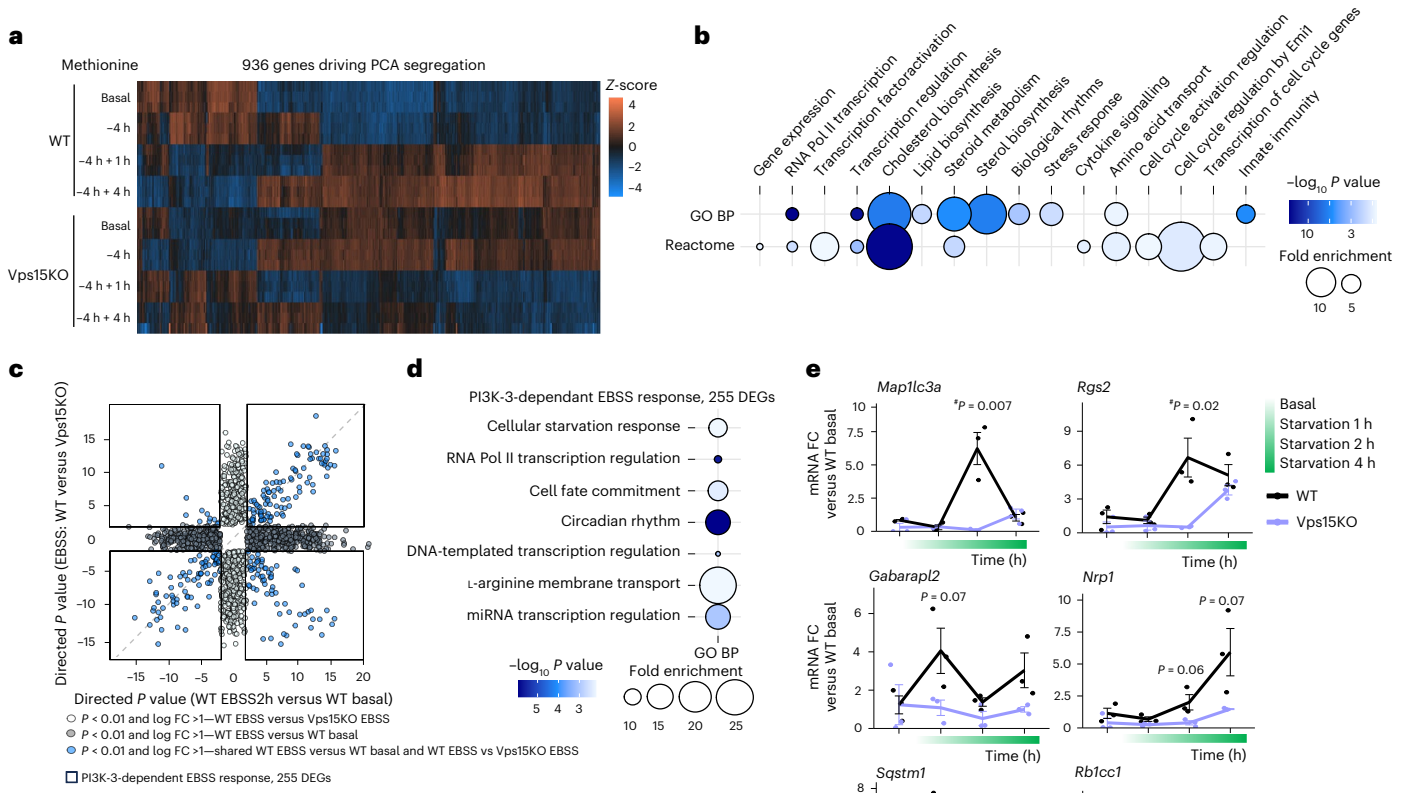

Fig. 4 | PI3K-3 promotes transcription of autophagy related genes. a, Heat map shows transcriptional changes in 936 methionine-responsive genes driving PC1 and PC2 segregation in Vps15$^{f/f}$ MEFs transduced with either adeno-GFP (WT) or adeno-CRE (Vps15KO) in response to methionine deprivation (−4 h) followed by methionine replenishment (+1 h or +4 h) ($n = 3$ independent biological repeats). DEGs are listed in Supplementary Table 1. **b**, GO BP and Reactome pathway analysis on 936 methionine-responsive genes from **a**. *P* values determined with Fisher's exact test. **c**, Comparative transcriptomics plotting directed *P* values <0.01 of limma DEG in indicated comparisons. All dots represent log fold change (FC) >1, and colours of dots represent shared or unique genes to the respective comparisons. Black squares surrounding blue dots highlight PI3K-3-dependent EBSS-responsive genes that are overlapping between WT EBSS versus WT Basal and WT EBSS versus Vps15KO EBSS. Comparative transcriptomics DEGs are listed in Supplementary Table 1. **d**, GO BP pathway analysis of PI3K-3-dependent EBSS-responsive genes from **c**. *P* values determined with Fisher's exact test. **e**, RT–qPCR of indicated genes in WT and Vps15KO MEFs treated with EBSS for the indicated times. Data are mean ± s.e.m. expression fold change versus untreated (basal) condition. $^{\#}P < 0.05$ ($n = 3$ independent biological repeats) shows comparison between WT and Vps15KO respective timepoint, two-way ANOVA with Benjamini–Hochberg correction. **f**, CUT&RUN–qPCR of RNAPII-S5p or H3K4me3 on indicated genes in WT or Vps15KO MEFs. Data are mean ± s.e.m. fold change of either RNAPII-S5p or H3K4me3 enrichment normalized to IgG versus WT cells, $^{\#}P < 0.05$ ($n = 3$ independent biological repeats); Student's two-tailed *t*-test.

Vps15iLKO mice were mapped to genes exclusively involved in metabolic processes such as lipid and amino acid metabolism (Fig. 5g). Beyond fasting, fed Vps15iLKO mice displayed impaired transcription programmes for steroid hormone synthesis and one carbon metabolism (Extended Data Fig. 6j). Notable examples of fasting-induced peaks included gluconeogenesis (*Pck1* and *G6pc*), fatty acid oxidation and ketogenesis (*Cpt1a* and *Hmgcs2*), insulin signalling (*Igfbp1*) and amino acid metabolism (*Tat*, *Mat1a*, *Ahcy* and *Sds*) (Fig. 5g and Extended Data Fig. 7a,b). Similar to in MEFs, Vps15 binding profiles in liver mirrored RNAPII-S5p and H3K4me3 in these gene regions (Fig. 1f and Extended Data Fig. 7a). Concurrent with pattern of RNAPII-S5p and H3K4me3 enrichment, respective gene transcripts induced by fasting in livers of WT mice were non-responsive in Vps15iLKO (Fig. 5h,i and Extended Data Fig. 7a,b). Gene set enrichment analysis reinforced the

genomic findings, highlighting impaired transcriptional responses in lipid catabolism, amino acid metabolism and methionine metabolism in livers of fasted Vps15iLKO mice (Extended Data Fig. 7c). These were supported by metabolomics analyses showing defects in fatty acid metabolism, redox reactions, amino acid metabolism and decreased levels of the ketone, 3-hydroxybutyric acid, in livers of fasted Vps15iLKO mice (Extended Data Fig. 8a,b). Key genes in the methionine cycle metabolic pathway (*Mat1a*, *Ahcy*, *Cth* and *Tat*) were consistently induced in livers of fasted WT mice in a PI3K-3-dependent manner (Fig. 5i and Extended Data Fig. 7a). Furthermore, in livers of WT mice, methionine and SAM levels, were decreased with fasting; indicative of active metabolic flux (Fig. 5i). By contrast, Vps15iLKO mice showed elevated levels of both metabolites, with SAM remaining largely unchanged upon fasting (Fig. 5i). Next, quantitative liquid chromatography–mass spectrometry (LC–MS) of nuclear liver extracts from fasted WT mice showed a reduction in SAM, with ~20 ng mg^{-1} wet liver remaining (Extended Data Fig. 8c). This nuclear SAM pool in livers of fasted WT mice was estimated at ~50–70 µM, which lies above the reported K_m range for Set1-family domain containing methyltransferases and is consistent with sustained methyltransferase activity in the presence of the Wdr5, Rbbp5, Ash2l and Dpy30 (WRAD) subunits[18,19]. Consistently, methylation capacity reflected in SAM:SAH ratio, was maintained in livers of fasted WT mice (Extended Data Fig. 8d). Notably, in fasted Vps15iLKO livers, nuclear SAM and nuclear SAM:SAH ratios were comparable to fasted WT, consistent with PI3K-3 involved in nuclear SAM utilization (Extended Data Fig. 8d). To further test contribution of PI3K-3 to nuclear SAM abundance, we performed ^{13}C-methionine tracing in Vps15KO and WT MEFs following methionine depletion/replenishment. Importantly, nuclear methionine recovered similarly in WT and Vps15KO cells, while nuclear SAM and SAM:SAH ratio were fully restored to pre-depletion levels in WT cells but remained reduced in Vps15KO cells (Fig. 5j,k). These differences in methionine flux to nuclear SAM were associated by unchanged cytosolic and nuclear Mat2a protein levels (Extended Data Fig. 8e). Together, these transcriptomic and metabolomic data support a model in which chromatin-bound PI3K-3 promotes fasting-induced transcriptional remodelling and sustains nuclear SAM dynamics for histone methylation.

Nuclear PI3K-3 engages in hepatic transcriptional networks

To test whether nuclear PI3K-3 engages fasting-dependent protein networks in fed versus fasted mice, we performed Vps15 immunoprecipitation from liver nuclear extracts followed by quantitative mass spectrometry (Fig. 6a and Supplementary Table 1). We identified 156 fed-enriched, 107 fasted-enriched and 372 shared nuclear Vps15 interactors (Fig. 6a). Both Vps15 (*Pik3r4*) and Vps34 (*Pik3c3*) were among the enriched proteins unmodified by fasting, in line with the nuclear PI3K-3 complex (Fig. 6b,c). Although some interactor subsets were fed/fast-enriched, most transcription- and chromatin-associated factors were found in both conditions (Fig. 6b,c). Restricting the analysis to nuclear proteins, GO Component and STRING analyses showed enrichment for core RNAPII transcription and chromatin assemblies, including COMPASS subunits (Wdr5, Wdr82 and Rbbp5) and mediator-associated proteins (Fig. 6d). Notably, Mat1a emerged as a fasting-induced nuclear Vps15 interactor (Fig. 6b,c), suggesting a potential link between PI3K-3 assemblies and local SAM-generation. We validated the Vps15-mediator association by co-IP (Fig. 6e). Moreover, consistent with a stabilizing role of PI3K-3, mediator/RNAPII interactions were weakened in Vps15KO MEFs compared with control cells (Extended Data Fig. 8f). Together, these findings suggest that nuclear PI3K-3 supports the assembly and/or stability of RNAPII-, Setd1a/COMPASS- and mediator-containing transcriptional complexes. Thus, the fasting response reflects regulated chromatin engagement of a pre-existing PI3K-3/Vps15 interactome rather than complex rewiring.

PI3K-3 co-activates Setd1a/COMPASS

To test whether PI3K-3 acts as a transcriptional co-activator, we examined its effect in luciferase transcriptional assays. Active transcription is marked not only by H3K4me3 but also by H3K27ac, mediated by p300/CBP acetyltransferases[20]. Thus, we tested the impact of PI3K-3 overexpression and depletion in conjunction with p300/CBP using a *Mat1a*- and *Mat2a*-luciferase reporters[21,22]. We used *Mat1a* and *Mat2a* gene reporters as they are rate-limiting enzymes in SAM synthesis[23] and were consistently found as targets of chromatin bound PI3K-3 (Figs. 2f and 5h,i). As expected, the overexpression of either p300 or CBP significantly increased activity of both reporters (Fig. 7a and Extended Data Fig. 9a). Supporting its co-activator role, the co-expression of Vps15 with p300/CBP further induced their activation, (Fig. 7a and Extended Data Fig. 9a). The functional involvement of both PI3K-3 subunits, Vps34 and Vps15, was further substantiated by potent co-activation of p300 and CBP on *Mat1a*-luciferase reporter with either subunit (Fig. 7b and Extended Data Fig. 9b). Notably, deletion of the Vps34 lipid kinase domain did not abrogate *Mat1a*-luc co-activation, while transcriptional induction by Vps34 overexpression was lost in the Vps34 C2-domain deletion mutant (Fig. 7b). Given that the Vps34 C2-deletion mutant does not bind to Vps15, these findings back the importance of an intact PI3K-3 complex for its transcriptional function (Fig. 7b,c and Extended Data Fig. 9b). Moreover, in Vps15KO MEFs, in which both PI3K-3 subunits are depleted, p300-dependent *Mat1a*-luc activity was strongly reduced and could only be partially restored by p300 overexpression (Fig. 7d). The functional involvement between PI3K-3, p300/CBP and Setd1a/COMPASS was further supported by Vps15-mediated co-activation of the *Mat1a*-luciferase or *Mat2a*-luciferase reporters that was abolished by inhibiting either p300/CBP acetyltransferases (C646) or Setd1a/COMPASS methyltransferase (OICR) (Fig. 7e and Extended Data Fig. 9c). To directly link the nuclear pool of PI3K-3 to its co-activator activity, we engineered gain-of-nuclear-localization variants by appending a 3×NLS tag to Vps15 or Vps34. In MEFs, Vps15-3×NLS produced only a modest increase in

Fig. 5 | The fasting-induced transcriptome depends on PI3K-3. a, A schematic diagram of the experimental design for fasting response analyses in livers of 12-week-old male Vps15iLKO (KO) and WT mice collected at ZT14 after 24 h of fasting or ad lib fed. **b**, PCA plot of RNA-seq in livers collected as in **a** ($n = 3$ mice per condition). **c**, A heat map showing 6,571 DEGs between Fed WT and Fast WT. The heat map rows are mean *z*-scores of $n = 3$ mice per condition, at fold change >1.5 and *P* value <0.05. Bar chart of DEGs across treatment groups as in **a** at fold change >1.5 and *P* value <0.05. DEGs are listed in Supplementary Table 1. **d**, ChIP-seq heat maps of RNAPII-S5p fasting induced enrichment across indicated conditions as in **a** identified by Diffbind peaks differentially bound at $P < 0.05$, Fast WT versus Fast KO. **e**, ChIP-seq heat maps of H3K4me3 fasting induced enrichment across indicated conditions as in **a** identified by Diffbind peaks differentially bound at $P < 0.05$, Fast WT versus Fast KO. **f**, ChIP-seq Vps15 heat maps and profile plots across the genome in livers of fed and fasted mice ($n = 3$). Rows represent genes ordered by peak signal strength −3 kb to +3 kb from the TSS. **g**, Reactome, KEGG and GO BP pathway analysis of shared between RNAPII-S5p and H3K4me3 and induced in fasting genes dependent on Vps15 identified by Diffbind (Wald test) peaks differentially bound at $P < 0.05$, Fast WT versus Fast KO. *P* values for pathway analysis determined with Fisher's exact test. **h**, Vps15, RNAPII-S5p and H3K4me3 enrichment on *Mat1a* in livers of mice treated as in **a**. **i**, A schematic of the methionine metabolism pathway with indicated RNA-seq normalized counts and normalized nuclear metabolite levels for respective genes and metabolites in livers of mice treated as in **a**. Data are mean ± s.e.m. and $^{\#}P < 0.05$ ($n = 3$ mice per condition), two-way ANOVA with Benjamini–Hochberg correction. **j**,**k**, LC–MS nuclear metabolomics of ^{13}C-methionine, $m+1$-labelled SAM and SAM:SAH ratio in MEFs transduced with either adeno-GFP (WT) or adeno-CRE (Vps15KO). MEFs were methionine deprived for 4 h followed by ^{13}C-methionine replenishment (−4 h + 1 h). Data are mean ± s.e.m. and $^{\#}P < 0.05$ ($n = 3$ independent biological repeats), two-way ANOVA with Benjamini–Hochberg correction. Schematic in **a** created in BioRender Henneman, N. https://biorender.com/gqhx29q (2026).

https://doi.org/10.1038/s41556-026-02030-7

nuclear enrichment relative to WT Vps15 (Extended Data Fig. 9d) and, accordingly, yielded *Mat1a*-luc co-activation similar to untagged Vps15 (Extended Data Fig. 9e). By contrast, Vps34-3×NLS was confined to the nucleus and drove higher *Mat1a*-luc activation than WT Vps34 (Extended Data Fig. 9d,f), indicating that increasing the nuclear PI3K-3 pool can potentiate transcriptional output. Consistently, expression of Vps34-3×NLS enhanced the recruitment of RNAPII-S5p, Setd1a/COMPASS components and H3K4me3 enrichment in previously identified PI3K-3 target genes involved in transcriptional regulation (Fig. 7f). We next examined the contribution of Vps34 lipid kinase

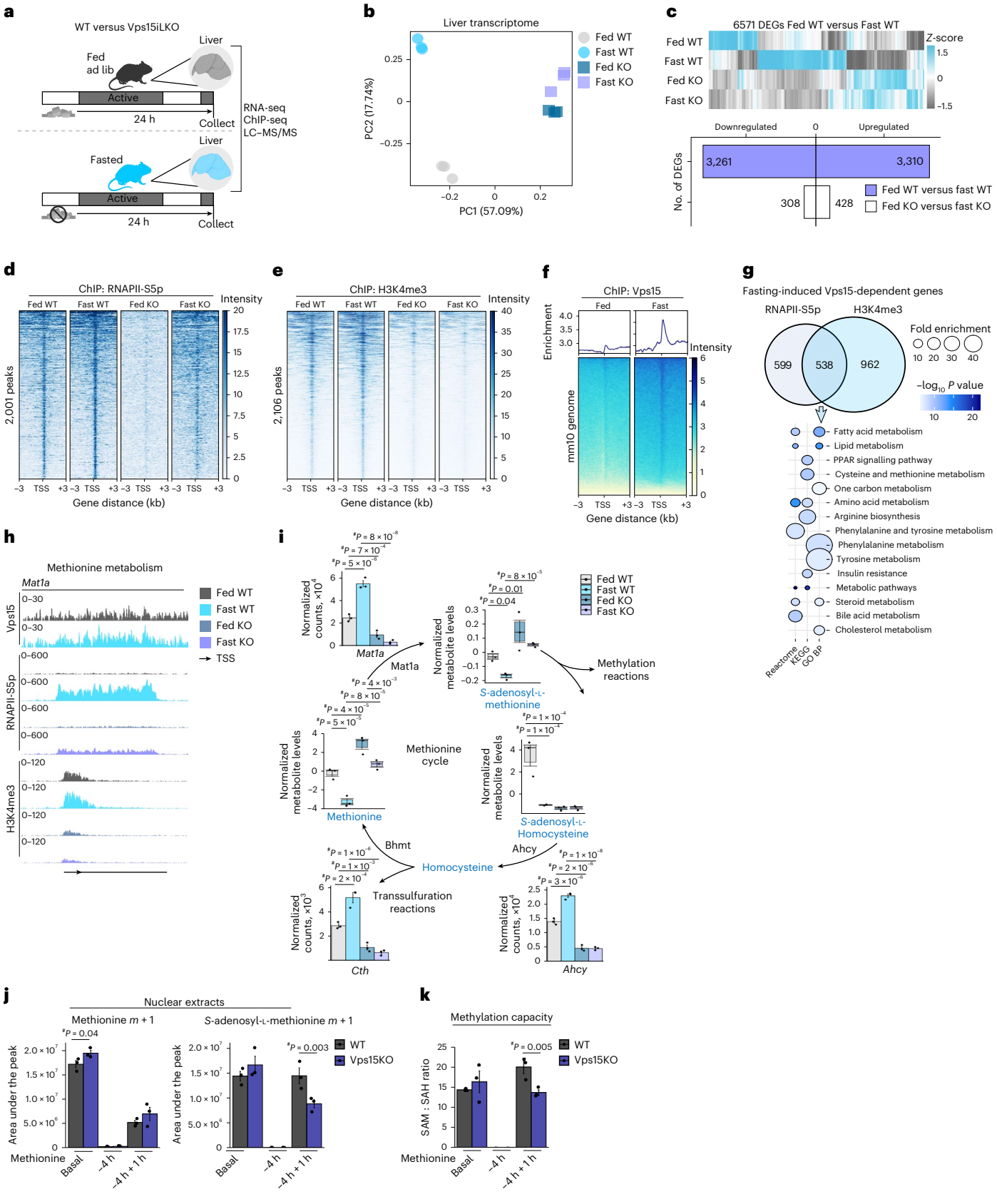

https://doi.org/10.1038/s41556-026-02030-7

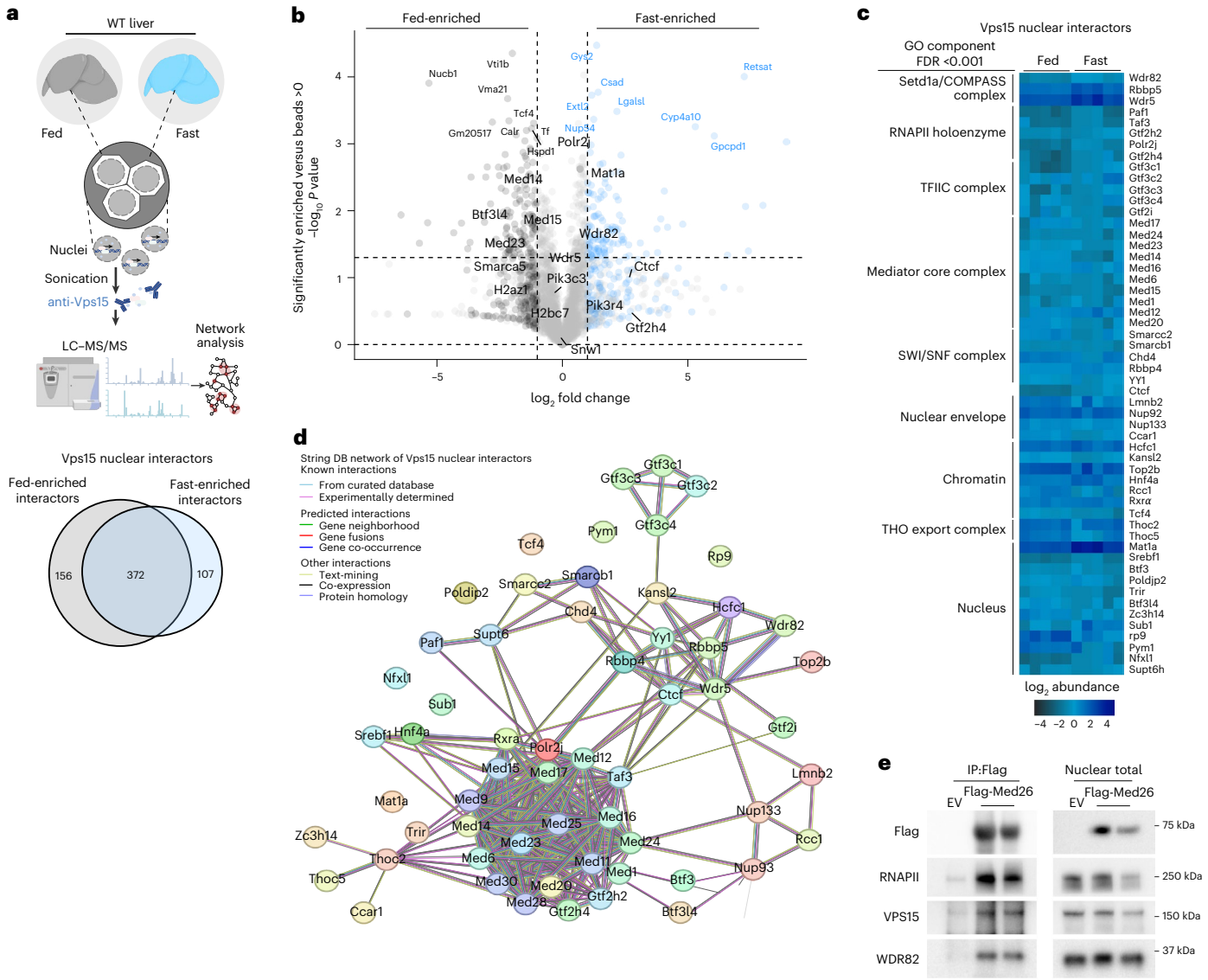

Fig. 6 | Nuclear PI3K-3 engages in hepatic transcriptional networks. a, Top: a schematic diagram of the experimental design for nuclear Vps15 interactome analyses in livers of 12-week-old male Vps15iLKO (KO) and WT mice ($n = 4$ mice per condition) collected at ZT14 after 24 h of fasting or ad lib-fed. Bottom: Venn diagram of proteins pulled-down in Vps15-immunoprecipitates from sonicated nuclei. **b**, Volcano plot of significantly enriched Vps15-immunoprecipitates compared to beads $-\log_{10} P$ value >0 plotted against $\log_2$ fold change >1 between Fed- and Fast-enriched protein abundance. Top eight Fed-enriched interactors shown in light grey; top eight Fast-enriched interactors shown in light blue; and transcriptional machinery and metabolic enzymes are highlighted in dark black. **c**, A heat map of $\log_2$ protein abundance from Vps15-nuclear interactors and GO Component analysis with FDR cutoff <0.001. **d**, STRING DB network analysis of Vps15-nuclear interactors from **c**. **e**, Immunoblot of RNAPII-immunoprecipitates from the nuclear extracts of HEK293T cells expressing Flag-Med26 subunit, probed with indicated antibodies ($n = 2$ independent biological repeats). Schematic in **a** created in BioRender; Henneman, N. https://biorender.com/gqhx29q (2026).

activity to transcriptional output and found that its acute inhibition with Vps34-IN1 abrogated Vps15-driven *Mat1a*-luc co-activation, while kinase-inactive Vps34 mutants—K771A (impaired phosphoinositide binding) and D761A (ATP-binding/catalysis defective)—showed reduced co-activation compared with WT Vps34 (Extended Data Fig. 9g,h). Together, retained activity of Vps34 mutants suggests that PI3K-3 co-activator function is supported by but not reliant on Vps34 lipid kinase input. In sum, these findings further back the direct involvement of PI3K-3 subunits as transcriptional co-activators of epigenetic writers.

PI3K-3 lipid kinase is required for nuclear SAM flux to histone methyl-sinks

Next, we tested how nuclear PI3K-3 lipid kinase activity interfaces with methionine/SAM availability to support transcriptional co-activation. We engineered 3×NLS-methionase to enrich the enzyme in the nucleus and reduce intracellular methionine (Fig. 7g). As expected, LC–MS metabolomic analyses confirmed that methionine was reduced by 70% in 3xNLS-methionase expressing cells, yet it was still present, unlike in cells incubated in media without methionine (Fig. 7h). Moreover, expression of 3xNLS-methionase resulted in decreased methionine levels in both the nucleus and cytosol, indicating the coupling of both pools (Extended Data Fig. 9i). These analyses also showed that nuclear methionine represents a minor pool relative to the cytosol (Extended Data Fig. 9i). In contrast to methionine-free media, intracellular methionine degradation resulted in predominantly higher SAM in the cytosol, while leading to a higher SAM:SAH ratio in both cytosolic and nuclear compartments (Extended Data Fig. 9j,k). This rise in SAM was transient, that would be consistent with exhaustion

of extracellular methionine supply (Extended Data Fig. 9l). It was concomitant with higher ^{13}C-methionine incorporation into SAM ($m+1$), indicating enhanced de novo SAM synthesis in 3×NLS-methionase expressing cells (Extended Data Fig. 9m). Consistent with histones acting as a methylation sink for excess methyl donors[24], the transient SAM increase in 3×NLS-methionase expressing cells coincided with elevated global H3K4me3 and H3K36me3, previously shown to be histone methyl-sinks[25] (Fig. 7i). This response required PI3K-3 lipid kinase activity, as Vps34-IN1 blocked the increase in H3 methylation (Fig. 7i). It also increased the SAM:SAH ratio, consistent with reduced methylation flux despite methyl-donor availability (Fig. 7j). Concordantly, nuclear abundance of Vps15 was unchanged in methionase-expressing cells as compared with not transfected neighbour cells (Extended Data Fig. 9n). Consistent with increased SAM availability, p300-driven *Mat1a*-luc co-activation was further enhanced in methionase-expressing cells and partially reversed by Vps34-IN1 (Fig. 7k). RNA-seq analyses showed broad transcriptional changes in this model, with 2,437 genes contributing to PCA variance of methionase-responsive and Vps34-IN1-sensitive regulation (Extended Data Fig. 9o,p). Moreover, lipid kinase inhibition rendered the methionase-driven transcriptome unresponsive (Fig. 7l and Extended Data Fig. 9p). The methionase-driven transcriptional response at 24 h compared with Vps34-IN1 treatment in methionase-expressed cells showed limited overlap of 290 genes (Fig. 7l). Notably, 452 genes were differentially expressed in methionase expressing cells, but these did not respond to methionase expression under Vps34-IN1 treatment (Fig. 7l). The PI3K-3 lipid kinase-dependent 452 methionase-responsive genes were enriched for GO processes related to regulation of RNAPII transcription and nucleic acid metabolic processes (Fig. 7l). Together, nucleus-directed methionine/SAM perturbation supports a requirement for PI3K-3 lipid kinase activity in coupling methyl-donor flux to histone methylation and transcriptional outputs (Fig. 7m).

PI3K-3 acts on chromatin to promote H3K4me3

Next, to directly test whether PI3K-3 co-activates Setd1a/COMPASS on chromatin, we employed the enzymatically inactive dCas-MINI[26] tool by fusing it to Vps15 or Vps34 (Fig. 8a). We selected gene loci based on H3K4me3 levels in MEFs with some targets showing Vps15 enrichment in liver (Fig. 5h and Extended Data Figs. 7a and 10a). These included *Mat1a* and *Mat2a* loci as both are co-activated by PI3K-3 (Fig. 7a and Extended Data Fig. 9a). Moreover, in proliferating non-hepatocyte MEFs, *Mat1a* gene transcription is silenced while *Mat2a* expression is induced, supported by respective differences in H3K4me3 enrichment at their promoters (Fig. 8b). First, we tested the gain-of-function effect of Vps15 on Setd1a/COMPASS by targeting dCas-MINI-Vps15 to gene loci that already showed H3K4me3 enrichment in MEFs (*Mat2a*, *Fasn* and *Pcx*) (Fig. 8b and Extended Data Fig. 10b). In line with the co-activator role of PI3K-3, Vps15 targeting to promoters of these genes resulted in increased H3K4me3 (Fig. 8c and Extended Data Fig. 10c). Next, we asked if dCas-MINI-Vps15 could promote Setd1a/COMPASS activity at the promoters lacking H3K4me3 enrichment in MEFs, as for hepatocyte-expressed genes *Mat1a*, *Alb*, *Pck1*, *Igfbp1*, *G6pc*, and *Ascl1* (Fig. 8b and Extended Data Fig. 10b). Remarkably, dCas-MINI-Vps15 targeting induced H3K4me3 enrichment at the TSS of *Alb* and *Mat1a* (Fig. 8d). This H3K4me3 methylation induced by dCas-MINI-Vps15 targeting was not accompanied by changes in RNAPII-S5p recruitment at TSS regions (Extended Data Fig. 10d). However, on *Mat2a*, dCas-MINI-Vps15 targeting was sufficient to induce RNAPII-S5p recruitment, and it was abolished by Vps34 lipid kinase inhibition with Vps34-IN1 (Fig. 8e). Then, using dCas-MINI-Vps34, we observed locus selectivity with Vps34 targeting induced H3K4me3 at *Mat2a* but not at *Mat1a* or *Alb* (Extended Data Fig. 10e). Notably, the kinase-dead Vps34-K771A still promoted RNAPII-S5p at *Mat1a* and *Mat2a* (Extended Data Fig. 10e), indicating that RNAPII engagement, in some contexts, could be uncoupled from Vps34 catalytic output. This finding was consistent with differential effect on productive transcription elongation such as increased RNAPII-S2p signal within the gene body in cells transiently overexpressing Vps34-K771A compared with WT Vps34 (Extended Data Fig. 10f). The differential effect of PI3K-3 targeting on H3K4me3 and RNAPII enrichment at hepatocyte-specific genes was not accompanied with their transcript induction (undetected CTs), pointing to requirement for additional co-activators, as well as chromatin

Fig. 7 | PI3K-3 co-activates Setd1a/COMPASS. a, Luciferase assay in HEK293T cells co-transfected with the *Mat1a*-luciferase reporter, p300 or CBP, with or without Vps15. Relative luminescence shown as fold induction compared to cells transfected with *Mat1a*-Luc + empty vector (EV) (grey background). Data are mean ± s.e.m., $^{\#}P < 0.05$ ($n = 7$ independent biological repeats for EV + EV and EV + Vps15, $n = 6$ independent biological repeats for EV + p300, Vps15 + p300, $n = 3$ independent biological repeats for EV+ CBP and Vps15 + CBP), two-way ANOVA with Benjamini–Hochberg correction. **b**, Luciferase assay in HEK293T cells co-transfected with the *Mat1a*-luciferase reporter and p300, Vps15, Vps34 or truncated mutants of Vps34. Relative luminescence shown as fold induction compared with cells transfected with *Mat1a*-luc + EV (grey background). Data are mean ± s.e.m., $^{\#}P < 0.05$ ($n = 5$ independent biological repeats), two-way ANOVA with Benjamini–Hochberg correction. **c**, Immunoblot analysis of immunoprecipitated Flag-tagged full length or truncated mutants of Vps34 in HEK293T cells, probed with respective antibodies ($n = 2$ independent biological repeats). **d**, Luciferase assay in Vps15$^{f/f}$ cells transduced with either adeno-GFP (WT) or adeno-CRE (Vps15KO) and, after 5 days, co-transfected with the *Mat1a*-luc reporter together with either EV or p300. Relative luminescence shown as fold induction compared with cells transfected with *Mat1a*-luc + EV in WT conditions (grey background). Data are mean ± s.e.m., $^{\#}P < 0.05$ ($n = 7$ independent biological repeats), two-way ANOVA with Benjamini–Hochberg correction. **e**, Luciferase assay in HEK293T cells co-transfected with the *Mat1a*-luciferase reporter, p300 with or without Vps15. Cells were treated with either DMSO, C646 (p300 acetyltransferase inhibitor) or OICR (Win-site WDR5 inhibitor). Relative luminescence shown as fold induction compared with cells transfected with *Mat1a*-luc + EV (grey background). Data are mean ± s.e.m., $^{\#}P < 0.05$ ($n = 7$ independent biological repeats), two-way ANOVA with Benjamini–Hochberg correction. **f**, ChIP-qPCR using antibodies against the indicated targets in HEK293T cells transfected with either WT Vps34 or Vps34-3xNLS. Data are mean fold change (FC) of Vps34-3xNLS input normalized enrichment against IgG versus Vps34 input normalized enrichment against IgG, ± s.e.m., $^{\#}P < 0.05$ ($n = 4$ independent biological repeats), Student's two-tailed t-test. **g**, Top: a schematic diagram of the impact of 3xFlag-3xNLS-Methionase expression on intracellular L-methionine. Bottom: immunofluorescence microscopy of HEK293T cells transfected with 3xFlag-3xNLS-Methionase for 24 h ($n = 2$ independent biological repeats). Scale bar, 10 µm. **h**, LC–MS metabolomics showing L-methionine levels in HEK293T cells which either transiently overexpressed 3xFlag-3xNLS-methionase or were deprived of methionine for 4 h. Data are mean ± s.e.m. $^{\#}P < 0.05$ ($n = 3$ independent biological repeats), one-way ANOVA with Benjamini–Hochberg correction. **i**, Top: immunoblot of protein extracts from HEK293T cells transfected with 3xFlag-3xNLS-methionase for 12 h and 24 h and treated with DMSO or Vps34-IN1. Bottom: densitometric analyses of respective immunoblots with indicated antibodies. Data are mean ± s.e.m. $^{\#}P < 0.05$ ($n = 3$ independent biological repeats), two-way ANOVA with Benjamini–Hochberg correction. **j**, LC–MS analyses presenting SAM:SAH ratio in HEK293T cells treated as in **i**. Data are mean ± s.e.m. $^{\#}P < 0.05$ ($n = 3$ independent biological repeats), one-way ANOVA with Benjamini–Hochberg correction. **k**, Luciferase assay in HEK293T cells co-transfected with the *Mat1a*-luciferase reporter, p300 and 3xFlag-3xNLS-methionase, treated with DMSO or Vps34-IN1. Relative luminescence shown as fold induction compared with cells transfected with *Mat1a*-luc + EV. Data are mean ± s.e.m., $^{\#}P < 0.05$ ($n = 6$ independent biological repeats), two-way ANOVA with Benjamini–Hochberg correction. **l**, Venn diagram showing DEGs (limma, $P < 0.05$, $\log_2$ FC >1) in HEK293T cells treated as in **i**. Gene set enrichment analysis of GO BP in uniquely enriched genes between DMSO (EV versus 3xNLS-M (3xFlag-3xNLS-methionase)) and Vps34-IN1 (EV versus 3xNLS-M) using the GseaVis package in R. P values for pathway analysis determined with Fisher's exact test. **m**, A schematic diagram showing the metabolic outcomes and involvement of PI3K-3 lipid kinase on H3K4me3 in methionase-expressing cells. Schematics in **g** and **m** created in BioRender; Henneman, N. https://biorender.com/gqhx29q (2026).

https://doi.org/10.1038/s41556-026-02030-7

remodellers and transcription factors[27–29]. Thus, next we asked if PI3K-3 could activate transcription factors in identified hepatocyte-specific gene loci outside of the repressed chromatin by employing the luciferase assay. To test it, we performed motif analysis of shared RNAPII-S5p and Vps15-bound peaks in MEFs and Vps15 binding sites in livers of fasted WT mice. These revealed an enrichment for general transcription factors, including Sp1, YY1, homeobox family transcription factors and members of the ETS family (Extended Data Fig. 10g). Putative

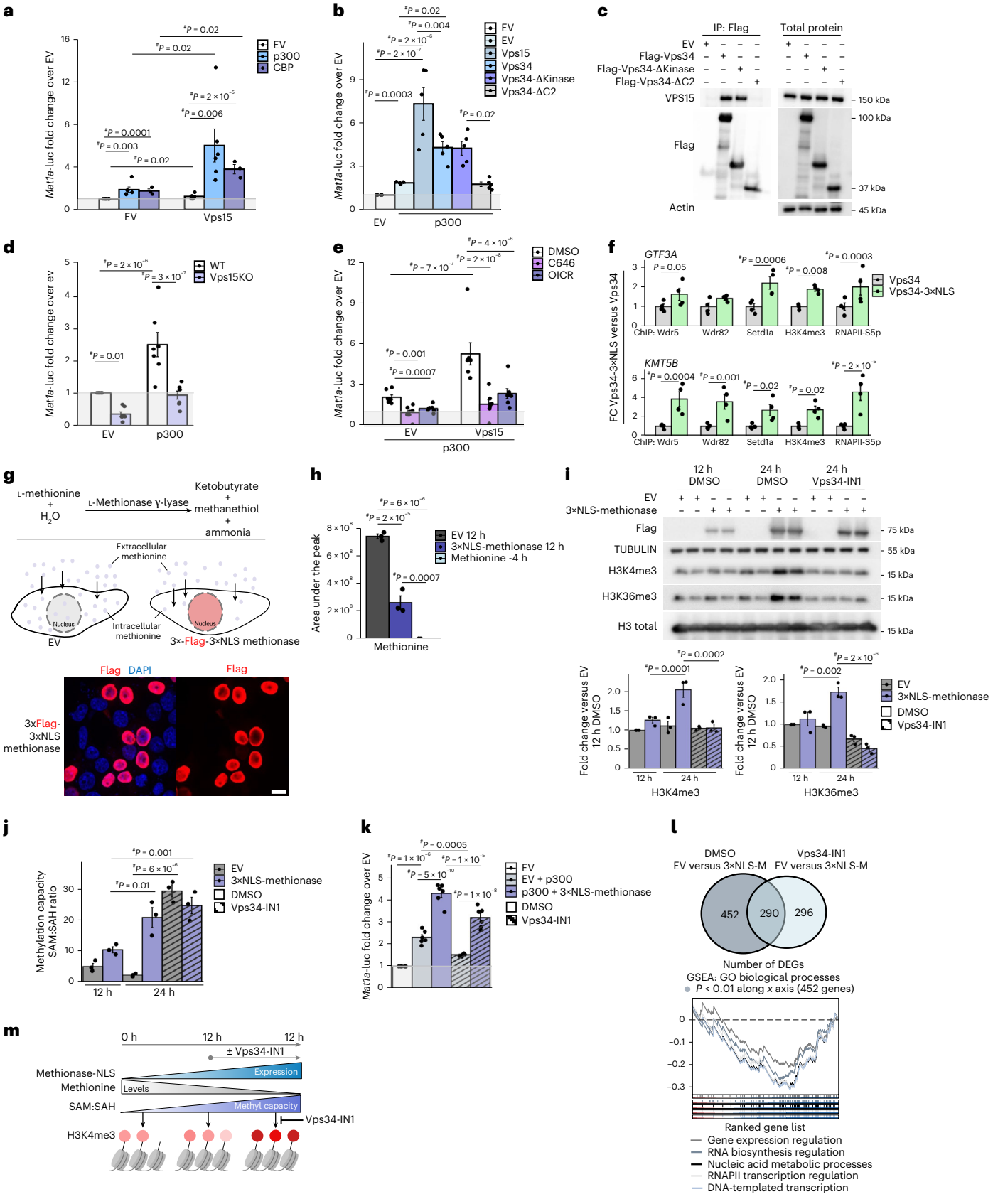

https://doi.org/10.1038/s41556-026-02030-7

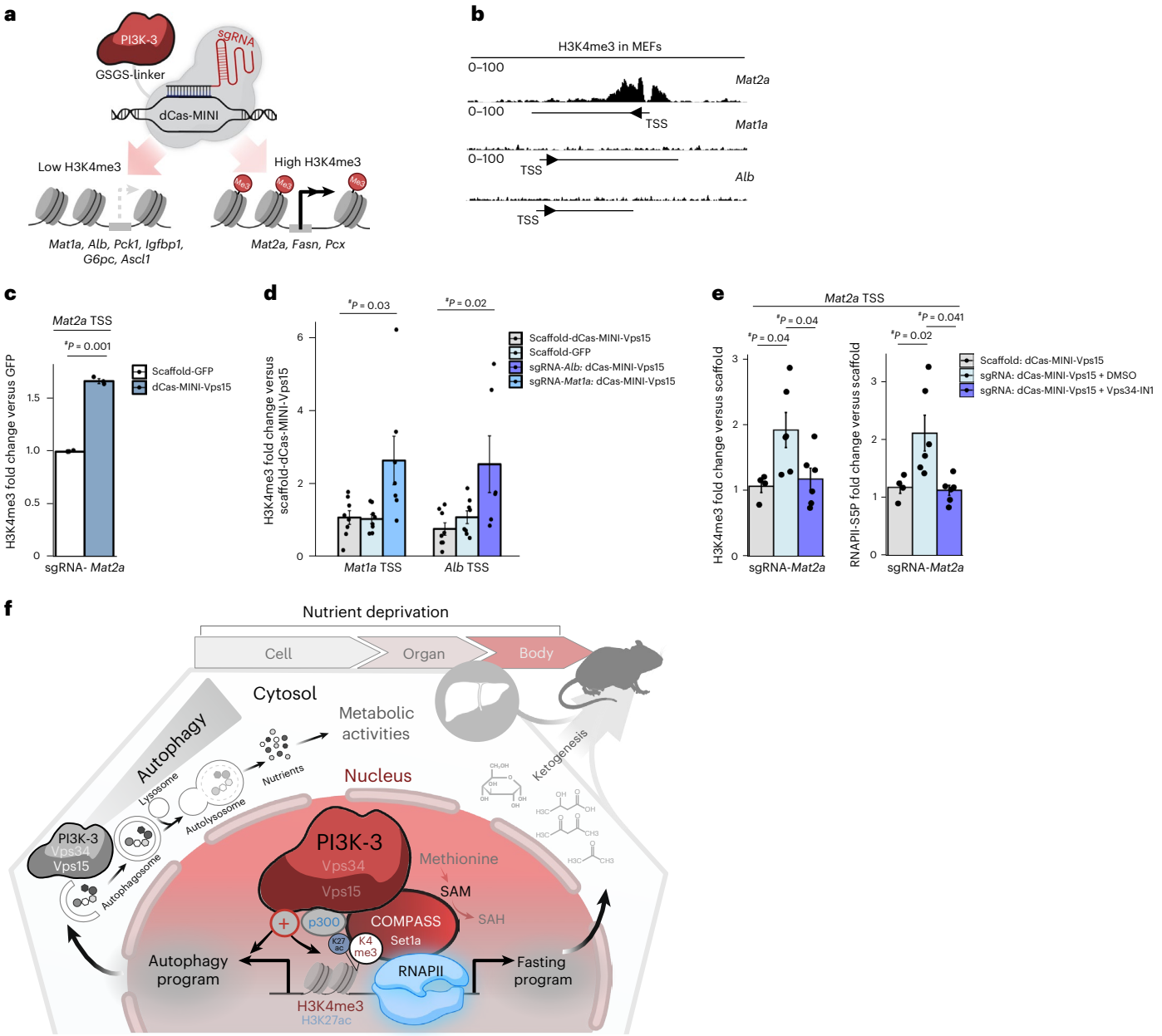

Fig. 8 | PI3K-3 acts on chromatin to promote H3K4me3. a, A schematic diagram showing the dCas-MINI fusion with PI3K-3 subunits (Vps15 or Vps34) targeted to transcriptionally active (high H3K4me3) or inactive loci (low H3K4me3) in MEFs. **b**, Gene tracks of H3K4me3 in MEFs on indicated genes. **c**, CUT&RUN–qPCR of H3K4me3 in MEFs transduced with lenti-sgRNA-*Mat2a* and either adeno-GFP or adeno-dCas-MINI-Vps15. Data are means ± s.e.m., fold change to adeno-GFP of relative H3K4me3 enrichment on the *Mat2a* TSS normalized to respective IgG control, $^{\#}P < 0.05$ ($n = 3$ independent biological repeats), two-tailed unpaired Student's *t*-test. **d**, CUT&RUN–qPCR of H3K4me3 in MEFs transduced with indicated lenti-sgRNA or lenti-scaffold with no sgRNA and adeno-dCas-MINI-Vps15 or adeno-GFP. Data are means ± s.e.m. fold change to scaffold-dCas-MINI-Vps15 normalized to respective IgG controls. $^{\#}P < 0.05$ ($n = 8$ independent biological repeats for scaffold-dCas-MINI-Vps15 and scaffold-GFP for *Mat1a*, $n = 7$ independent biological repeats for sgRNA-*Mat1a*-dCas-MINI-Vps15, $n = 8$ independent biological repeats for scaffold-dCas-MINI-Vps15 and scaffold-GFP for *Alb* and $n = 6$ independent biological repeats for sgRNA-*Alb*-dCas-MINI-Vps15), one-way ANOVA with Benjamini–Hochberg correction. **e**, CUT&RUN–qPCR of H3K4me3 or RNAPII-S5p in MEFs transduced with indicated lenti-sgRNA or lenti-empty scaffold and adeno-dCas-MINI-Vps15 for 24 h and treated with DMSO or Vps34-IN1. Data are means ± s.e.m. fold change to empty scaffold dCas-MINI-Vps15 and normalized to respective IgG controls. $^{\#}P < 0.05$ ($n = 4$ independent biological repeats for scaffold-dCas-MINI-Vps15, $n = 6$ independent biological repeats for sgRNA-dCas-MINI-Vps15), one-way ANOVA with Benjamini–Hochberg correction. **f**, A schematic diagram of PI3K-3 involvement in transcription to control autophagy and fasting programmes for the metabolic adaptation to nutrient deprivation. Schematics in **a** and **f** created in BioRender; Henneman, N. https://biorender.com/gqhx29q (2026).

binding sites for most of these transcription factors were also identified in the promoter of the hepatocyte-specific *Mat1a* gene. In line, overexpression of Sp1, YY1, Dlx2, En1 or c-Myc significantly enhanced *Mat1a*-luc activity and was comparable to Vps15 overexpression alone (Extended Data Fig. 10h). Notably, Vps15 further co-activated all of these transcription factors, with the strongest effects observed for c-Myc and Sp1 (Extended Data Fig. 10h). Altogether, these findings suggest that PI3K-3 engages as a co-activator of Setd1a/COMPASS for targeted H3K4me3 deposition to promote RNAPII-driven transcription in response to nutrient stress (Fig. 8f).

Discussion

PI3K-3 links nutrient sensing to autophagy and endocytosis via its distinct cytosolic complexes[30–32], yet its nuclear localization across yeast, plants and animal cells also suggests a conserved role in transcriptional regulation[4–6]. We find that nuclear PI3K-3 co-activates Setd1a/COMPASS and p300/CBP, driving H3K4me3 deposition and RNAPII-mediated transcription on selective gene loci, opening to future mechanistic work. PI3K-3 might engage with RNAPII at least on three levels. For example, widespread proximal-promoter pausing of RNAPII across the genome has been shown in various cell types and cell states for prompt and timed transcription initiation of specific genes[33–35]. Moreover, the recruitment of specific transcription factors or epigenetic reader/writer landscape, determines whether H3K4me3 influences RNAPII promoter-proximal pause release and subsequent transcription[27,28,36]. Furthermore, as cytosolic PI3K-3 lipid kinase responds to changes in amino acid and glucose levels[37], a nutrient-sensitive nuclear PI3P pool could be also produced by PI3K-3. Supporting this, Vps15 was pulled down in complexes of WDR5, CDK9, NOLC1, and PAF1, highlighting potentially wider links of PI3K-3 to transcriptional control[38]. Our proteomic analyses also show that transcriptional/chromatin-associated interactors of PI3K-3 are mostly shared across fasting-fed states in liver. Thus, our findings support a model in which fasting targets pre-existing PI3K-3 interaction networks to responsive loci. Importantly, the upstream mechanism that recruits PI3K-3 to specific chromatin loci (for example, posttranslational modifications, binding with transcription factors and chromatin features) remains a key future direction. However, given that we identified the nuclear PI3K-3 interactome with its core subunit, Vps15, we cannot rule out the existence of distinct PI3K-3 chromatin subcomplexes responsive to nuclear metabolic states. This would be analogous to PI3K-3 subcomplexes in the cytosol specialized for autophagy or endocytosis[3]. Future proximity labelling proteomes of chromatin-bound PI3K-3 would facilitate their identification.

Prior studies established that methionine/SAM availability allocates methyl donors across competing methylation 'sinks' and can impact autophagy through methylation-dependent programmes[25,39]. We did not observe a histone 'methyl-sink' phenotype in liver mutants of PI3K-3 or after acute depletion of PI3K-3 in cells unlike in cells with transient increase of SAM. Using nucleus-targeted methionase, we uncoupled intracellular methionine levels from extracellular supply, producing a transient SAM increase with elevated H3K4me3/H3K36me3, acting as an inducible histone 'methyl-sink' state that required PI3K-3 lipid kinase activity. As such, our findings point to lipid-kinase-dependent and independent transcriptional roles of PI3K-3 on chromatin for H3K4me3 deposition and RNAPII engagement. Inadvertently, we also discovered that PI3K-3 is required for maintaining nuclear SAM. These open to the questions on how nuclear SAM is maintained, sensed and integrated to instruct transcriptional complexes engaged with nuclear PI3K-3. Moreover, in light of Mat1a as a fasting-enriched Vps15 interactor, it will be interesting to address the role of PI3K-3 and PI3P in compartmentalization of transcriptional factories or condensates sensitive to metabolites such as methionine and SAM[40], especially.

Finally, we find PI3K-3-deficient cells are inefficient in inducing autophagy-related genes under starvation, and PI3K-3 liver mutants show impaired fasting metabolic responses[8,41,42]. Accumulation of transcriptional repressors in autophagy-deficient cells may partially underly this phenotype[8,9], yet selective loss of H3K4me3 and RNAPII points to a direct chromatin role for PI3K-3. Recent work in chronic dietary restriction model in *Caenorhabditis elegans* connected SET-2/COMPASS and vps34, via macroautophagy providing an interesting hint to their functional crosstalk[43]. Moreover, several epigenetic factors were reported to regulate the autophagy gene programme under different stresses in cells, while less is known about its epigenetic control in vivo[44–49]. In fasted liver, the transcriptional activation of autophagy involves the removal of inhibitory H3K27me3 by histone demethylase JMJD3/KDM6B[50]. In feeding, autophagy repression is associated with demethylation of activatory H3K4me2/3 and deacetylation of H3K9/14ac, as well as deposition of repressive H3K9me2[51]. Thus, functional interactions of nuclear PI3K-3 with epigenetic modifiers may extend beyond Setd1a/COMPASS and p300/CBP, identified here. Overall, our work provides broader principles by which nutrient-sensing signals might be integrated within the nucleus to maintain epigenetic programmes under metabolic stress. Fasting gains mainstream popularity for its health benefits[52,53], while transcriptional deregulation emerges as a hallmark of aging[1,11]. Understanding the molecular mechanisms of how nuclear PI3K-3 coordinates transcriptional and epigenetic machinery for metabolic rewiring to nutrient stress represents an exciting research direction.

Online content

Any methods, additional references, Nature Portfolio reporting summaries, source data, extended data, supplementary information, acknowledgements, peer review information; details of author contributions and competing interests; and statements of data and code availability are available at https://doi.org/10.1038/s41556-026-02030-7.

References

1. Debès, C. et al. Ageing-associated changes in transcriptional elongation influence longevity. *Nature* **616**, 814–821 (2023).
2. Evans, R. M. & Mangelsdorf, D. J. Nuclear receptors, RXR, and the Big Bang. *Cell* **157**, 255–266 (2014).
3. Backer, J. M. The intricate regulation and complex functions of the class III phosphoinositide 3-kinase Vps34. *The Biochemical Journal* **473**, 2251–2271 (2016).
4. Bunney, T. D. et al. Association of phosphatidylinositol 3-kinase with nuclear transcription sites in higher plants. *The Plant Cell* **12**, 1679–1688 (2000).
5. Gaur, N. A. et al. Vps factors are required for efficient transcription elongation in budding yeast. *Genetics* **193**, 829–851 (2013).
6. Alkhoury, C. et al. Class 3 PI3K coactivates the circadian clock to promote rhythmic de novo purine synthesis. *Nat. Cell Biol.* **25**, 975–988 (2023).
7. Koike, N. et al. Transcriptional architecture and chromatin landscape of the core circadian clock in mammals. *Science* **338**, 349–354 (2012).
8. Iershov, A. et al. The class 3 PI3K coordinates autophagy and mitochondrial lipid catabolism by controlling nuclear receptor PPARα. *Nat. Commun.* **10**, 1566 (2019).
9. Saito, T. et al. Autophagy regulates lipid metabolism through selective turnover of NCoR1. *Nat. Commun.* **10**, 1567 (2019).
10. Hsin, J. P. & Manley, J. L. The RNA polymerase II CTD coordinates transcription and RNA processing. *Genes Dev.* **26**, 2119–2137 (2012).
11. Gyenis, A. et al. Genome-wide RNA polymerase stalling shapes the transcriptome during aging. *Nat. Genet.* **55**, 268–279 (2023).
12. Rosonina, E. & Blencowe, B. J. Analysis of the requirement for RNA polymerase II CTD heptapeptide repeats in pre-mRNA splicing and 3′-end cleavage. *RNA* **10**, 581–589 (2004).
13. Nemazanyy, I. et al. Defects of Vps15 in skeletal muscles lead to autophagic vacuolar myopathy and lysosomal disease. *EMBO Mol. Med.* **5**, 870–890 (2013).
14. Wang, H. et al. H3K4me3 regulates RNA polymerase II promoter-proximal pause-release. *Nature* **615**, 339–348 (2023).
15. Krogan, N. J. et al. The Paf1 complex is required for histone H3 methylation by COMPASS and Dot1p: linking transcriptional elongation to histone methylation. *Mol. Cell* **11**, 721–729 (2003).
16. Bae, H. J. et al. The Set1 N-terminal domain and Swd2 interact with RNA polymerase II CTD to recruit COMPASS. *Nat. Commun.* **11**, 2181 (2020).
17. Mentch, S. J. et al. Histone methylation dynamics and gene regulation occur through the sensing of one-carbon metabolism. *Cell Metab.* **22**, 861–873 (2015).

18. Horiuchi, K. Y. et al. Assay development for histone methyltransferases. *Assay Drug Dev. Technol.* **11**, 227–236 (2013).
19. Shinsky, S. A., Monteith, K. E., Viggiano, S. & Cosgrove, M. S. Biochemical reconstitution and phylogenetic comparison of human SET1 family core complexes involved in histone methylation. *J. Biol. Chem.* **290**, 6361–6375 (2015).
20. Zhao, W. et al. Investigating crosstalk between H3K27 acetylation and H3K4 trimethylation in CRISPR/dCas-based epigenome editing and gene activation. *Sci. Rep.* **11**, 15912 (2021).
21. Tomasi, M. L., Li, T. W., Li, M., Mato, J. M. & Lu, S. C. Inhibition of human methionine adenosyltransferase 1 A transcription by coding region methylation. *J. Cell. Physiol.* **227**, 1583–1591 (2012).
22. Yang, H. et al. Role of promoter methylation in increased methionine adenosyltransferase 2A expression in human liver cancer. *Am. J. Physiol. Gastrointest. Liver Physiol.* **280**, G184–G190 (2001).
23. Capelo-Diz, A. et al. Hepatic levels of S-adenosylmethionine regulate the adaptive response to fasting. *Cell Metab.* **35**, 1373–1389 e1378 (2023).
24. Ye, C. & Tu, B. P. Sink into the epigenome: histones as repositories that influence cellular metabolism. *Trends Endocrinol. Metab.* **29**, 626–637 (2018).
25. Ye, C., Sutter, B. M., Wang, Y., Kuang, Z. & Tu, B. P. A metabolic function for phospholipid and histone methylation. *Mol. Cell* **66**, 180–193 e188 (2017).
26. Xu, X. et al. Engineered miniature CRISPR–Cas system for mammalian genome regulation and editing. *Mol. Cell* **81**, 4333–4345.e4334 (2021).
27. Policarpi, C., Munafò, M., Tsagkris, S., Carlini, V. & Hackett, J. A. Systematic epigenome editing captures the context-dependent instructive function of chromatin modifications. *Nat. Genet.* **56**, 1168–1180 (2024).
28. Isbel, L., Grand, R. S. & Schübeler, D. Generating specificity in genome regulation through transcription factor sensitivity to chromatin. *Nat. Rev. Genet.* **23**, 728–740 (2022).
29. Cano-Rodriguez, D. et al. Writing of H3K4Me3 overcomes epigenetic silencing in a sustained but context-dependent manner. *Nat. Commun.* **7**, 12284 (2016).
30. Itakura, E., Kishi, C., Inoue, K. & Mizushima, N. Beclin 1 forms two distinct phosphatidylinositol 3-kinase complexes with mammalian Atg14 and UVRAG. *Mol. Biol. Cell* **19**, 5360–5372 (2008).
31. Matsunaga, K. et al. Two Beclin 1-binding proteins, Atg14L and Rubicon, reciprocally regulate autophagy at different stages. *Nat. Cell Biol.* **11**, 385–396 (2009).
32. Liang, C. et al. Beclin1-binding UVRAG targets the class C Vps complex to coordinate autophagosome maturation and endocytic trafficking. *Nat. Cell Biol.* **10**, 776–787 (2008).
33. Muse, G. W. et al. RNA polymerase is poised for activation across the genome. *Nat. Genet.* **39**, 1507–1511 (2007).
34. Zeitlinger, J. et al. RNA polymerase stalling at developmental control genes in the *Drosophila melanogaster* embryo. *Nat. Genet.* **39**, 1512–1516 (2007).
35. Lysakovskaia, K., Devadas, A., Schwalb, B., Lidschreiber, M. & Cramer, P. Promoter-proximal RNA polymerase II termination regulates transcription during human cell type transition. *Nat. Struct. Mol. Biol.* **32**, 995–1005 (2025).
36. Douillet, D. et al. Uncoupling histone H3K4 trimethylation from developmental gene expression via an equilibrium of COMPASS, Polycomb and DNA methylation. *Nat. Genet.* **52**, 615–625 (2020).
37. Kim, J. et al. Differential regulation of distinct Vps34 complexes by AMPK in nutrient stress and autophagy. *Cell* **152**, 290–303 (2013).
38. Dawson, M. A. et al. Inhibition of BET recruitment to chromatin as an effective treatment for MLL-fusion leukaemia. *Nature* **478**, 529–533 (2011).
39. Ye, C. et al. Demethylation of the protein phosphatase PP2A promotes demethylation of histones to enable their function as a methyl group sink. *Mol. Cell* **73**, 1115–1126.e1116 (2019).
40. Rippe, K. & Papantonis, A. RNA polymerase II transcription compartments—from factories to condensates. *Nat. Rev. Genet.* **26**, 775–788 https://doi.org/10.1038/s41576-025-00859-6 (2025).
41. Nemazanyy, I. et al. Class III PI3K regulates organismal glucose homeostasis by providing negative feedback on hepatic insulin signalling. *Nat. Commun.* **6**, 8283 (2015).
42. Bilanges, B. et al. Vps34 PI 3-kinase inactivation enhances insulin sensitivity through reprogramming of mitochondrial metabolism. *Nat. Commun.* **8**, 1804 (2017).
43. Lim, C. Y. et al. SAMS-1 coordinates HLH-30/TFEB and PHA-4/FOXA activities through histone methylation to mediate dietary restriction-induced autophagy and longevity. *Autophagy* **19**, 224–240 (2023).
44. Füllgrabe, J. et al. The histone H4 lysine 16 acetyltransferase hMOF regulates the outcome of autophagy. *Nature* **500**, 468–471 (2013).
45. Chen, S. et al. Histone H2B monoubiquitination is a critical epigenetic switch for the regulation of autophagy. *Nucleic Acids Res.* **45**, 1144–1158 (2017).
46. Shin, H. J. et al. AMPK-SKP2-CARM1 signalling cascade in transcriptional regulation of autophagy. *Nature* **534**, 553–557 (2016).
47. Artal-Martinez de Narvajas, A. et al. Epigenetic regulation of autophagy by the methyltransferase G9a. *Mol. Cell. Biol.* **33**, 3983–3993 (2013).
48. Wei, F. Z. et al. Epigenetic regulation of autophagy by the methyltransferase EZH2 through an MTOR-dependent pathway. *Autophagy* **11**, 2309–2322 (2015).
49. Puri, D., Kelkar, A., Gaurishankar, B. & Subramanyam, D. Balance between autophagy and cell death is maintained by Polycomb-mediated regulation during stem cell differentiation. *FEBS J.* **290**, 1625–1644 (2023).
50. Byun, S. et al. Fasting-induced FGF21 signaling activates hepatic autophagy and lipid degradation via JMJD3 histone demethylase. *Nat. Commun.* **11**, 807 (2020).
51. Byun, S. et al. A postprandial FGF19-SHP-LSD1 regulatory axis mediates epigenetic repression of hepatic autophagy. *EMBO J.* **36**, 1755–1769 (2017).
52. Longo, V. D., Di Tano, M., Mattson, M. P. & Guidi, N. Intermittent and periodic fasting, longevity and disease. *Nat Aging* **1**, 47–59 (2021).
53. Aon, M. A. et al. Untangling determinants of enhanced health and lifespan through a multi-omics approach in mice. *Cell Metab.* **32**, 100–116.e104 (2020).

Methods

Reagents

The following primary antibodies were used: Vps15 (1:1,000, Abnova, H00030849-M02), Vps34 (1:1,000, Cell Signaling, 4263), Vps15 (1:1,000, GeneTex, GTX108953), Lamin A/C (1:1,000, Cell Signaling, 2032), Histone H3 (1:1,000 Cell Signaling 4499), H3K4me3 (1:1,000, Cell Signaling 9751), H3K36me3 (1:1,000, Cell Signaling, 4909), Set1a (1:1,000, Cell Signaling 61702), Wdr82 (1:1,000, Cell Signaling 99715), Wdr5 (1:1,000, Cell Signaling 13105), Flag (1:1,000, Sigma, F1804), RNAPII (1:1,000, Active Motif, 39097), RNAPII-S5p (1:1,000, Chromotek, 3E8-1) and MED17 (1:1,000, Cell Signaling, 64733). Plasmids expressing Vps15-Flag and Vps34-Flag used for subcloning of split-Luc assay constructs were purchased from MRC PPU Reagents and Services. Methionase-3×Flag-3×NLS, Vps34-Flag domain mutants, Vps15-3×NLS and Vps34-3×NLS were produced by VectorBuilder. The dCas-MINI-Vps15, Vps34 and Vps34K771A constructs were based on the dCas-MINI-V4-VPR construct (Addgene#:176269) with VPR replaced by PI3K-3 subunits and generated by VectorBuilder. Plasmids expressing RNAPII-CTD-Flag domain mutants were used from a previous report (Addgene#: 35175, 35176, 35178, 35179)[12]. Wdr5-Flag plasmid was used in a previous report (Addgene#:15552). RbBP5-Flag was used in a previous report (Addgene#:15550). Med26-Flag plasmid was used in a previous report (Addgene#:15367). The *Mat1a*- and *Mat2a*- promoter luciferase reporter constructs were kind gift from Dr Shelly Lu[21,22].

Animals

Inducible Vps15 hepatocyte-specific knockout (KO) mice were generated by crossing $Vps15^{f/f}$ mice with mice expressing the Cre recombinase under the transthyretin promoter[54]. To induce Vps15 deletion in hepatocytes, 12-week-old male mice were injected intraperitoneally with tamoxifen (1.5 mg per mouse) for five consecutive days. All animals used were fed a standard chow diet (Teklad Global, 18% protein, irradiated) ad libitum and housed in a 12–12 hour (8:00–20:00) lights ON/OFF cycle in ambient temperature (21–22 °C) and humidity of 50–60%. All feeding/fasting experiments were performed at ZT14 (22:00), 14 days following the first injection of tamoxifen. Livers were removed and flash frozen in liquid nitrogen. All experiments were approved Université Paris Cité ethical committee (authorization numbers: APAFIS#32312).

Cell culture

MEF cells were immortalized by passaging[55]. $Vps15^{f/f}$ MEFs were obtained from a pool of embryos from two different females were passaged every 3 days before spontaneous transformation[13]. All cultures were tested bi-weekly and validated as mycoplasma-free. To obtain $Vps15^{-/-}$ MEFs, cells were grown in High-glucose DMEM (Gibco) containing 100 U ml^{-1} of penicillin, 100 mg ml^{-1} streptomycin, 10% fetal bovine serum (FBS) and were transduced with adenoviruses expressing CRE–GFP or GFP (control) with a multiplicity of infection of 500. Methionine starvation and stimulation treatments were performed using High-glucose DMEM without methionine (ThermoFisher, 21013024), supplemented with cysteine and glutamine, for methionine starvation, and for methionine stimulation conditions, methionine was added back at 30 mg l^{-1}. Human embryonic kidney 293 (HEK293T) cells were purchased from the ATCC (CRL-3216) and cultured in high-glucose DMEM supplemented with 100 U ml^{-1} penicillin, 100 mg ml^{-1} streptomycin and 10% FBS. Vps34-IN1 (MedChemExpress) was dissolved in DMSO and cells treated between 12 and 24 h, depending on the experiment at a final concentration of 5 µM.

Biochemical fractionation

The cytosolic fractions of cells (1×10^6) were extracted with 800 µl of ice-cold hypotonic buffer (10 mM HEPES pH 7.9, 0.5 mM DTT, 1× protease inhibitors (Roche), 1× PhosphoStop Inhibitors (Roche)). Cells were vortexed for 10 s every 10 min for 30 min and kept on ice. Following the addition of 8 µl 10% NP-40, samples were vortexed and allowed to rest for 2 min before being vortexed again. Samples were then centrifuged at 800*g* at 4 °C for 2 min, and the supernatant was collected as the cytosolic fraction. Nuclear pellets were then washed with hypotonic buffer, then with 14% NP-40 in hypotonic buffer and washed again with hypotonic buffer alone. The nuclear soluble fraction was then extracted using 1% Triton buffer (1% Triton X-100, 40 mM HEPES, 120 mM NaCl, 1 mM EDTA, 50 mM NaF) with protease and phosphatase inhibitors. The nuclear fraction was vortexed for 10 s, and samples were then centrifuged at 15,000*g* at 4 °C for 5 min. The supernatant was collected as the nuclear fraction. The remaining pellet was washed with 1% Triton buffer, and the nuclear insoluble fraction was resuspended in 100 µl of 0.2 N HCl following incubation for 20 min. The HCl was then neutralized with 5 M NaOH, and samples were centrifuged at 15,000*g* for 1 min; the supernatant represents the nuclear insoluble/chromatin fraction. For nuclear fractionation of liver tissue, 50 mg of powdered liver tissue was first homogenized in hypotonic buffer (10 mM HEPES pH 7.9, 0.5 mM DTT, 1× protease inhibitors (Roche), 1× PhosphoStop Inhibitors (Roche)) using a drill homogenizer for 15 strokes at 500 rpm. The samples were incubated 10 min on ice before proceeding with additional 15 strokes at 500 rpm. Following tissue homogenization, the protocol for liver fractionation then follows the same in cells starting at 30 min of vortexing samples for 10 sec once every 10 min.

Protein extraction, immunoblotting and immunoprecipitation

To prepare total protein extracts for immunoblot analysis, cells were washed twice with cold phosphate-buffered saline (PBS), scraped from the dishes in lysis buffer containing 20 mM Tris–HCl (pH 8.0), 5% glycerol, 128 mM NaCl, 2.7 mM KCl, 1% NP-40, 20 mM NaF, 5 mM EDTA, 1× protease inhibitors (Roche), 1× PhosphoStop Inhibitors (Roche) and vortexed for 10 s. A total of 30 mg of powdered liver was extracted with the sample lysis buffer. Lysates were spun at 15,000*g* for 10 min at 4 °C. Protein concentration was measured by Bradford assay (BioRad). For immunoprecipitation, nuclei were extracted in 1% Triton buffer (1% Triton X-100, 40 mM HEPES, 120 mM NaCl, 1 mM EDTA, 50 mM NaF) sonicated for five rounds of 10 s ON followed by 30 s OFF using the Pico Bioruptor (Diagenode, B01080010). Immunoprecipitation was set with 1 mg of nuclear protein extract which was incubated with 2 µg of primary antibody overnight at 4 °C on a rotating wheel. Magnetic protein-A (Dynabeads, ThermoFisher, 10002D) beads were used to pull down immune complexes for 2 h, followed by four washes with 1% Triton buffer. Protein complexes on beads were boiled in 1× SDS-sample buffer for 10 min, and protein extracts or immunoprecipitate eluates were resolved by SDS–PAGE before transfer to a PVDF membrane followed by incubation with primary antibodies and subsequent incubation with HRP-linked secondary antibodies. Immobilon Western Chemiluminescent HRP Substrate (Millipore) was used for detection. Images were acquired on ChemiDocTM Imager (BioRad).

RT–qPCR

Total RNA from liver was extracted with a RNeasy lipid tissue kit (Qiagen) and from cells using the RNeasy mini kit (Qiagen). Single-strand complementary DNA (cDNA) was synthesized from 1 µg of total RNA using 125 ng random hexamer primers and SuperScript II (Life Technologies). Reverse-transcriptase quantitative PCR (RT–qPCR) was performed on a QuantStudio 1 (Thermo Fisher) using iTaq Universal SYBR Green Supermix (BioRad). Relative amount of mRNA was determined using the $2^{-\Delta\Delta CT}$ method. Primer sequences are listed in the Supplementary Information.

Plasmid construction for the split luciferase assay

Expression vectors for Vps15-NlucC, NlucC-Vps15, Vps34-NlucC, WDR5-NlucN, NlucN-WDR5, NlucN-RbBP5, RbBp5-NlucN, NlucN-RNAPII and H2B-NlucN were generated by PCR amplification and enzymatic digestion followed by ligation of the DNA fragments

into pcDNA3 expression vector (Invitrogen). DNA polymerase, DNA restriction enzymes and DNA modification enzymes were obtained from Takara Bio. Plasmid encoding Vps15 was developed as described previously[6]. cDNAs encoding RbBP5 (pcDNA3 Flag-RbBP5) and WDR5 (pcDNA3-Flag-WDR5) were a gift from Kai Ge (Addgene plasmid #15550, #15552)[56] The cDNA of split NanoLuc fragments (NlucN and NlucC)[57] were synthesized using oligonucleotides by PCR with PrimeSTAR HS DNA polymerase (Takara Bio). The sequences of the inserted region were confirmed using DNA sequencing analysis (Eurofins Genomics). Expression vectors were purified using PureLink HiPure Plasmid Midiprep Kit (Life Technologies).

Luminescence measurement

HEK293T cells were cultured for 24–28 h on a 96-well solid white microplate at a density of 2×10^4 cells per well with 100 µl per well of DMEM supplemented with 10% FBS and 100 U ml^{-1} penicillin, 100 mg ml^{-1} streptomycin. Plasmids were introduced into cells using TransIT LT1 reagent (Takara Bio) at a total concentration of 10 ng per well at a 1:1 ratio of split-luciferase fragments. A total of 24 h later, the medium was replaced with 100 µl per well of Hank's balanced salt solution (HBSS, Gibco) supplemented with 10% FBS, 20 mM HEPES and furimazine at a 1:2,500 dilution (Nano-Glo Luciferase Assay System; Promega). The bioluminescent signal was recorded for 45 min at 0.5 s per well exposure time using a multimode plate reader (TriStar LB941; Berthold). The value of bioluminescent signal intensity for each split-luciferase fragment pair was calculated using an integral of the luminescence signal over the measurement period. The signal intensity was further normalized by the signal intensity of the negative control (cells expressing only the NlucC fragment) and a $\log_{10}$ value presented.

For live imaging of bioluminescence, a custom-made imaging system based on an inverted fluorescence microscope (IX-81; Olympus) was used. All images were obtained using a cooled EM-CCD camera (ImagEM; Hamamatsu Photonics) with a 20× objective lens (UPLSAPO20XO; Olympus). A metal-halide light source (KTX-60MT; Kenko Tokina) was used for fluorescence imaging. The total imaging system was located in a dark box, of which the temperature was set at 22 °C. For imaging, HEK293T cells were cultured for 24–28 h on a µ-Slide 8 Well (Ibidi) at 3×10^4 cells per well density with 250 µl per well of DMEM supplemented with 10% FBS and 100 U ml^{-1} penicillin, 100 mg ml^{-1} streptomycin at 37 °C with 5% CO_2. The plasmids were transfected using TransIT LT1 reagent (Takara Bio) at 25 ng per well concentration. A total of 48 h post transfection, cells were incubated with Hoechst33342 (Invitrogen) for 20 min before imaging. Buffer solutions of cell samples were exchanged into HBSS supplemented with 10% FBS and 20 mM HEPES. After 10 min incubation of the cells on the stage of the bioluminescence microscope, furimazine was added at 1:1,000 dilution. A Metamorph software (Molecular Devices) was used to control all image acquisition.

Luciferase Assay

The luciferase assay was performed in HEK293T cells. The cells were plated in 24-well plates and PEI-transfected with a mix of either luciferase reporter constructs (*Mat1a* or *Mat2a*), control plasmid expressing β-galactosidase (0.05 µg), Vps15-Flag or Vps34-Flag constructs (0.15 µg), p300 or CBP (0.15 µg) or pcDNA3.1 (0.3 µg) as a control. After transfection (24–36 h), the cells were collected, 1× passive lysis buffer (Promega) used for extraction, and luciferase reporter activity was measured and normalized to β-galactosidase activity as previously reported[10]. p300/CBP acetyltransferase inhibitor, C646 (MedChemExpress) and WIN site-WDR5 inhibitor, OICR (MedChemExpress), were used at concentrations of 20 µM and 75 µM, respectively, for 12 h.

dCas-MINI and related constructs

The adenoviral vector construct expressing the fusion protein of dCas-MINI-Vps15 or dCas-MINI-Vps34 were generated by Vector Builder, according to a previous study[11]. Guide RNAs were designed using single-guide RNA (sgRNA) scaffold design 2 from the previous report; 24 bp, 225 bp and 259 bp from the *Mat2a* TSS; 428 bp, 709 bp, 752 bp, 819 bp and 990 bp from the *Mat1a* TSS; 370 bp, 371 bp and 398 bp from the *Pck1* TSS; 307 bp, 352 bp and 372 bp from the *Igfbp1* TSS; 117 bp, 129 bp and 140 bp from the *G6pc* TSS; 349 bp, 364 bp and 399 bp from the *Alb* TSS; 12 bp, 26 bp and 82 bp from the *Fasn* TSS; 117 bp, 174 bp and 224 bp from the *Ascl1* TSS; 46 bp, 127 bp and 358 bp from the *Pcx* TSS. MEF stable lines were generated by transfecting all three guide constructs, and cells were selected by puromycin. Stable lines expressing mixed sgRNA pool were transduced with dCas-MINI-Vps15, dCas-MINI-Vps34 or GFP (control) adenoviruses for 24 h before CUT&RUN for H3K4me3, RNAPII-S5p or RNAPII-S2p. Relative DNA enrichment was determined by quantitative PCR using the $2^{-\Delta\Delta CT}$.

Targeted metabolomics analysis

For targeted metabolomics analysis, cells or liver tissue were flash frozen in liquid nitrogen and analysed with liquid chromatography mass spectrometry as was previously described[58]. Metabolites were extracted with 50% methanol, 30% acetonitrile and 20% water with the extraction volume normalized to cell number or tissue weight. Samples were vortexed for 5 min at 4 °C and centrifuged at 16,000*g* for 15 min at 4 °C. Supernatants were collected and analysed by liquid chromatography followed by mass spectrometry using the SeQuant ZIC-pHilic column (Merck) for liquid-chromatography separation. Mobile phase A was 20-mM ammonium carbonate and 0.1% ammonia hydroxide in H_2O. Mobile phase B was acetonitrile. Flow rate was 100 ml min^{-1}, and the gradient was: 0 min, 80% phase B; 30 min, 20% phase B; 31 min, 80% phase B, and 34 min, 80% phase B. The mass spectrometer (QExactive Orbitrap, Thermo Fisher) was operated in polarity switching mode and metabolites were identified using TraceFinder Software (Thermo Fisher). For SAM detection in nuclear extracts, cells were extracted in 800 µl of ice-cold hypotonic buffer (10 mM HEPES pH 7.9, 0.5 mM DTT, 1× protease inhibitors (Roche), 1× PhosphoStop Inhibitors (Roche)). A total of 8 µl of 10% NP40 was added and extracts were vortexed for two rounds of 5 s, after which were washed two times with ice-cold hypotonic buffer. After the final wash, hypotonic buffer was aspirated and nuclear pellets were flash frozen in liquid nitrogen. Nuclear pellets were then processed like all other samples for metabolite extraction. For analysis, data were normalized using sum normalization with MetaboAnalyst 5.0. The pheatmap and ggplot packages in R, was used to generate the heat map and individual metabolite plots, respectively.

RNA sequencing analysis

Total RNA was extracted from liver tissue or cells and sequenced using the DNBSEQ-400 sequencer. Clean reads were obtained by SOAPnuke filtering using: -n 0.03 -l 20 -q 0.4 -A 0.28. FASTQ files were aligned to the mm10 mouse genome using HISAT2 and counts generated using featureCounts from the Subread R package. Read-count normalization and group comparisons generated by three independent statistical methods: DESeq2, LimmaVoom and edgeR. Flags were determined from counts which were normalized to mean read coverage. Normalized counts were considered background if <20 (flag is 0), and signal was determined if counts ≥20 (flag is 1). P50 lists were used for statistical analysis regrouping genes that showed at least flag of 1. Direct comparisons were made between treatment conditions of WT, Vps15iLKO, fed and fasted conditions to generated differentially expressed gene (DEGs) lists. Gene set enrichment analysis (GSEA) version 4.2.2 was performed between groups[59]. DOSE GSEA performed with DOSE package, in R[60]. Density plots were generated by plotting vst normalized counts of RNA against respective gene-peak-score (V5 column, MACS2 output), for indicated ChIP and CUT&RUN experiments.

ChIP

ChIP was performed in liver and cells as previously described[61,62], with the following antibodies: Vps15 (Abnova, H00030849-M02), RNAPII-S5p

(Abcam, ab5408), RNAPII-S5p (Cell Signaling, 13523), RNAPII-S2p (Cell Signaling, 13499) H3K4me3 (Cell Signaling, 9751), mouse-IgG (Santa Cruz Biotechnology, sc-2025) and rabbit-IgG (Cell Signaling, 3900). In brief, powdered liver tissue was fixed for 15 min at room temperature (RT) with 1% formaldehyde (Sigma), after which was quenched in 125 mM glycine. Tissue was centrifuged at 800*g* for 5 min at 4 °C and washed in ice cold PBS on a rotating wheel for 5 min. Tissue was centrifuged at 800*g* for 5 min at 4 °C after which they were resuspended in lysis buffer (5 mM HEPES pH 8.0, 85 mM KCl, 0.5% NP40). Pellets were then homogenized with a Dounce homogenizer. Tissue was centrifuged at 800*g* for 5 min at 4 °C after which they were resuspended in SDS lysis buffer (50 mM Tris–HCl pH 8.0, 10 mM EDTA pH 8.0, 1% SDS) and vortexed for three rounds of 10 s. Samples were then frozen in liquid nitrogen and allowed to thaw, before being sonicated using the Pico Bioruptor (Diagenode) to achieve 200–500-bp chromatin fragments. Antibodies were added to chromatin overnight at 4 °C on a spinning wheel, and protein-A Dynabeads (Thermo Fisher, 10001D) was added to chromatin for 3 h. Bead-immune-complexes were washed once with Low Salt RIPA (150 mM NaCl, 50 mM Tris–HCl pH 8.0, 1 mM EDTA pH 8.0, 1% Triton X-100, 0.1% SDS and 0.1% sodium deoxycholate (NaDOC)), once with High Salt RIPA buffer (500 mM NaCl, 50 mM Tris–HCl pH 8.0, 1 mM EDTA pH 8.0, 1% Triton X-100, 0.1% SDS and 0.1% NaDOC), once with liver-LiCl wash buffer (250 mM LiCl, 10 mM Tris–HCl pH 8.0, 1 mM EDTA, 0.5% NP-40 and 0.5% NaDOC) and twice with TE buffer (10 mM Tris–HCl pH 8.0 and 1 mM EDTA pH 8.0). Immune complexes were then eluted with elution buffer (10 mM Tris–HCl pH 8.0, 300 mM NaCl, 5 mM EDTA pH 8.0 and 0.5% SDS) and reverse crosslinked overnight at 65 °C on a heat block. Eluted DNA was treated with RNAse and Proteinase K, and DNA was purified with phenol chloroform: isoamyl alcohol phase lock extraction. For cells, they were fixed with 1% formaldehyde (Sigma) for 10 min at RT and quenched with 125 mM glycine. Cells were sonicated in cell lysis buffer (25 mM Tris–HCl pH 8.0, 2 mM EDTA, 150 mM NaCl, 1% Triton X-100, 0.3% SDS) to achieve chromatin fragments of 200–500 bp. Chromatin was then incubated with respective antibodies overnight at 4 °C on a spinning wheel, and protein-A Dynabeads (Thermo Fisher, 10001D) was added to chromatin for 3 h. Bead-immune-complexes were then washed once each with wash I (10 mM Tris–HCl pH 8.0, 150 mM NaCl, 0.1% NaDOC, 1% Triton X-100), wash II (10 mM Tris–HCl pH 8.0, 150 mM NaCl, 1% NaDOC, 1% NP40), wash III (10 mM Tris–HCl pH 8.0, 500 mM NaCl, 0.1% NaDOC, 0.5% Triton X-100), wash IV (20 mM Tris–HCl pH 8.0, 250 mM LiCl, 1 mM EDTA pH 8.0, 0.5% NaDOC, 0.5% NP40), wash V (20 mM Tris–HCl pH 8.0, 150 mM NaCl, 1 mM EDTA pH 8.0, 0.1% NP40) and twice with TE buffer (10 mM Tris–HCl pH 8.0 and 1 mM EDTA pH 8.0). Immune-complexes were then reverse crosslinked in elution buffer (100 mM NaCl, 100 mM $NaHCO_3$, 1% SDS) overnight at 65 °C on a heat block. Eluted DNA was treated with RNAse and Proteinase K, and DNA was purified with phenol chloroform: isoamyl alcohol phase lock extraction. Eluted DNA was used for sequencing.

CUT&RUN

CUT&RUN was performed as previously described[63,64] with the following antibodies: Vps15 (1:1,000, GeneTex, GTX108953) H3K4me3 (Cell Signaling, 9751), RNAPII-S5p (Cell Signaling, 13523), rabbit-IgG (Cell Signaling, 3900). In brief, cells were counted and plated to have equal cell numbers per condition/treatments. 12–16 h after, wash buffer (20 mM HEPES pH 7.5, 150 mM NaCl, 500uM Spermidine, 1× protease inhibitors (Roche), 1× PhosphoStop Inhibitors (Roche)) was added to cells and they were scraped into tubes and centrifuged at 800*g* for 1 min at RT. Cells were resuspended in wash buffer and fixed with 0.1% formaldehyde (Sigma) in D-PBS for 3 min at RT spinning end-on-end to assure mixing. Formaldehyde was quenched in 125 mM Glycine for 2 min at RT, and cells were collected by centrifugation for 1 min at 800*g*. The pellet was resuspended in Fixation Wash Buffer (20 mM HEPES pH 7.5, 150 mM NaCl, 500uM Spermidine, 1% Triton X-100, 0.05% SDS, 1× protease inhibitors (Roche), 1× PhosphoStop Inhibitors (Roche)). The pellet was centrifuged at 800*g* for 1 min at RT, and resuspended with Fixation wash buffer to serve as a washing step. Cells were distributed equally into tubes containing pre-washed Concavalin-A (Polysciences, 86057-3) beads and rotated on a spinning wheel for 10 min at RT. Supernatant was aspirated and respective antibodies were added for 1-h incubation on a spinning wheel at RT. Beads were then washed twice with Digitonin wash buffer (20 mM HEPES pH 7.5, 150 mM NaCl, 500 µM Spermidine, 1% Triton X-100, 0.05% SDS, 0.1% Digitonin (Sigma), 1× protease inhibitors (Roche), 1× PhosphoStop Inhibitors (Roche)) and then incubated for 10 min with pAG-MNase at RT. Beads were washed twice with Digitonin wash buffer and kept on ice for 5 min. Ca^{2+} was added to activate pAG-MNase enzymatic activity, for 30 min, after which the enzyme was quenched with stop buffer (170 mM NaCl, 10 mM EDTA pH 8.0, 2 mM EGTA, 0.01% Digitonin, 50 µg ml^{-1} RNAse, 25 µg ml^{-1} Glycogen). Beads were incubated at 37 °C for 15 min to elute DNA fragments. Following Proteinase K treatment, DNA fragments were purified with phenol chloroform: isoamyl alcohol phase lock extraction or purified by PCR Clean-up columns (Machery-Nagel, 740609.250). DNA quality was determined by quantitative PCR using the $2^{-\Delta\Delta CT}$ method before sequencing. Primer sequences listed in Supplementary Information. CUT&RUN on the plate (CROP)[63] was performed for CUT&RUN followed by IP and dCas-MINI experiments whereby cells were plated on 24-well plates.

ChIP and CUT&RUN library preparation and sequencing

Sample quality was determined using the Agilent Technologies 2100 Bioanalyzer. DNA fragments were then subjected to end-repair and 3′ adenylation. Adaptors were ligated to the 3′ ends of adenylated fragments. PCR products purified and enriched using the Agencourt AMPure XP-medium kit. Double stranded PCR products were heat denatured and circularized by the splint oligonucleotide sequence. Single-stranded circular DNA was formatted as the final library, which was then quantified using the Qubit ssDNA kit. DNA nanoballs were made from the library and loaded into a patterned nanoarray, and paired-end reads were generated by sequenced combinatorial Probe-Anchor Synthesis. Sequencing was performed with the DNBSEQ-400 sequencer (Beijing Genomics Institute).

ChIP and CUT&RUN sequencing data analysis

Reads were filtered using SOAPnuke to remove adaptor sequences and low-quality reads. Data filtering was performed with: SOAPnuke filter -l 5 -q 0.5 -n 0.1 -Q 2 -c 30. Clean reads were aligned to either human hg38 or mouse mm10 genomes using Bowtie2 version 2.4.4, after which SAMtools version 1.13 was used to index and sort binary alignment map (BAM) files[19,20]. Composition bias normalization was performed with the csaw package in R[21]. Composition bias normalization scaling factors were used to generate bigwigs. The plotHeatmap function in the deepTools2 suite was used to create profile plots and heatmaps of peaks ordered by read concentration[22]. Peak calling was performed for all samples using MACS2 version 2.2.7.1[23]. Differential peak binding analysis was performed with DiffBind 3.10.0, an R package[24] or the bdgdiff command in MACS2. Peaks were annotated with ChIPseeker, and pathway analysis/visualization was performed using clusterProfiler, R packages[25,26]. Gene tracks are visualized with IGV.

Statistics and reproducibility

Data are shown as means ± s.e.m. The *n*-numbers of distinct samples or biological replicates are presented in figure legends. Either two-tailed Student's *t*-test, one-way analysis of variance (ANOVA) or two-way ANOVA were used for statistical analysis corrected with Benjamini–Hochberg post-test. Results were considered significant in all experiments at $P < 0.05$. No statistical method was used to predetermine sample size. Sample sizes were chosen based on previous literature and what is common practice in the field. Data distribution was assumed to be normal, but this was not formally tested. No data were excluded from the analyses. The experiments were not randomized. In all treatments

in vitro and in vivo, the samples were number-coded and investigators were blinded during extract preparations for molecular analyses (for example transcript and protein expression, luciferase assays). Depending on the analysis, the groups were revealed either at the stage of sample quantifications and statistical analyses (for example qPCR, luciferase assay) or when it was essential for analysis (for example immunoblot of time series to include all conditions in the same gel panel, immunoprecipitation or ChIP to set-up control and experimental groups with antibodies). Statistics analysis and data visualization were performed in R (4.1.2) using the rstatix, emmeans and ggplot2 packages. All statistical tests, exact *P* values, *n* and number of biological replicates are listed in Figs 1–8 and Extended Data Figs. 1–10.

Reporting summary

Further information on research design is available in the Nature Portfolio Reporting Summary linked to this article.

Data availability

All data are available in the main text or the supplementary materials. Deep-sequencing (ChIP-seq, CUT&RUN-seq and RNA-seq) data that support the findings of this study are deposited in the Gene Expression Omnibus (GSE290680, GSE290681, GSE290682, GSE320350, GSE322778). All other data supporting the findings of this study are available from the corresponding author on reasonable request. Source data are provided with this paper.

References

54. Tannour-Louet, M., Porteu, A., Vaulont, S., Kahn, A. & Vasseur-Cognet, M. A tamoxifen-inducible chimeric Cre recombinase specifically effective in the fetal and adult mouse liver. *Hepatology* **35**, 1072–1081 (2002).
55. Todaro, G. J. & Green, H. Quantitative studies of the growth of mouse embryo cells in culture and their development into established lines. *J. Cell Biol.* **17**, 299–313 (1963).
56. Cho, Y. W. et al. PTIP associates with MLL3- and MLL4-containing histone H3 lysine 4 methyltransferase complex. *J. Biol. Chem.* **282**, 20395–20406 (2007).
57. Hattori, M. et al. Confocal bioluminescence imaging for living tissues with a caged substrate of luciferin. *Anal. Chem.* **88**, 6231–6238 (2016).
58. Mackay, G. M., Zheng, L., van den Broek, N. J. & Gottlieb, E. Analysis of cell metabolism using LC–MS and isotope tracers. *Methods Enzymol.* **561**, 171–196 (2015).
59. Subramanian, A. et al. Gene set enrichment analysis: a knowledge-based approach for interpreting genome-wide expression profiles. *Proc Natl Acad. Sci. USA* **102**, 15545–15550 (2005).
60. Yu, G., Wang, L.-G., Yan, G.-R. & He, Q.-Y. DOSE: an R/Bioconductor package for disease ontology semantic and enrichment analysis. *Bioinformatics* **31**, 608–609 (2014).
61. Koronowski, K. B. et al. Defining the independence of the liver circadian clock. *Cell* **177**, 1448–1462 e1414 (2019).
62. Lerner, J. et al. Human mutations affect the epigenetic/bookmarking function of HNF1B. *Nucleic Acids Res.* **44**, 8097–8111 (2016).
63. Miura, M. & Chen, H. CUT&RUN detects distinct DNA footprints of RNA polymerase II near the transcription start sites. *Chromosome Res.* **28**, 381–393 (2020).
64. Skene, P. J. & Henikoff, S. An efficient targeted nuclease strategy for high-resolution mapping of DNA binding sites. *eLife* **6**, e21856 (2017).

Acknowledgements

We thank all the members of the Panasyuk laboratory as well as the members of INSERM-U1151 for their support and insightful discussions. We thank M. Pontoglio, J.-S. Annicotte and J.-C. Weil for the critical feedback on the manuscript. We thank B. Lemesre, Y. Shibayama and A. Ficany for their technical help with cell culture. We thank M. Pontoglio, A. Bagattin, S. Garbay, and K. Shostak for technical help with the set-up of the ChIP method. We thank S. Berissi (SFR Small Animal Histology and Morphology Platform), S. Fabrega (SFR Viral Vector and Gene Transfer Platform) and A. Stella (ProteoToul) for technical support. We thank L. Fajas for the gift of plasmid vectors (β-Gal, p300, CBP); M. Vasseur-Cognet and A.-F. Burnol for TtrCre deleter line.

Author contributions

Conceptualization: N.F.H. and G.P. Methodology: N.F.H., I.N., T.O., D.L., R.M. and G.P. Investigation: N.F.H., G.K., Y.L., C.O.D., J.S., A.S., I.N., N.K., N.C., S.l.C., C.R., K.H. and G.P. Data curation: N.F.H., I.N., N.C. and CR. Visualization: N.F.H. and G.P. Funding acquisition: G.P. Supervision: T.O., R.M. and G.P. Writing—original draft: N.F.H. and G.P. Writing—review and editing: all authors.

Funding

Agence National de la Recherche (grant no. ANR-JCJC-NUTRISENSPIK-16-CE14-0029 to G.P.; grant no. ANR-21-CE14-0056 to K.H. and G.P.; ANR-24-CE92-0023 CoMeT to G.P.). European Research Council (grant no. ERC-CoG-MetaboSENS-819543 to G.P.). INSERM First Step 'Tremplin International' (grant PINUT to G.P.). The association Française contre les myopathies (grant no. #23101 and #25113 to K.H.). DFG, German Research Foundation (grant no. 545363987 CoMeT and grant no. 536691227 Hypermet to D.L.). Campus France PHC-PROCOPE/DAAD (grant no. 57658289 to G.P. and D.L.). Campus France PHC-SAKURA (G.P. and T.O.). French Ministry for Education (N.F.H. and C.O.D.). Fondation pour la Recherche Médicale (N.F.H.). The Genetics and Epigenetics New Education (G.E.N.E.) Graduate School (N.F.H.). China Scholarchip Counsil (J.S.). JSPS grant (grant no. JP22K14779 to G.K.). JSPS grant (grant no. 25H00882 to T.O.). JST CREST grant (grant no. 22717448 to T.O.).

Competing interests

The authors declare no competing interests.

Additional information

Extended data is available for this paper at https://doi.org/10.1038/s41556-026-02030-7.

Supplementary information The online version contains supplementary material available at https://doi.org/10.1038/s41556-026-02030-7.

Correspondence and requests for materials should be addressed to Ganna Panasyuk.

Peer review information *Nature Cell Biology* thanks the anonymous reviewer(s) for their contribution to the peer review of this work. Peer reviewer reports are available.

https://doi.org/10.1038/s41556-026-02030-7

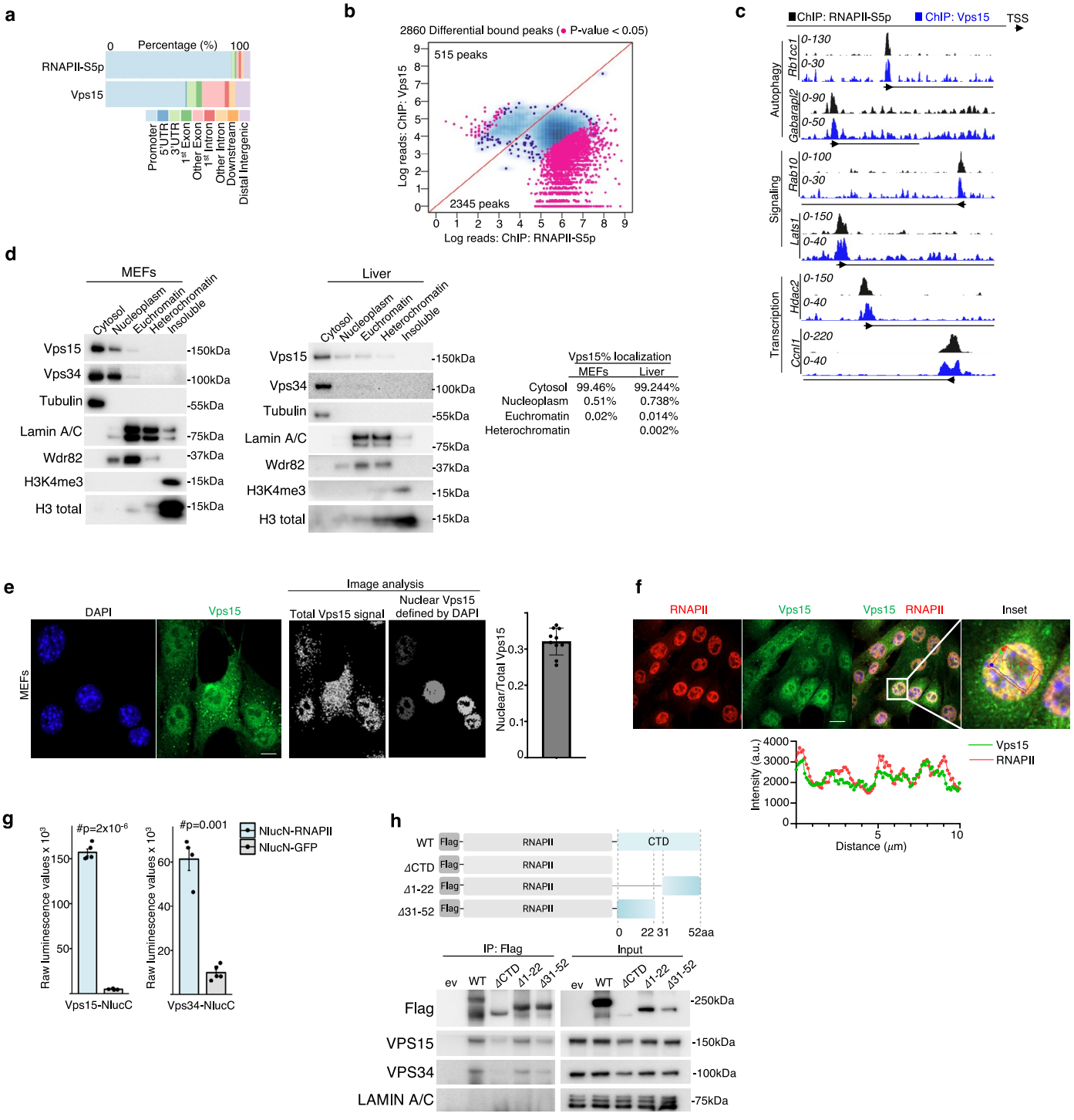

Extended Data Fig. 1 | See next page for caption.

https://doi.org/10.1038/s41556-026-02030-7

Extended Data Fig. 1 | Nuclear PI3K-3 interacts with RNAPII. a, ChIP-RNAPII-S5p and ChIP-Vps15 genomic annotation. **b**, Diffbind differential binding analysis of RNAPII-S5p and Vps15 demonstrating unique and shared peaks. Data are log read concentrations in indicated conditions; pink dots show differentially bound peaks with p-value < 0.05 (n = 2 independent biological repeats per ChIP). **c**, ChIP-RNAPII-S5p and ChIP-Vps15 on indicated genes in MEFs. **d**, Immunoblot of cytosolic and subnuclear fractionation in MEFs and *ad lib* fed liver probed with indicated antibodies. Densitometric quantification of Vps15 distribution across respective fractions, when detected (n = 2 independent biological repeats). **e**, Immunofluorescent microscopy of Vps15 in MEFs. Image analysis to identity nuclear/total Vps15 levels. Data are nuclear/total Vps15 intensity signal ± s.e.m. for n = 10 cells. Scale bar 5µm. **f**, Immunofluorescent microscopy with indicated antibodies in MEFs. Plot shows co-localization intensity between Vps15 and RNAPII in cross section of the nucleus. Scale bar 20µm. **g**, Split-luciferase complementation assay analysis of HEK293T cells overexpressing NlucN-RNAPII, Vps15-NlucC, Vps34-NlucC, or NlucN-GFP (control). Data are raw luminescent values × 10^3, mean ± s.e.m., #p < 0.05 (n = 5 independent biological repeats for Vps15-NlucC, n = 4 independent biological repeats for Vps34-NlucC + NlucN-RNAPII, n = 5 independent biological repeats for Vps34-NlucC + NlucN-GFP) student's two-tailed t-test. **h**, Schematic of RNAPII C-terminal domain (CTD) deletion mutants. Immunoblot analysis of immunoprecipitated Flag-RNAPII complexes of WT CTD, ΔCTD, ΔCTD 1-22aa, or ΔCTD 31-52aa in HEK293T cells, probed with respective antibodies (n = 3 independent biological repeats). **i**, Immunoblot of nuclear RNAPII-immunoprecipitates probed with indicated antibodies. $Vps15^{f/f}$ MEFs were transduced with either adeno-GFP or adeno-CRE adenoviruses and analysed 5 days post-infection. Source numerical data and unprocessed blots are available in source data.

https://doi.org/10.1038/s41556-026-02030-7

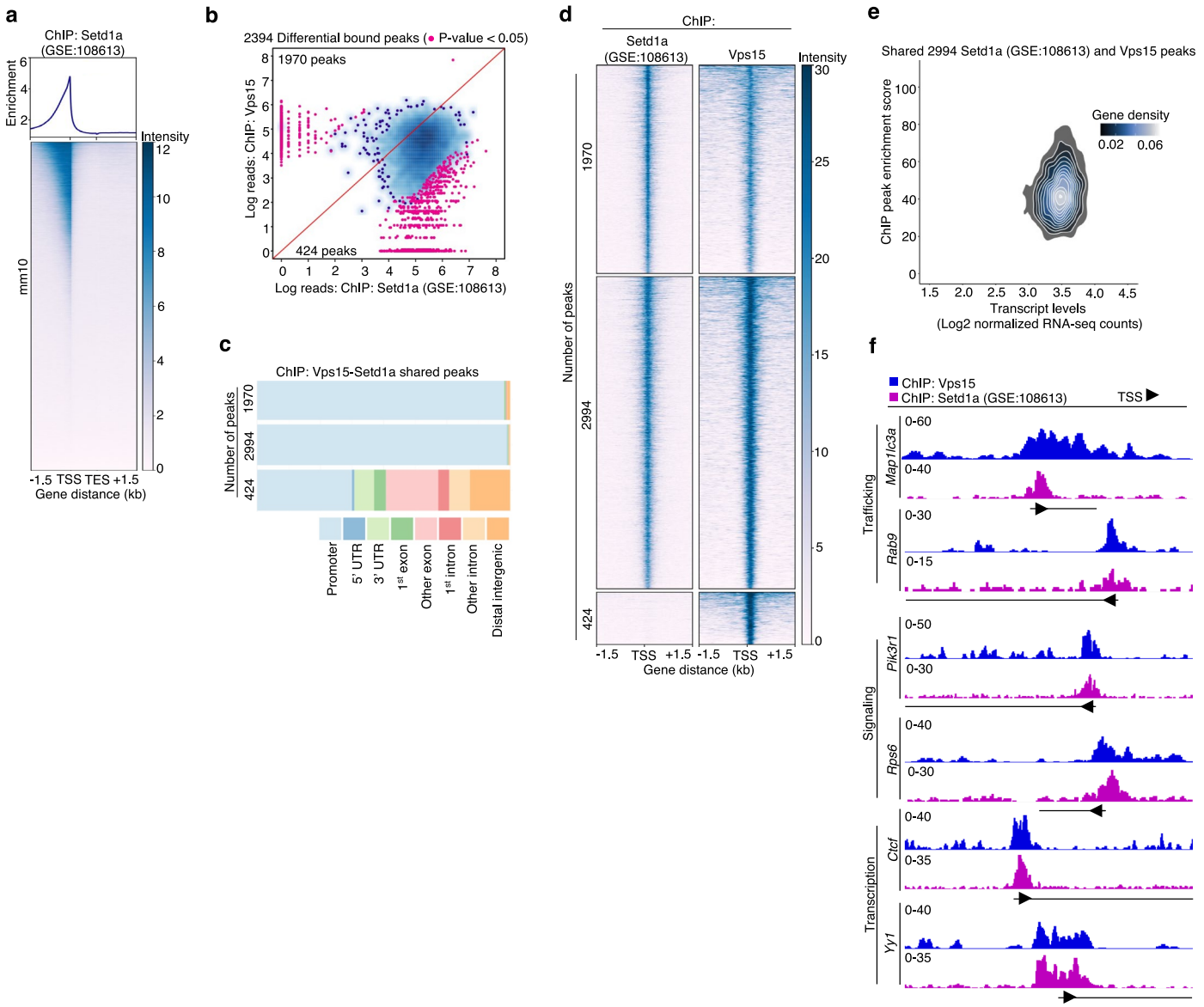

Extended Data Fig. 2 | PI3K-3 overlaps with Setd1a on chromatin. **a**, ChIP-seq heatmap and profile plot of Setd1a (GSE:108613) in mouse embryonic fibroblasts (MEFs). Rows represent peaks ordered by signal strength across the mm10 genome, −1.5 kb to +1.5 kb from the transcription start site (TSS) and transcription end site (TES). **b**, Diffbind differential binding analysis of Setd1a (GSE:108613) and Vps15 demonstrating unique and shared consensus peaks. Data are log read concentrations in indicated conditions; pink dots show differentially bound peaks with p-value < 0.05. **c**, Genomic annotation of unique (Vps15 (424), Setd1a (1970)) and shared (2994) peaks between Setd1a and Vps15. **d**, Heatmap plotting unique (Vps15 (424), Setd1a (1970)) and shared (2994) peaks between Setd1a and Vps15. **e**, Gene density plots of log2 variance stabilized transformation (vst) RNA counts in MEFs plotted against shared (2994) peaks between Setd1a and Vps15. Peak enrichment scores indicate relative peak intensity. Gene density indicates number of genes associated with respective peak score. **f**, Setd1a (GSE:108613) and Vps15 enrichment on promoters of indicted genes associated to cellular pathways. TSS is indicated with an arrow. Source numerical data are available in source data.

https://doi.org/10.1038/s41556-026-02030-7

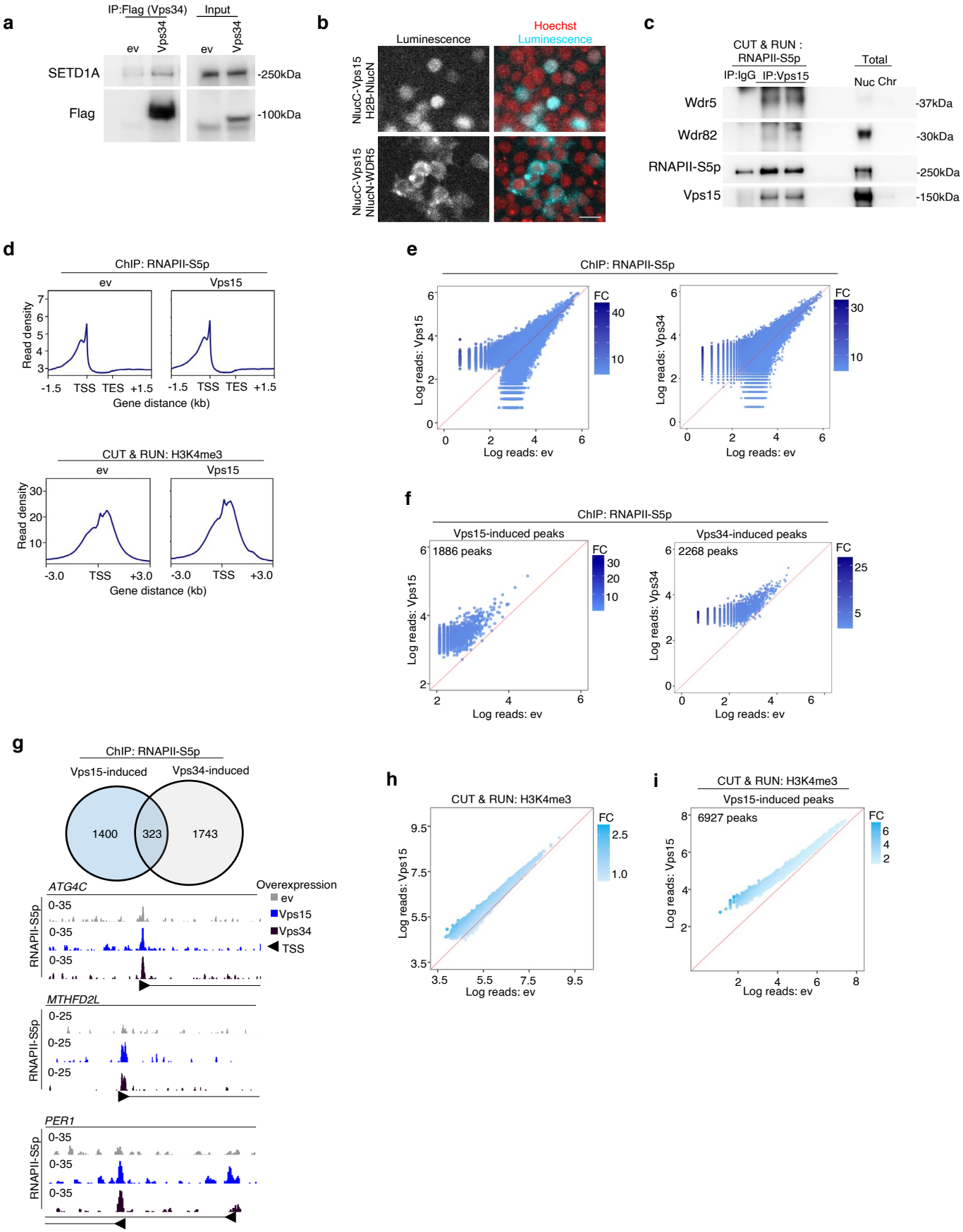

Extended Data Fig. 3 | See next page for caption.

https://doi.org/10.1038/s41556-026-02030-7

Extended Data Fig. 3 | PI3K-3 overexpression induces RNAPII-S5p and H3K4me3 on select loci. a, Immunoblot of immunoprecipitated Flag-Vps34 complexes from HEK293T cells, probed with indicated antibodies (n = 2 independent biological repeats). **b**, Live-cell imaging capture of bioluminescent signal resulting from partner-pair interaction of split-luciferase complementation assay in HEK293T cells (n = 3 independent biological repeats). Scale bar 100μm. **c**, Immunoblot of immunoprecipitated Vps15 complexes from eluates of CUT & RUN RNAPII-S5p in MEFs, probed with indicated antibodies (n = 2 independent biological repeats). **d** ChIP-RNAPII-S5p and CUT & RUN H3K4me3 profile plots in HEK293T cells overexpressing ev (empty vector) or Vps15 (n = 3 independent biological repeats per ChIP). **e**, XY plots of ChIP-RNAPII-S5p in HEK293T cells transfected with ev (empty vector), Vps15 or Vps34. Data are log read counts in indicated conditions. **f**, Bdgdiff differentially bound RNAPII-S5p or peaks induced by Vps15 or Vps34 overexpression, plotted with corresponding log read counts from each condition for fold change > 1 vs. ev expressing cells. **g**, Venn diagram of shared and unique RNAPII-S5p peaks induced by Vps15 and Vps34 (fold change > 1 vs. ev expressing cells) on example gene tracks in indicated conditions. **h**, XY plot of CUT & RUN of H3K4me3 in HEK293T cells transfected with ev (empty vector) or Vps15. Data are log read counts in indicated conditions. **i**, Bdgdiff differentially bound H3K4me3 or peaks induced (fold change > 1) by Vps15 overexpression, plotted with corresponding log read counts from each condition. Source numerical data and unprocessed blots are available in source data.

https://doi.org/10.1038/s41556-026-02030-7

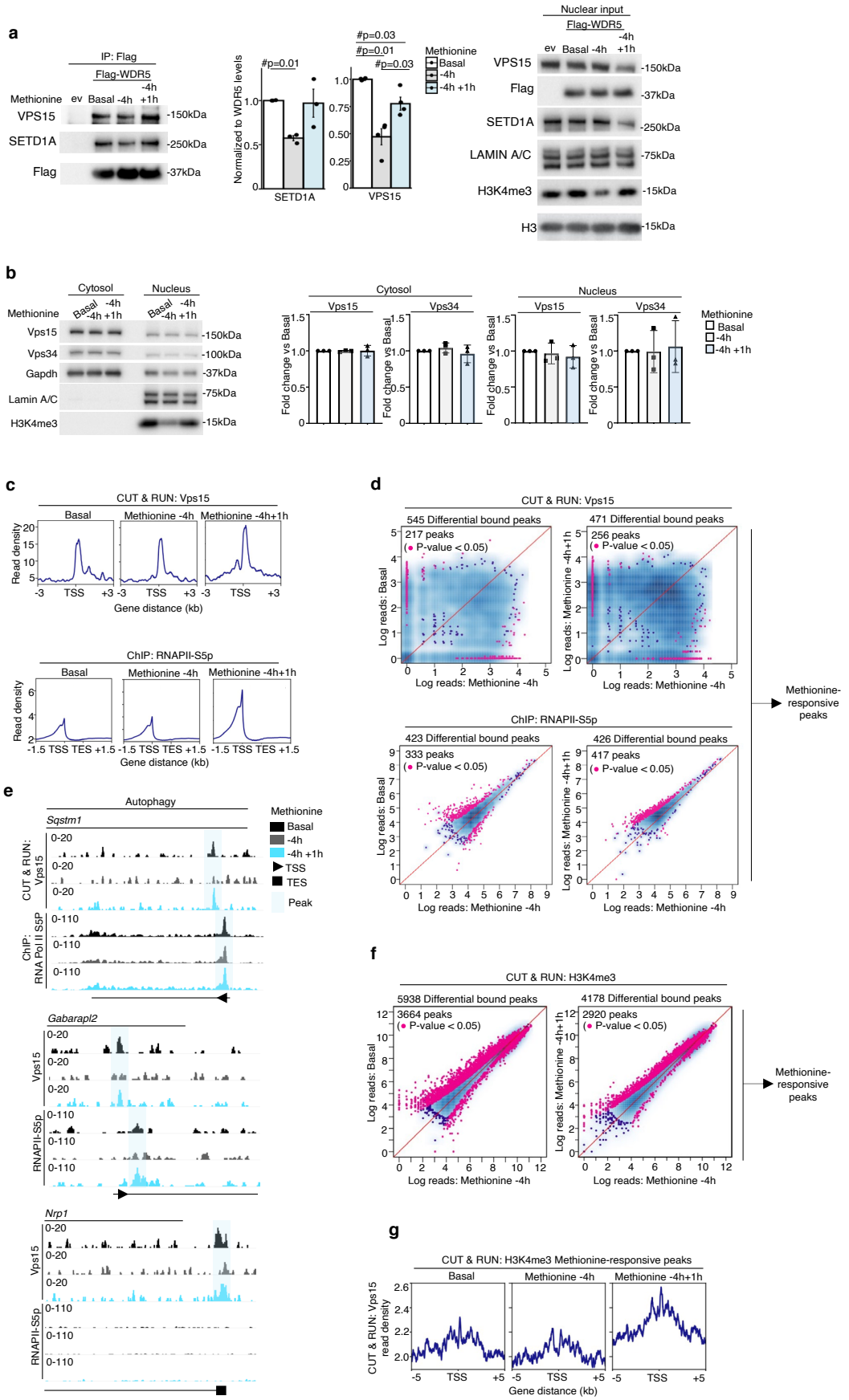

Extended Data Fig. 4 | See next page for caption.

https://doi.org/10.1038/s41556-026-02030-7

Extended Data Fig. 4 | PI3K-3 chromatin recruitment and interation with transcriptional complexes is methionine responsive. a, Immunoblot of Flag-WDR5 immunoprecipitated complexes from nuclei of HEK293T under methionine deprivation (−4h) followed by methionine replenishment (+ 1 h) probed with respective antibodies. Densitometric analysis shows mean ± s.e.m. of SETD1A and VPS15 intensity normalized to Flag-WDR5 signal, fold change vs. Basal methionine condition. #p < 0.05 (n = 3 independent biological repeats for SETD1A, n = 4 independent biological repeats for VPS15), one-way ANOVA with Benjamini-Hochberg correction. **b**, Immunoblots of cytosol and nuclear extracts of MEFs treated with methionine free media (−4h) or methionine reconstitution (−4h + 1 h), probed with indicated antibodies. Densitometric analysis shows mean ± s.e.m. of signal intensity normalized to Gapdh (for cytosol) and Lamin A/C (for nuclei), fold change vs. Basal. #p < 0.05 (n = 3 independent biological repeats), one-way ANOVA with Benjamini-Hochberg correction. **c**, CUT & RUN Vps15 and ChIP-seq RNAPII-S5p profile plots in MEFs in Basal, methionine deprivation (−4h) or methionine replenishment (−4h + 1 h) (n = 2 independent biological repeats for Vps15, n = 3 independent biological repeats for RNAPII-S5p), −1.5 kb or 3 kb to +1.5 kb or 3 kb from the transcription start site (TSS) and transcription end site (TES). **d**, Diffbind differential binding analysis of CUT & RUN Vps15 and ChIP-RNAPII-S5p in MEFs treated as in (**c**). Log read concentrations plotted, pink dots indicate differentially bound peaks with p-value < 0.05 (Diffbind, Wald test) between indicated conditions (n = 2 independent biological repeats for Vps15, n = 3 independent biological repeats for RNAPII-S5p). Peak annotations are provided in Supplementary Table 1. **e**, Representative Vps15 and RNAPII-S5p binding on indicated methionine responsive genes in MEFs under methionine deprivation (−4h) and methionine replenishment (−4h + 1 h). Differential peaks determined by Diffbind highlighted in blue. **f**, Diffbind differential binding analysis of CUT & RUN H3K4me3 in MEFs treated as in (**c**) (Diffbind, Wald test). Log read concentrations plotted, pink dots indicate differentially bound peaks with p-value < 0.05 between indicated conditions (n = 2 independent biological repeats). **g**, CUT & RUN Vps15 reads plotted against CUT & RUN H3K4me3 methionine sensitive (decreased peaks from Basal to Methionine −4h and increased peaks from Methionine −4h to Methionine −4h + 1 h) plots in MEFs in Basal, methionine deprivation (−4h) or methionine replenishment (−4h + 1 h) (n = 2 independent biological repeats for Vps15), −5kb or +5 kb from the transcription start site (TSS). Source numerical data and unprocessed blots are available in source data.

https://doi.org/10.1038/s41556-026-02030-7

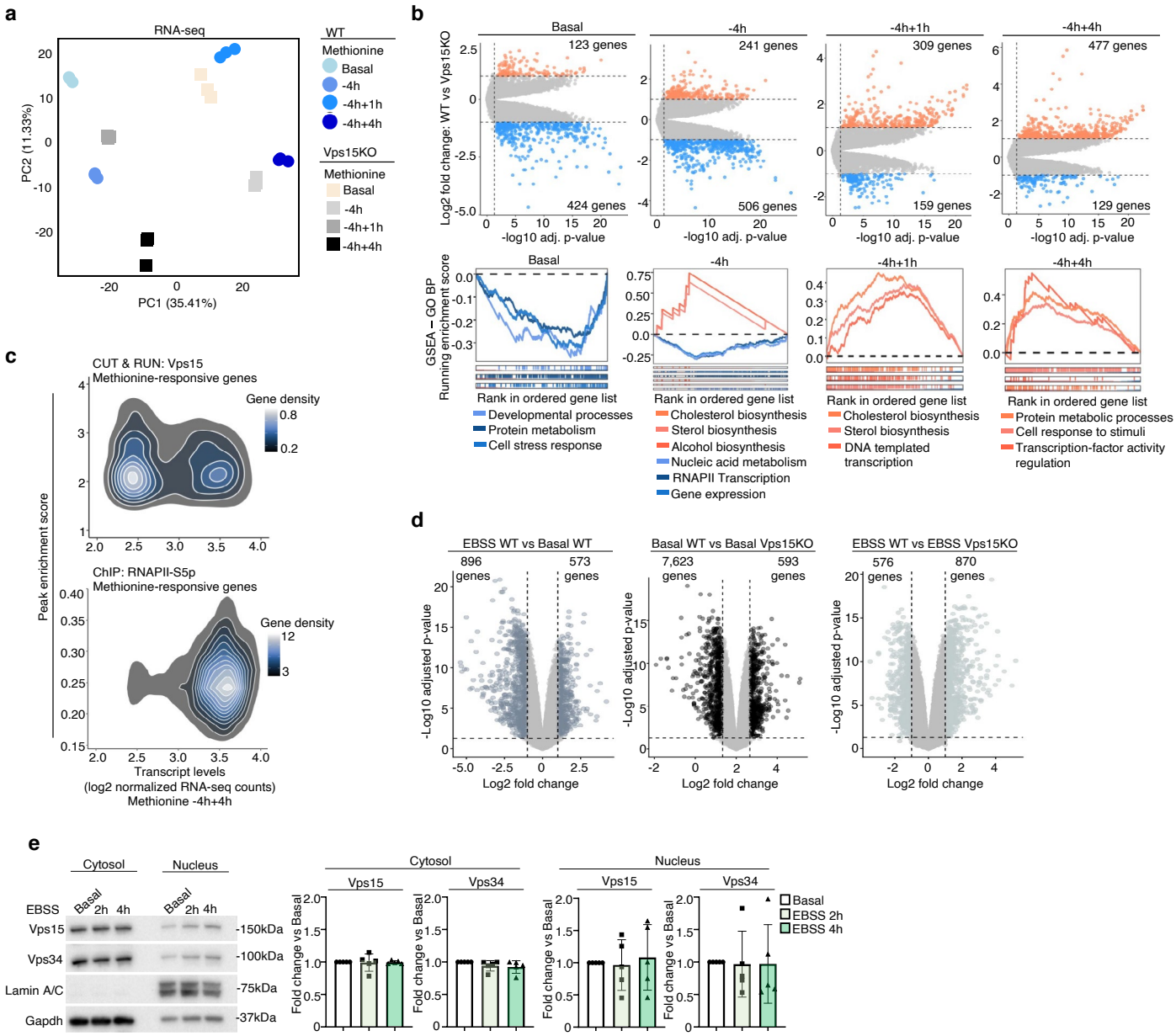

Extended Data Fig. 5 | PI3K-3 depletion results in impaired transcriptional response to methionine availability. a, PCA plot of RNA-seq in Vps15$^{f/f}$ MEFs transduced with adenoviruses expressing GFP (WT) or CRE (Vps15KO) 5 days prior to methionine deprivation (−4h) or followed by methionine replenishment (+1 h or +4 h) (n = 3 independent biological repeats per group). **b**, Volcano plots of differentially expressed genes between WT and Vps15KO MEFs in indicated methionine conditions with respective Gene Set Enrichment Analysis (GSEA) plots showing positively or negatively enriched pathways for upregulated or downregulated genes compared to WT cells (n = 3 independent biological repeats), dashed lines indicate log2 fold change > 1 (or log2 fold change < −1 for downregulated genes) and −log10 of adjusted p-value < 0.05 (limma differential analysis with Benjamini-Hochberg correction). **c**, Gene density plots of log2 variance stabilized (vst) RNA counts in methionine-replenished MEFs plotted against methionine-responsive Vps15 and RNAPII-S5p genes. Peak enrichment scores indicate relative peak intensity. Gene density indicates number of genes per peak score. **d**, Volcano plots of limma identified differentially expressed genes between WT and Vps15KO MEFs in EBSS or Basal conditions (n = 3 independent biological repeats), dashed lines indicate log2 fold change > 1 (or log2 fold change < −1 for downregulated genes) and −log10 of adjusted p-value < 0.05 (limma differential analysis with Benjamamini-Hochberg correction). **e**, Immunoblots of cytosol and nuclear extracts of MEFs treated with EBSS for respective times, probed with indicated antibodies. Densitometric analysis shows mean ± s.e.m. of signal intensity normalized to Gapdh (for cytosol) and Lamin A/C (for nuclei), fold change vs. Basal. #p < 0.05 (n = 5 independent biological repeats per condition), one-way ANOVA with Benjamini-Hochberg correction. Source numerical data and unprocessed blots are available in source data.

https://doi.org/10.1038/s41556-026-02030-7

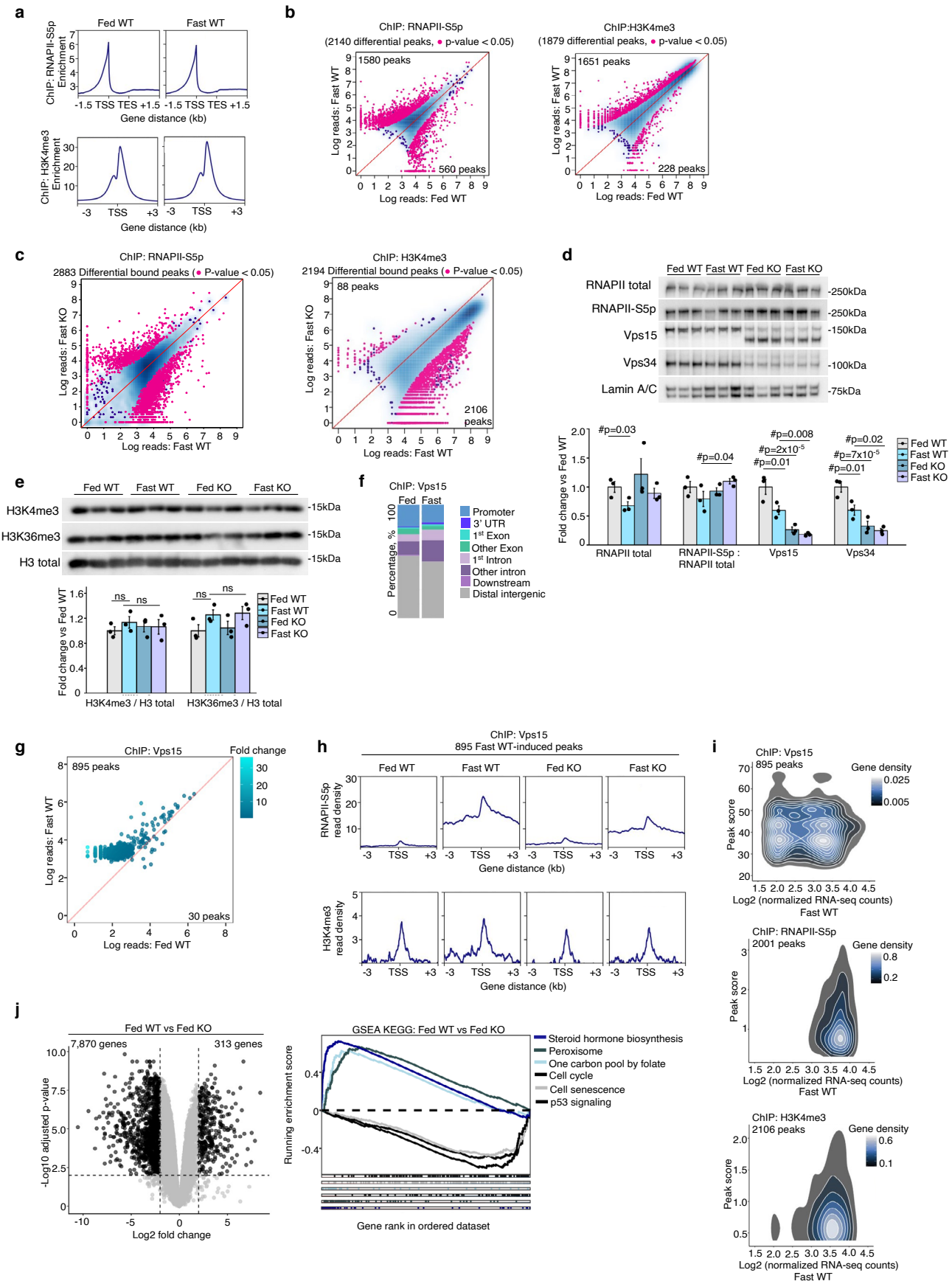

Extended Data Fig. 6 | See next page for caption.

https://doi.org/10.1038/s41556-026-02030-7

Extended Data Fig. 6 | PI3K-3 coordinates RNAPII-S5p recruitment and H3K4me3 deposition in fasted liver. a, ChIP-seq of RNAPII-S5p and H3K4me3 profile plots in livers of 12-week-old male wild type (WT) mice collected at ZT14 after 24 h of fasting or *ad lib* fed (n = 3 mice for RNAPII-S5p, n = 2 mice for H3K4me3). Data presented −1.5 kb or −3kb to +1.5 or +3 kb from TSS and TES. **b**, Diffbind (Wald test) differential binding analysis of RNAPII-S5p and H3K4me3 in livers of mice collected at ZT14 after 24 h of fasting or *ad lib* fed (n = 3 mice per condition). Data are log read concentrations in indicated conditions; pink dots show differentially bound peaks with p-value < 0.05. Peak annotations are provided in Supplementary Table 1. **c**, Differential binding analysis of RNAPII-S5p and H3K4me3 in livers of WT or Vps15iLKO after 24 h of fasting (n = 3 mice per condition). Data are log read concentrations in indicated conditions; pink dots show differentially bound peaks with p-value < 0.05 (Diffbind, Wald test). Peak annotations are provided in Supplementary Table 1. **d**, Immunoblots in nuclear extracts of mouse liver probed with indicated antibodies. Densitometric analysis shows mean ± s.e.m. of antibodies intensity normalized to Lamin A/C, or the RNAPII-S5p to RNAPII total ratio, fold change vs. Fed WT. #p < 0.05 (n = 3 mice per condition), two-way ANOVA with Benjamini-Hochberg correction. **e**, Immunoblots of mouse liver chromatin extracts probed with indicated antibodies. Densitometric analysis shows antibodies intensity normalized to H3 total levels. Data are mean ± s.e.m., #p < 0.05 (n = 3 mice per condition), two-way ANOVA with Benjamini-Hochberg correction (ns indicates not significant). **f**, Vps15 peak genomic annotation in respective conditions. **g**, Bdgdiff differential Vps15 peaks in Fast WT vs. Fed WT with fold change > 1. **h**, ChIP-seq Vps15 Fast WT induced peaks across respective RNAPII-S5p and H3K4me3 read densities. **i**, Gene density plots of Vps15, RNAPII-S5p, and H3K4me3 peaks on RNA-seq variance stabilized (vst) counts in livers of Fast WT mice. Peak scores indicate relative peak intensity. Gene density indicates number of genes per peak score. Source numerical data and unprocessed blots are available in source data.

https://doi.org/10.1038/s41556-026-02030-7

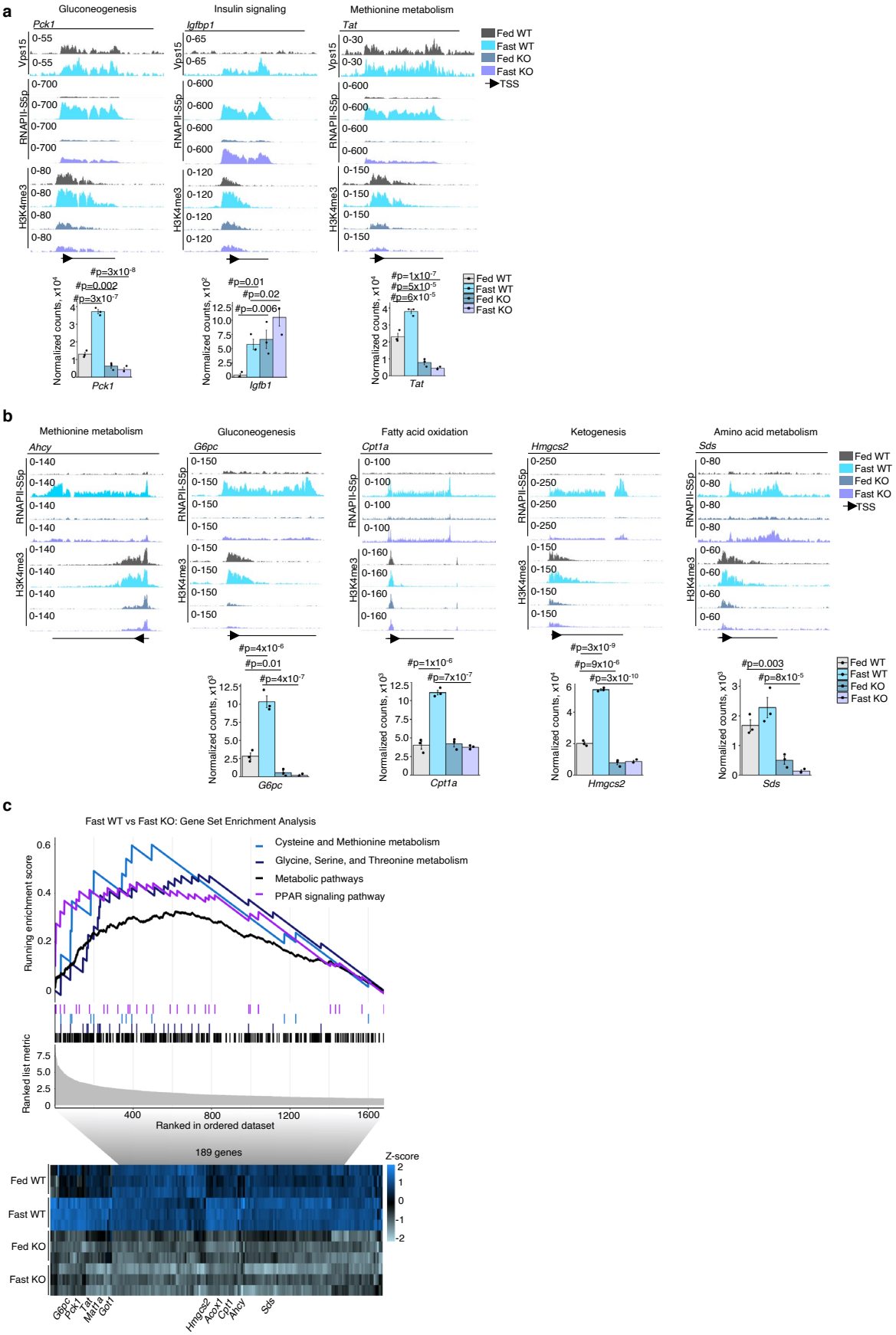

Extended Data Fig. 7 | See next page for caption.

https://doi.org/10.1038/s41556-026-02030-7

Extended Data Fig. 7 | Hepatic PI3K-3 is required for transcriptional rewiring in fasting. a, Vps15, RNAPII-S5p, and H3K4me3 enrichment on indicated genes with respective normalized RNA-seq counts. Data are mean ± s.e.m., #p < 0.05 (n = 3 mice per condition), two-way ANOVA with Benjamini-Hochberg correction. Livers of 12-week-old male Vps15iLKO (KO) and wildtype (WT) control mice were collected at ZT14 after 24 h of fasting or *ad lib* fed. **b**, ChIP-seq in mouse liver of RNAPII-S5p, and H3K4me3 enrichment on indicated genes in respective conditions. Normalized RNA-seq counts for indicated genes in livers of mice treated as in (**a**). Data are mean ± s.e.m., #p < 0.05 (n = 3 mice per condition), two-way ANOVA with Benjamini-Hochberg correction. **c**, DOSE GSEA analysis of RNA-seq comparing Fast WT to Fast KO mice and respective pathways plotted by their Running enrichment score. Heatmap of RNA-seq normalized counts shows 189 genes in the Enrichment score plot and their Z-scores mouse livers of *ad lib* or 24 h fasted WT and Vps15iLKO mice (n = 3 mice per condition). Source numerical data are available in source data.

https://doi.org/10.1038/s41556-026-02030-7

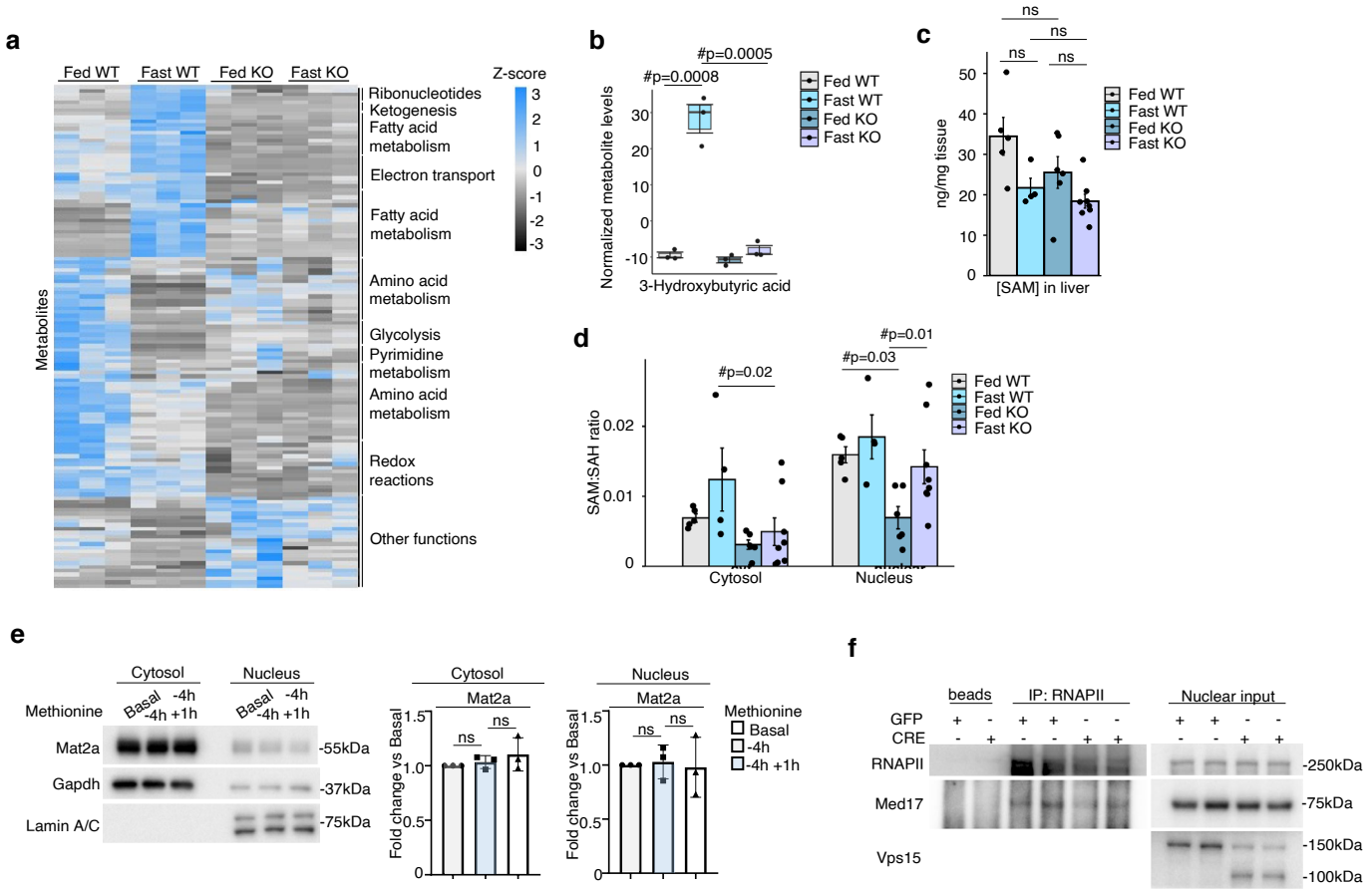

Extended Data Fig. 8 | Metabolic rewiring in fasted liver relies on PI3K-3. **a**, Heatmap of LC-MS metabolomics from livers of 12-week-old male Vps15iLKO (KO) and wildtype (WT) control mice were collected at ZT14 after 24 h of fasting or *ad lib* fed. showing general metabolite classifications (n = 3 mice per condition). **b**, Mean normalized 3-Hydroxybutyric acid metabolite levels in livers of mice treated as in (**a**). Data are mean ± s.e.m., #p < 0.05 (n = 3 mice per condition), two-way ANOVA with Benjamini-Hochberg correction. **c**, Quantitative LC-MS in nuclear extracts of mouse liver in respective conditions showing [SAM] concentrations ng per mg liver tissue. Data are means ± s.e.m., #p < 0.05 (n = 5 mice for Fed WT, n = 4 mice for Fast WT, n = 6 mice for Fed KO, n = 8 mice for Fast KO), two-way ANOVA with Benjamini-Hochberg correction (ns indicates not significant). **d**, SAM:SAH ratio in mouse liver (as in **a**) analysed in cytosolic and nuclear fractions. Data are mean ± s.e.m., #p < 0.05 (n = 5 mice for Fed WT, n = 4 mice for Fast WT, n = 6 mice for Fed KO, n = 8 mice for Fast KO), two-way ANOVA with Benjamini-Hochberg correction. **e**, Immunoblots of cytosol and nuclear extracts of MEFs treated with methionine free media (−4h) or methionine reconstitution (−4h + 1 h), probed with indicated antibodies. Densitometric analysis shows mean ± s.e.m. of signal intensity normalized to Gapdh (for cytosol) and Lamin A/C (for nuclei), fold change vs. Basal. #p < 0.05 (n = 3 independent biological repeats per condition), one-way ANOVA with Benjamini-Hochberg correction (ns indicates not significant). **f**, Immunoblot of RNAPII-immunoprecipitates in the nuclear fraction of MEFs probed with the indicated antibodies. Vps15$^{f/f}$ MEFs were transduced with either adeno-GFP (WT) or adeno-CRE (Vps15KO) and collected 5 days post-infection (n = 2 independent biological repeats). Source numerical data and unprocessed blots are available in source data.

https://doi.org/10.1038/s41556-026-02030-7

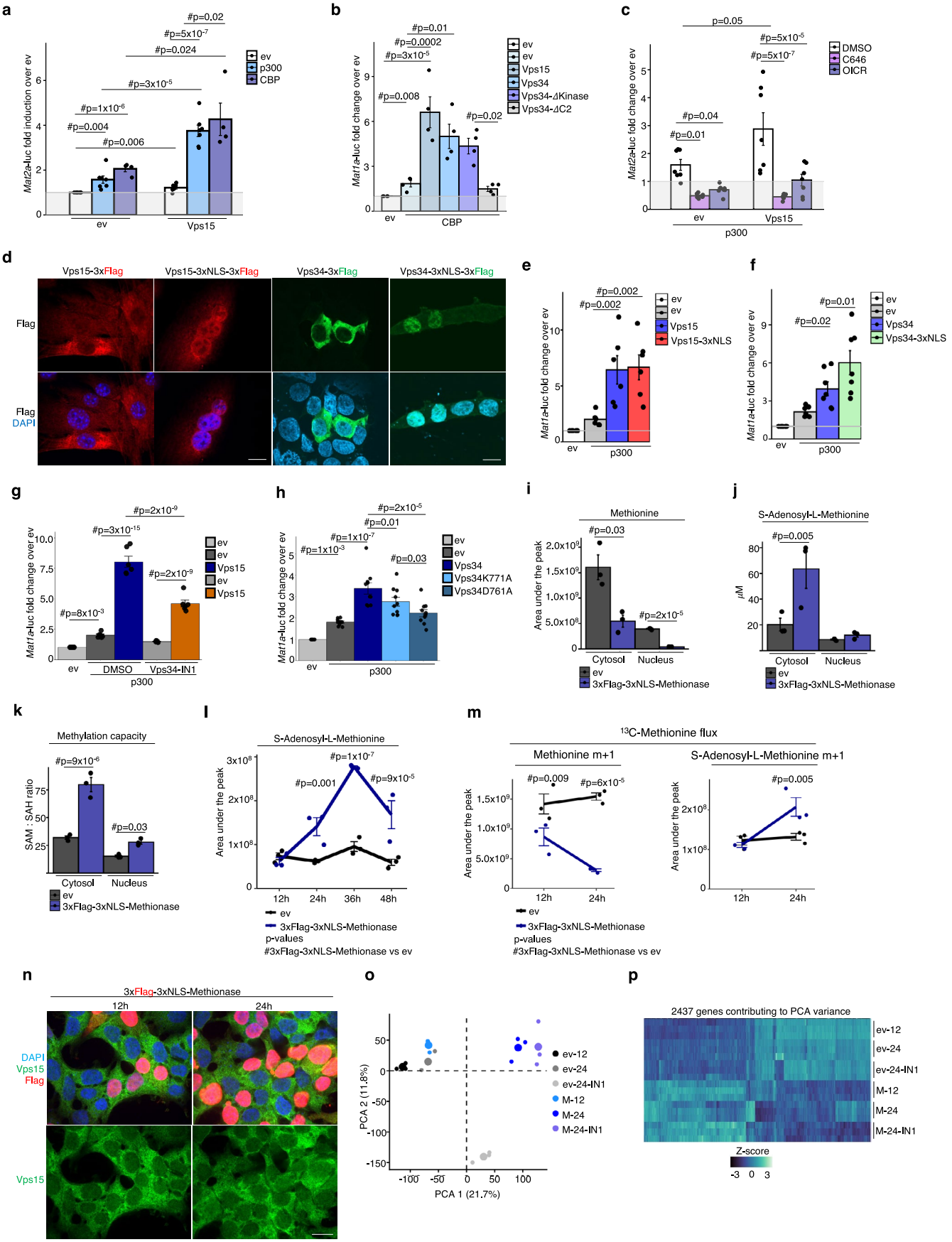

Extended Data Fig. 9 | See next page for caption.

https://doi.org/10.1038/s41556-026-02030-7

Extended Data Fig. 9 | PI3K-3 co-activates p300 and CBP. a, Luciferase assay in HEK293T cells co-transfected with *Mat2a*-luciferase reporter, p300 or CBP, with or without Vps15. Relative luminescence shown as fold induction compared to cells transfected with *Mat2a*-luc + ev (grey background). Data are mean ± s.e.m., #p < 0.05 (n = 7 independent biological repeats for ev +ev, ev + p300, ev + Vps15, and p300+Vps15; n = 4 independent biological repeats for ev + CBP, Vps15 + CBP). **b**, Luciferase assay in HEK293T cells co-transfected with *Mat1a*-luciferase reporter and CBP, Vps15, Vps34, or Vps34 truncated mutants. Relative luminescence shown as fold induction compared to cells transfected with *Mat1a*-luc + ev (grey background). Data are mean ± s.e.m., #p < 0.05 (n = 4 independent biological repeats). **c**, Luciferase assay in HEK293T cells co-transfected with the *Mat2a*-luciferase reporter, p300 with or without Vps15. Cells were treated with either DMSO, C646 (p300 acetyltransferase inhibitor), or OICR (Win-site WDR5 inhibitor). Relative luminescence shown as fold induction compared to cells transfected with *Mat2a*-luc + ev (grey background). Data are mean ± s.e.m., #p < 0.05 (n = 7 independent biological repeats). **d**, Immunofluorescent microscopy of HEK293T cells transiently transfected with indicated constructs (n = 2 independent biological repeats). Scale bar 10µm. **e**, **f**, Luciferase assay in HEK293T cells co-transfected with the *Mat1a*-luciferase reporter, p300, and respective Vps15 or Vps34 constructs. Relative luminescence shown as fold induction compared to cells transfected with *Mat1a*-luc + ev. Data are mean ± s.e.m., #p < 0.05 (n = 6 independent biological repeats for Vps15 constructs, n = 7 independent biological repeats for Vps34 constructs). **g**, Luciferase assay in HEK293T cells co-transfected with the *Mat1a*-luciferase reporter, p300 and Vps15, treated with DMSO or Vps34-IN1. Relative luminescence shown as fold induction compared to cells transfected with *Mat1a*-luc + ev. Data are mean ± s.e.m., #p < 0.05 (n = 6 independent biological repeats). **h**, Luciferase assay in HEK293T cells co-transfected with the *Mat1a*-luciferase reporter, p300 and Vps34, Vps34K771A, or Vps34K761A. Relative luminescence shown as fold induction compared to cells transfected with *Mat1a*-luc + ev. Data are mean ± s.e.m., #p < 0.05 (n = 10 independent biological repeats). Two-way ANOVA with Benjamini-Hochberg correction for panels **a,b,c,e,f,g,h**. **i,j,k**, LC-MS of cytosolic and nuclear fractions for Methionine (area under the peak) (**i**), quantitative measurement of S-Adenosyl-L-Methionine (**j**), and SAM:SAH ratio (**k**) in HEK293T cells expressing 3xFlag-3xNLS-Methionase for 24 h. Data are mean ± s.e.m. #p < 0.05 (n = 3 independent biological repeats), one-way ANOVA with Benjamini-Hochberg correction for each timepoint. **l**, LC-MS detection of S-Adenosyl-L-Methionine in HEK293T cells expressing 3xFlag-3xNLS-Methionase collected at indicated timepoints after transfection. Data are mean ± s.e.m. #p < 0.05 (n = 3 independent biological repeats), one-way ANOVA with Benjamini-Hochberg correction. **m**, LC-MS of Methionine m + 1 and S-Adenosyl-L-Methionine m + 1 in HEK293T cells expressing 3xFlag-3xNLS-Methionase. Cells were incubated with ^{13}C-Methionine for 12 h prior to collection. Data are mean ± s.e.m. #p < 0.05 (n = 3 independent biological repeats), one-way ANOVA with Benjamini-Hochberg correction for each timepoint. **n**, Immunofluorescent microscopy of HEK293T cells transfected with either 3xFlag-3xNLS-Methionase for either 12 or 24 hours, probed with indicated antibodies (n = 2 independent biological repeats). Scale bar is 20 µm. **o**, Principal component analysis (PCA) plot of HEK293T cells transfected with either empty vector (ev) or 3xFlag-3xNLS-Methionase (M) for either 12 or 24 hours. Where indicated, cells were treated with either DMSO or Vps34-IN1 (5 μM) for 12 hours and treatment initiated 12 h post-transfection. **p**, Heatmap of samples in (**o**), showing 2,437 genes that contributed to PCA variance. Source numerical data are available in source data.

https://doi.org/10.1038/s41556-026-02030-7

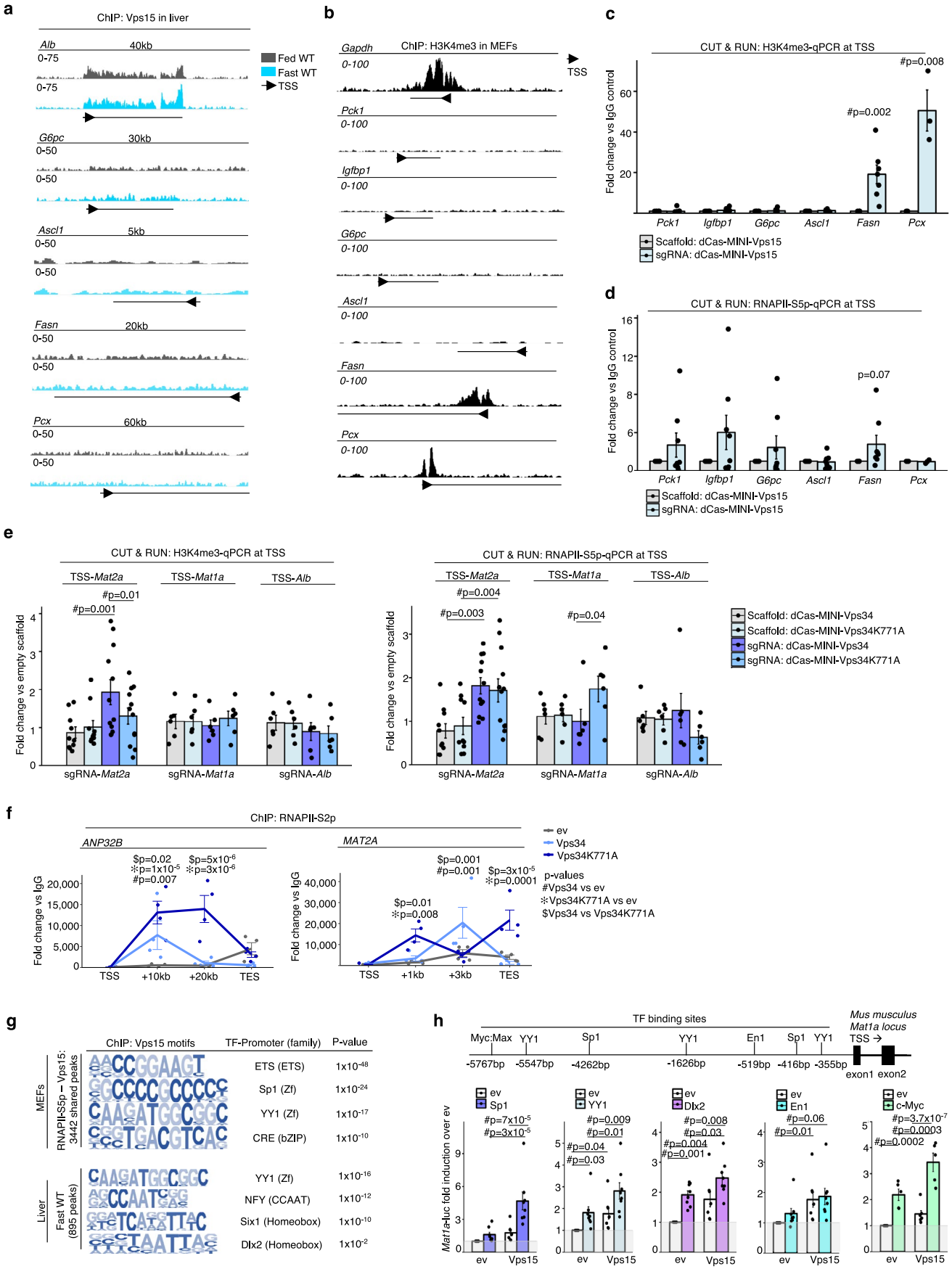

Extended Data Fig. 10 | See next page for caption.

https://doi.org/10.1038/s41556-026-02030-7

Extended Data Fig. 10 | Chromatin targeting of PI3K-3 can induces gene-specific H3K4me3 deposition. a, ChIP-seq of Vps15 on indicated genes in liver of *ad lib* or 24 h fasted WT mice. **b**, ChIP-seq of H3K4me3 on indicated genes in WT MEFs. **c**, CUT & RUN-qPCR of H3K4me3 in MEFs transduced with indicated lenti-sgRNA or lenti -scaffold with no sgRNA and adeno-dCas-MINI-Vps15 or adeno-GFP. Data are means ± s.e.m. fold change to scaffold-dCas-MINI-Vps15 normalized to respective IgG controls. #p < 0.05 (n = 8 independent biological repeats for *Pck1*, *Igfbp1*, *G6pc*, *Ascl1*; n = 7 independent biological repeats for *Fasn*; n = 3 independent biological repeats for *Pcx*) Student's two sided t-test vs. Scaffold: dCas-MINI-Vps15 per gene. **d**, CUT & RUN-qPCR of RNAPII-S5p in MEFs transduced with indicated lenti-sgRNA or lenti-scaffold with no sgRNA and adeno-dCas-MINI-Vps15 or adeno-GFP. Data are means ± s.e.m. fold change to scaffold-dCas-MINI-Vps15 normalized to respective IgG controls. #p < 0.05 (n = 8 independent biological repeats for *Pck1*, *Igfbp1*, *G6pc*, *Ascl1*, *Fasn*; n = 3 independent biological repeats for *Pcx*) Student's two-sided t-test vs. scaffold: dCas-MINI-Vps15 per gene. **e**, CUT & RUN-qPCR of H3K4me3 or RNAPII-S5p in MEFs transduced with indicated lenti-sgRNA or lenti-empty scaffold and adeno-dCas-MINI-Vps34 or adeno-dCas-MINI-Vps34K771A. Data are means ± s.e.m. fold change to empty scaffold dCas-MINI-Vps34 or dCas-MINI-Vps34K771A or normalized to respective IgG controls. #p < 0.05 (n = 6 independent biological repeats for sgRNA-*Mat1a* and sgRNA-*Alb*, n = 10 independent biological repeats for scaffold-dCas-MINI-Vps34/Vps34K771A, n = 12 independent biological repeats for sgRNA-*Mat2a*-dCas-MINI-Vps34/Vps34K771A) two-way ANOVA with Benjamini-Hochberg correction. **f**, ChIP-qPCR of RNAPII-S2p in HEK293T cells expressing indicated constructs, on respective gene regions. Data are mean ± s.e.m. (n = 4 independent biological repeats) and #p < 0.05 in indicated comparisons, one-way ANOVA with Benjamini-Hochberg correction. **g**, HOMER motif analysis (p-value determined with Fisher's Exact test) of consensus transcription factor motifs shared between ChIP-RNAPII-S5p and ChIP-Vps15 in growing MEFs and ChIP-Vps15 in Fast WT liver. **h**, Diagram of the *Mat1a* locus with identified transcription factor binding sites upstream of the TSS. Luciferase assay in HEK293T cells co-transfected with the *Mat1a*-luciferase reporter, Vps15, and respective transcription factors: Sp1, YY1, Dlx2, En1, and c-Myc. Relative luminescence shown as fold induction compared to cells transfected with *Mat1a*-luc + ev (grey background). Data are mean ± s.e.m., #p < 0.05 (n = 6 independent biological repeats for Sp1, YY1, Dlx2, En1: ev + ev, Vps15 + ev. n = 8 independent biological repeats for Sp1, YY1, Dlx2, En1: ev + Sp1, Vps15 + Sp1, ev + YY1, Vps15 + YY1, ev + Dlx2, Vps15 + Dlx2, ev + En1, Vps15 + En1. n = 7 independent biological repeats for cMyc: ev + ev, ev + Vps15. n = 5 independent biological repeats for cMyc: ev + cMyc, Vps15 + cMyc), two-way ANOVA with Benjamini-Hochberg correction. Source numerical data are available in source data.

nature portfolio

Corresponding author(s): Dr. Ganna Panasyuk

Last updated by author(s): June 4, 2026

Reporting Summary

Nature Portfolio wishes to improve the reproducibility of the work that we publish. This form provides structure for consistency and transparency in reporting. For further information on Nature Portfolio policies, see our Editorial Policies and the Editorial Policy Checklist.

Statistics

For all statistical analyses, confirm that the following items are present in the figure legend, table legend, main text, or Methods section.

n/a	Confirmed	
☐	☒	The exact sample size (*n*) for each experimental group/condition, given as a discrete number and unit of measurement
☐	☒	A statement on whether measurements were taken from distinct samples or whether the same sample was measured repeatedly
☐	☒	The statistical test(s) used AND whether they are one- or two-sided *Only common tests should be described solely by name; describe more complex techniques in the Methods section.*
☒	☐	A description of all covariates tested
☐	☒	A description of any assumptions or corrections, such as tests of normality and adjustment for multiple comparisons
☐	☒	A full description of the statistical parameters including central tendency (e.g. means) or other basic estimates (e.g. regression coefficient) AND variation (e.g. standard deviation) or associated estimates of uncertainty (e.g. confidence intervals)
☐	☒	For null hypothesis testing, the test statistic (e.g. *F*, *t*, *r*) with confidence intervals, effect sizes, degrees of freedom and *P* value noted *Give P values as exact values whenever suitable.*
☒	☐	For Bayesian analysis, information on the choice of priors and Markov chain Monte Carlo settings
☒	☐	For hierarchical and complex designs, identification of the appropriate level for tests and full reporting of outcomes
☒	☐	Estimates of effect sizes (e.g. Cohen's *d*, Pearson's *r*), indicating how they were calculated

Our web collection on statistics for biologists contains articles on many of the points above.

Software and code

Policy information about availability of computer code

Data collection	Software for data collection are listed in Methods, including: ChemiDocTM Imager (BioRad) and Image Lab Software for Western Blots revelation, and CFX384 Touch Real-Time PCR Detection System and CFX Maestro (BioRad).
Data analysis	The software packages used in this study are listed in the Methods, including: Western blot quantifications were done using ImageJ software (v. 2.1.0) and calculations in Microsoft Excel 365 (v. 2016). q-PCR data analyses were done using QuantStudio 1 (ThermoFisher Scientific) and calculations in Microsoft Excel 365 (v. 2016) and GraphPad Prizm9. Chip-seq and RNA-seq data were analyzed with SOAPnuke, Bowtie2 v2.4.4, SAMtools v 1.13, deepTools2, MACS2 v2.2.7.1, HOMER (v4.11.1), DOSE (v4.2.0), ChIPeakAnno (3.28.1), ChIPseeker (1.30.3), clusterProfiler (4.2.2), ComplexHeatmap (2.10.0), DESeq2 (1.48.2), GseaVis (0.0.5), GSEABase (1.70.1), GenomicRanges (1.46.1), rtracklayer (1.54.0), KEGGdb (3.2.4), limma (3.64.3), PCAtools (2.20.0), pheatmap (1.0.13), and R v4.5 (http://www.r-project.org/foundation/).

For manuscripts utilizing custom algorithms or software that are central to the research but not yet described in published literature, software must be made available to editors and reviewers. We strongly encourage code deposition in a community repository (e.g. GitHub). See the Nature Portfolio guidelines for submitting code & software for further information.

Data

Policy information about availability of data

All manuscripts must include a data availability statement. This statement should provide the following information, where applicable:

- Accession codes, unique identifiers, or web links for publicly available datasets
- A description of any restrictions on data availability
- For clinical datasets or third party data, please ensure that the statement adheres to our policy

All data are available in the main text or the supplementary materials. Deep-sequencing (ChIP-seq, Cut & Run-seq, and RNAseq) data that support the findings of this study are deposited in the Gene Expression Omnibus (GEO) (GSE290680, GSE290681, GSE290682, GSE320350, GSE322778). Source data have been provided in Source Data file. All other data supporting the findings of this study are available from the corresponding author on reasonable request.

Research involving human participants, their data, or biological material

Policy information about studies with human participants or human data. See also policy information about sex, gender (identity/presentation), and sexual orientation and race, ethnicity and racism.

Reporting on sex and gender	NA
Reporting on race, ethnicity, or other socially relevant groupings	NA
Population characteristics	NA
Recruitment	NA
Ethics oversight	NA

Note that full information on the approval of the study protocol must also be provided in the manuscript.

Field-specific reporting

Please select the one below that is the best fit for your research. If you are not sure, read the appropriate sections before making your selection.

☒ Life sciences ☐ Behavioural & social sciences ☐ Ecological, evolutionary & environmental sciences

For a reference copy of the document with all sections, see nature.com/documents/nr-reporting-summary-flat.pdf

Life sciences study design

All studies must disclose on these points even when the disclosure is negative.

Sample size	For the studies in cell lines we determined the number of the experimental repetitions based on our previous works using these lines (pubmid: 26387534; 23630012). All experiments were independently repeated as indicated in figure legends, and mean and the standard error from the mean were calculated. In studies with animals, the "n" number corresponds to an individual mouse.
Data exclusions	No data or animals were excluded from the analyses.
Replication	All quantified vitro and in vivo assays have been performed at least 3 times. The accompanying quantification and statistics were derived from at least n=3 independent replicates. For biological replicates, independent preparation of depleted cells (adenoviral infection) were used to ensure reproducibility. For in vivo experiments, at least 3 mice per condition were analyzed.
Randomization	For studies in cells, the treatment groups were attributed randomly between plates and wells. For studies in vivo, animals, including those treated with tamoxifen for gene deletion, were randomly allocated into experimental groups based on genotype. The breeding was set up in order of obtain both genotypes in the same litter.
Blinding	In all treatments in vitro and in vivo, the samples were number-coded and the investigators were blinded during extract preparations for molecular analyses (e.g. transcript and protein expression, luciferase assays). Depending on the analysis, the groups were revealed either at the stage of sample quantifications and statistical analyses (e.g. qPCR, luciferase assay) or when it was essential for analysis (e.g. immunoblot of time series to include all conditions in the same gel panel, immunoprecipitation, CUT & RUN or ChIP to set-up control and experimental groups with antibodies).

Reporting for specific materials, systems and methods

We require information from authors about some types of materials, experimental systems and methods used in many studies. Here, indicate whether each material, system or method listed is relevant to your study. If you are not sure if a list item applies to your research, read the appropriate section before selecting a response.

Materials & experimental systems

n/a	Involved in the study
☐	☒ Antibodies
☐	☒ Eukaryotic cell lines
☒	☐ Palaeontology and archaeology
☐	☒ Animals and other organisms
☒	☐ Clinical data
☒	☐ Dual use research of concern
☒	☐ Plants

Methods

n/a	Involved in the study
☐	☒ ChIP-seq
☒	☐ Flow cytometry
☒	☐ MRI-based neuroimaging

Antibodies

Antibodies used

All antibodies are listed in Methods section: The following primary antibodies were used: Vps15 (1:1000, Abnova, H00030849-M02; Genetex, GTX108953), Vps34 (1:1000, Cell Signaling, 4263), Lamin A/C (1:1000, Cell Signaling, 2032), Histone H3 (1:1000 Cell Signaling 4499), H3K4me3 (1:1000, Cell Signaling 9751), H3K36me3 (1:1000, Cell Signaling, 4909), Set1a (1:1000, Cell Signaling 61702), Wdr82 (1:1000, Cell Signaling 99715), Wdr5 (1:1000, Cell Signaling 13105), Flag (1:1000, Sigma, F1804), RNA Pol II (1:1000, Active Motif, 39097), RNA Pol II S5P (1:1000, Chromotek, 3E8-1), RNAPII-S5p (Cell Signaling, 13523), RNAPII-S2p (Cell Signaling, 13499).

Validation

The validation information for the antibodies used in this study are available on the websites of the respective commercial providers as well as in published studies. No custom-made antibodies were used in this study. In addition, for anti-Vps15, anti-Vps34, the specificity in WB, IF, and IP assays was validated in our laboratory in human and mouse cell models upon knock-down (siRNA or shRNA)/KO and overexpression of respective cDNA constructs). The molecular weight markers were used to identify proteins of the expected molecular weight for the target proteins.

Eukaryotic cell lines

Policy information about cell lines and Sex and Gender in Research

Cell line source(s)

HEK293T (CRL-3216) cells were acquired from ATCC. Mouse embryonic fibroblasts (MEFs) were generated by our laboratory from Vps15f/f mice (PMID: 23630012). MEFs were obtained from a pool of embryos from two different females and were passaged every three days before spontaneous transformation. The MEF line proliferating after p25 was considered spontaneously immortalized.

Authentication

All members of our laboratory are trained on the Best Laboratory Practices and safe experimenting including cell line culture in order to prevent contamination with different cell types (ICLAC guidelines). HEK293T cell lines were obtained from ATCC and were not further authenticated. For MEFs Vps15f/f, knock-out was verified by western blots following adeno-Cre infections in every experiment.

Mycoplasma contamination

All cell lines used were bi-weekly tested for contaminations with mycoplasma using commercial PCR Mycoplasma Detection Kit (ABM, #G-238). All tests were negative.

Commonly misidentified lines
(See ICLAC register)

No misidentified lines were used in this study.

Animals and other research organisms

Policy information about studies involving animals; ARRIVE guidelines recommended for reporting animal research, and Sex and Gender in Research

Laboratory animals

Inducible hepatocyte-specific Vps15 knockout TtrCre + ;Vps15 f/f line was generated by our laboratory as described in the methods sections.
Animals of 3-5 month old TtrCre + ;Vps15 f/f were used for the experimentation. All animals used in the study were fed ad libitum standard chow diet (Teklad Global 2918, 18% protein, irradiated) and kept under 12h/12h (8am/8pm) light on/off cycle under an ambient temperature (+21-22C) and humidity ranging between 50-60%. All animal studies were performed by authorized users in compliance with ethical regulations for animal testing and research.

Wild animals

No wild animals were used.

Reporting on sex

Male mice were used in this study as it is specified in figure legends.

Field-collected samples

The study did not involve samples collected in the field.

Ethics oversight

The study was approved by the ethical committee of University Paris Cité (authorization number APAFIS#32312).

Note that full information on the approval of the study protocol must also be provided in the manuscript.

Plants

Seed stocks: NA

Novel plant genotypes: NA

Authentication: NA

ChIP-seq

Data deposition

☒ Confirm that both raw and final processed data have been deposited in a public database such as GEO.

☒ Confirm that you have deposited or provided access to graph files (e.g. BED files) for the called peaks.

Data access links
May remain private before publication.

Deep-sequencing (ChIP–seq, Cut & Run-seq, and RNA-seq) data that support the findings of this study are deposited in the Gene Expression Omnibus (GSE290680, GSE290681, GSE290682, GSE320350, GSE322778).

Files in database submission

GSM8819432 RNA, Liver, Fed wt, rep1
GSM8819433 RNA, Liver, Fed wt, rep2
GSM8819434 RNA, Liver, Fed wt, rep3
GSM8819435 RNA, Liver, Fast wt, rep1
GSM8819436 RNA, Liver, Fast wt, rep2
GSM8819437 RNA, Liver, Fast wt, rep3
GSM8819438 RNA, Liver, Fed Vps15LKO, rep1
GSM8819439 RNA, Liver, Fed Vps15LKO, rep2
GSM8819440 RNA, Liver, Fed Vps15LKO, rep3
GSM8819441 RNA, Liver, Fast Vps15LKO, rep1
GSM8819442 RNA, Liver, Fast Vps15LKO, rep2
GSM8819443 RNA, Liver, Fast Vps15LKO, rep3
GSM9065503 RNA, MEF WT, basal, rep1
GSM9065504 RNA, MEF WT, basal, rep2
GSM9065505 RNA, MEF WT, basal, rep3
GSM9065506 RNA, MEF Vps15KO, basal, rep1
GSM9065507 RNA, MEF Vps15KO, basal, rep2
GSM9065508 RNA, MEF Vps15KO, basal, rep3
GSM9065509 RNA, MEF WT, -4h_Methionine, rep1
GSM9065510 RNA, MEF WT, -4h_Methionine, rep2
GSM9065511 RNA, MEF WT, -4h_Methionine, rep3
GSM9065512 RNA, MEF Vps15KO, -4h_Methionine, rep1
GSM9065513 RNA, MEF Vps15KO, -4h_Methionine, rep2
GSM9065514 RNA, MEF Vps15KO, -4h_Methionine, rep3
GSM9065515 RNA, MEF WT, -4h+1h_Methionine, rep1
GSM9065516 RNA, MEF WT, -4h+1h_Methionine, rep2
GSM9065517 RNA, MEF WT, -4h+1h_Methionine, rep3
GSM9065518 RNA, MEF Vps15KO, -4h+1h_Methionine, rep1
GSM9065519 RNA, MEF Vps15KO, -4h+1h_Methionine, rep2
GSM9065520 RNA, MEF Vps15KO, -4h+1h_Methionine, rep3
GSM9065521 RNA, MEF WT, -4h+4h_Methionine, rep1
GSM9065522 RNA, MEF WT, -4h+4h_Methionine, rep2
GSM9065523 RNA, MEF WT, -4h+4h_Methionine, rep3
GSM9065524 RNA, MEF Vps15KO, -4h+4h_Methionine, rep1
GSM9065525 RNA, MEF Vps15KO, -4h+4h_Methionine, rep2
GSM9065526 RNA, MEF Vps15KO, -4h+4h_Methionine, rep3

GSM8819450 Vps15, mouse embryonic fibroblasts, basal methionine, rep1
GSM8819451 Vps15, mouse embryonic fibroblasts, basal methionine, rep2
GSM8819452 Vps15, mouse embryonic fibroblasts, 4h methionine starvation, rep1
GSM8819453 Vps15, mouse embryonic fibroblasts, 4h methionine starvation, rep2
GSM8819454 Vps15, mouse embryonic fibroblasts, 1h methionine stimulation, rep1
GSM8819455 Vps15, mouse embryonic fibroblasts, 1h methionine stimulation, rep2
GSM8819456 IgG, mouse embryonic fibroblasts, basal methionine
GSM8819457 IgG, mouse embryonic fibroblasts, 4h methionine starvation

GSM8819458 IgG, mouse embryonic fibroblasts, 4h methionine stimulation
GSM9065553 H3K4me3, HEK293T, empty vector overexpression, rep1
GSM9065554 H3K4me3, HEK293T, empty vector overexpression, rep2
GSM9065555 H3K4me3, HEK293T, Flag-Vps15 overexpression, rep1
GSM9065556 H3K4me3, HEK293T, Flag-Vps15 overexpression, rep2
GSM9065557 IgG, HEK293T, empty vector overexpression, rep1
GSM9065558 IgG, HEK293T, empty vector overexpression, rep2
GSM9065559 IgG, HEK293T, Flag-Vps15 overexpression, rep1
GSM9065560 IgG, HEK293T, Flag-Vps15 overexpression, rep2

GSM8819464 RNA Pol II S5P, liver, Fed Vps15LKO, rep1
GSM8819465 RNA Pol II S5P, liver, Fed Vps15LKO, rep2
GSM8819466 RNA Pol II S5P, liver, Fed Vps15LKO, rep3
GSM8819467 RNA Pol II S5P, liver, Fast Vps15LKO, rep1
GSM8819468 RNA Pol II S5P, liver, Fast Vps15LKO, rep2
GSM8819469 RNA Pol II S5P, liver, Fast Vps15LKO, rep3
GSM8819470 Vps15, liver, Fed wt, rep1
GSM8819471 Vps15, liver, Fed wt, rep2
GSM8819472 Vps15, liver, Fast wt, rep1
GSM8819473 Vps15, liver, Fast wt, rep2
GSM8819474 Vps15, liver, Fast wt, rep3
GSM8819475 Input for RNA Pol II S5P Fed wt
GSM8819476 Input for Vps15 Fed wt
GSM8819477 Input for RNA Pol II S5P Fast wt
GSM8819478 Input for Vps15 Fast wt
GSM8819479 Input for RNA Pol II S5P Fed Vps15LKO
GSM8819480 Input for RNA Pol II S5P Fast Vps15LKO
GSM8819481 H3K4me3, liver, Fed wt, rep1
GSM8819482 H3K4me3, liver, Fed wt, rep2
GSM8819483 H3K4me3, liver, Fast wt, rep1
GSM8819484 H3K4me3, liver, Fast wt, rep2
GSM8819485 H3K4me3, liver, Fed Vps15LKO, rep1
GSM8819486 H3K4me3, liver, Fed Vps15LKO, rep2
GSM8819487 H3K4me3, liver, Fast Vps15LKO, rep1
GSM8819488 H3K4me3, liver, Fast Vps15LKO, rep2
GSM8819489 Input for H3K4me3 Fed wt
GSM8819490 Input for H3K4me3 Fast wt
GSM8819491 Input for H3K4me3 Fed Vps15LKO
GSM8819492 Input for H3K4me3 Fast Vps15LKO
GSM8819493 RNA Pol II S5P, HEK293 cells, overexpressing pcDNA3.1, rep1
GSM8819494 RNA Pol II S5P, HEK293 cells, overexpressing pcDNA3.1, rep2
GSM8819495 RNA Pol II S5P, HEK293 cells, overexpressing Vps15, rep1
GSM8819496 RNA Pol II S5P, HEK293 cells, overexpressing Vps15, rep2
GSM8819497 RNA Pol II S5P, HEK293 cells, overexpressing Vps34, rep1
GSM8819498 RNA Pol II S5P, HEK293 cells, overexpressing Vps34, rep2
GSM8819499 Input for HEK293 cells overexpressing pcDNA3.1
GSM8819500 Input for HEK293 cells overexpressing Vps15
GSM8819501 Input for HEK293 cells overexpressing Vps34
GSM9065696 RNA Pol II S5P, liver, Fed wt, rep1
GSM9065697 RNA Pol II S5P, liver, Fed wt, rep2
GSM9065698 RNA Pol II S5P, liver, Fed wt, rep3
GSM9065699 RNA Pol II S5P, liver, Fast wt, rep1
GSM9065700 RNA Pol II S5P, liver, Fast wt, rep2
GSM9065701 RNA Pol II S5P, liver, Fast wt, rep3
GSM9065702 Input for RNA Pol II S5P Fed wt, rep1
GSM9065703 Input for RNA Pol II S5P Fast wt, rep1
GSM9065704 RNA Pol II S5P, MEFs, basal methionine, rep1
GSM9065705 RNA Pol II S5P, MEFs, basal methionine, rep2
GSM9065706 RNA Pol II S5P, MEFs, basal methionine, rep3
GSM9065707 RNA Pol II S5P, MEFs, -4h methionine, rep1
GSM9065708 RNA Pol II S5P, MEFs, -4h methionine, rep2
GSM9065709 RNA Pol II S5P, MEFs, -4h methionine, rep3
GSM9065710 RNA Pol II S5P, MEFs, -4h+1h methionine, rep1
GSM9065711 RNA Pol II S5P, MEFs, -4h+1h methionine, rep2
GSM9065712 RNA Pol II S5P, MEFs, -4h+1h methionine, rep3
GSM9065713 Input for RNA Pol II S5P in MEFs basal methionine condition
GSM9065714 Input for RNA Pol II S5P in MEFs -4h methionine condition
GSM9065715 Input for RNA Pol II S5P in MEFs -4h+1h methionine condition
GSM9065716 RNA Pol II S5P, MEFs, basal growth, rep1
GSM9065717 RNA Pol II S5P, MEFs, basal growth, rep2
GSM9065718 Vps15, MEFs, basal growth, rep1
GSM9065719 Vps15, MEFs, basal growth, rep2
GSM9065720 Input for MEFs, basal growth, rep1

GSM9541293 MEF WT, basal, rep1
GSM9541294 MEF WT, basal, rep2
GSM9541295 MEF WT, basal, rep3
GSM9541296 MEF Vps15KO, basal, rep1
GSM9541297 MEF Vps15KO, basal, rep2
GSM9541298 MEF Vps15KO, basal, rep3
GSM9541299 MEF WT, EBSS2h, rep1
GSM9541300 MEF WT, EBSS2h, rep2
GSM9541301 MEF WT, EBSS2h, rep3
GSM9541302 MEF Vps15KO, EBSS2h, rep1
GSM9541303 MEF Vps15KO, EBSS2h, rep2
GSM9541304 MEF Vps15KO, EBSS2h, rep3

GSM9558283 RNA, HEK293T, pLEX, dmso,12h, rep1
GSM9558284 RNA, HEK293T, pLEX, dmso,12h, rep2
GSM9558285 RNA, HEK293T, pLEX, dmso,12h, rep3
GSM9558286 RNA, HEK293T, MethionaseNLS, dmso,12h, rep1
GSM9558287 RNA, HEK293T, MethionaseNLS, dmso,12h, rep2
GSM9558288 RNA, HEK293T, MethionaseNLS, dmso,12h, rep3
GSM9558289 RNA, HEK293T, pLEX, dmso,24h, rep1
GSM9558290 RNA, HEK293T, pLEX, dmso,24h, rep2
GSM9558291 RNA, HEK293T, pLEX, dmso,24h, rep3
GSM9558292 RNA, HEK293T, MethionaseNLS, dmso,24h, rep1
GSM9558293 RNA, HEK293T, MethionaseNLS, dmso,24h, rep2
GSM9558294 RNA, HEK293T, MethionaseNLS, dmso,24h, rep3
GSM9558295 RNA, HEK293T, pLEX, Vps34IN1,24h, rep1
GSM9558296 RNA, HEK293T, pLEX, Vps34IN1,24h, rep2
GSM9558297 RNA, HEK293T, pLEX, Vps34IN1,24h, rep3
GSM9558298 RNA, HEK293T, MethionaseNLS, Vps34IN1,24h, rep1
GSM9558299 RNA, HEK293T, MethionaseNLS, Vps34IN1,24h, rep2
GSM9558300 RNA, HEK293T, MethionaseNLS, Vps34IN1,24h, rep3

Genome browser session
(e.g. UCSC)

Not applicable.

Methodology

Replicates

n=2-3 per condition were sequenced and analyzed, and specified for each experiment.

Sequencing depth

Average of 20-30million (100bp-Paired End) clean reads following filtering low quality reads, N reads, and adapter sequences.

Antibodies

Vps15 (Abnova, H00030849-M02), RNA Pol II S5P (Abcam, ab5408), H3K4me3 (Cell Signaling, 9751), rabbit-IgG (Cell Signaling, 3900)

Peak calling parameters

RNA Pol II S5P peak calling was performed using: macs2 callpeak -t -c -f BAMPE -g mm --nomodel --extsize 200 --outdir pol2_peaks

H3K4me3 peak calling was performed using: macs2 callpeak -t -c --nomodel --extsize 200 -f BAM -g mm --outdir H3K4me3_peaks

Vps15 peak calling was performed using: macs2 callpeak -t -c -f BAMPE -g mm --nomodel --extsize 200 --outdir vps15_peaks

Data quality

Data filtering was performed with SOAPnuke to remove adaptor sequences and low-quality reads. Data filtering parameter was: SOAPnuke filter -l 5 -q 0.5 -n 0.1 -Q 2 -c 40.

SAMtools for filtering reads with mapping quality score above 40, Picard Tools (v2.18.25) for marking and removing duplicates, blacklisted regions removed using mm10-blacklist.v2.bed, SAMtools for indexing and sorting SAM files.

Software

Sequencing was performed with the DNBSEQ-400 sequencer (Beijing Genomics Institute, China). All data were analyzed with the pipeline: Bowtie2 for alignment to mm10 or hg28 genomes, MACS2 for peak calling and bdgdiff differential binding analysis, R package Diffbind (V3.10.0) for differential peak calling, R package ChIPseeker and clusterProfiler for peak annotation and GO/KEGG pathway enrichment. IGV_2.8.13 used for bigwig/bam file visualization.